2D Materials for Organic and Perovskite Photovoltaics

Um Kanta Aryal[1], Mehrad Ahmadpour[1], Vida Turkovic[1], Horst-Günter Rubahn[1], Aldo Di Carlo[2,3], Morten Madsen[1,*]

1. University of Southern Denmark, Mads Clausen Institute, SDU NanoSYD 6400 Sønderborg, Denmark
2. Istituto di Struttura della Materia, CNR-ISM, Via del Fosso del Cavaliere 100, 00133, Rome, Italy
3. CHOSE (Centre for Hybrid and Organic Solar Energy), Department of Electronic Engineering, University of Rome "Tor Vergata", via del Politecnico 1, 00133 Rome, Italy

Abstract

The power conversion efficiency of thin film solar cells based on organic and perovskite materials has improved dramatically in recent years, currently reaching above 18 % for organic photovoltaics and above 25 % for perovskite solar cells. Combined with their appealing properties, such as mechanical flexibility, light weight, semi-transparency, and low-cost large-scale roll-to-roll (R2R) processing compatibility, the high conversion efficiencies have placed organic and perovskite solar cells at the center of attention in terms of promising PV technologies. In this context, 2D materials are, due to their unique properties such as high charge carrier mobility, high optical transparency and especially tunable electronic structure, ideal contact layer materials in thin film solar cell devices. They can be applied as electrodes, hole (HTL) and electron (ETL) transport layers, and additives in active layers. This review paper focuses on the integration of 2D graphene and its derivatives, and 2D materials beyond graphene, i.e. transitional metal dichalcogenides (TMD), MXene, black phosphorous (BP) and boron nitrides in organic and perovskite solar cells, and discusses the positive influence these material systems have shown on both the fundamental photophysical processes, as well as on device stability and lifetime. Furthermore, this review addresses the future potential of 2D materials for the development of lightweight, eco-friendly, high performance and cost-effective flexible solar cells, provided by the high mechanical flexibility, high environmental stability, low electrical resistivity, and low environmental impact of these 2D material systems.

Introduction

In recent years, solar cells based on organic and perovskite materials have attracted significant attention due to their strong rise in power conversion efficiency (PCE). Their appealing properties, such as mechanical flexibility, light weight, semi-transparency, and low-cost roll-to-roll (R2R) processing techniques, are opening up for large-scale industry-compatible manufacturing routes [1-4]. The exploration of new electron donors, and especially non-fullerene electron acceptor materials, and different interlayers for organic photovoltaics (OPV), as well as the novel device engineering approaches including solvent engineering, interfacial engineering and bandgap engineering, for perovskite solar cells (PSC), has been detrimental to improving their performance significantly over the past few years [5-12]. To date, the certified PCE is above 18 % for OPV and above 25 % for PSC [13-17].

Flexible, transparent, conductive electrodes made from indium tin oxide (ITO) and fluorine-doped tin oxide (FTO) are typically employed as transparent conductive electrodes (TCE) in such photovoltaic devices. Due to the high cost of some of the raw materials, as well as the mechanical brittleness, alternative TCE, such as carbon nanotubes, two-dimensional (2D) metal carbides, nitrides, carbonitrides, graphene, conducting polymers, and metal nanowires, have been explored for the development of low-cost, scalable, flexible and wearable optoelectronic devices [18-22]. Among these TCE, 2D metal carbonitrides and graphene have shown excellent electrical performance with combined high optical transparency, making them very suitable for these applications [23-26]. In addition, beyond graphene and graphene derivatives, namely 2D materials, such as transitional metal dichalcogenides (TMD), transitional metal carbides and/or nitrides (MXene), black phosphorus (BP) and hexagonal boron nitrides, have been applied in the thin film device stacks, where they have shown very promising properties for extraction, transport and collection of charge carriers towards the respective electrodes. This makes them optimal for interlayers in such devices. 2D materials are an emerging class of nanostructured materials with unique structural and physical properties. Their properties, such as their bandgaps and work functions, can be extensively tuned by doping and passivation schemes, and via size control of their atomic-scale thickness [27,28], making it possible to adjust for selective charge carrier extraction with low energetic losses and limited surface recombination.

Graphene is a 2D allotrope of carbon consisting of a six-membered cyclic arrangement of carbon atoms in which the C-atoms are sp^2 bonded, creating a hexagonal 2D lattice that acts as a basic

element for graphite, carbon nanotubes and fullerenes. Graphene has many exceptional properties, such as high carrier mobility, electrical conductivity (zero-bandgap semimetal), mechanical durability, low optical absorbance in the visible spectral region, work function tunability combined with chemical modification, and configuration possibilities. [29-33]. One of the important derivatives of graphene, namely graphene oxide (GO), can be prepared with the introduction of many functional groups to the graphene surface, e.g., epoxide, carbonyl and hydroxyl groups, which tune the optoelectronic properties and provide hydrophilic behavior, allowing for uniform dispersion in an aqueous solution. This opens for large-scale fabrication using solution processing, which is highly appealing for photovoltaic devices [34]. In contrast to graphene, the as-synthesized GO shows poor electrical conductivity, however, it can be transformed into reduced graphene oxide (r-GO) with high conductivity and transparency upon chemical reduction processes [35,36]. In addition to GO and r-GO, there are other derivatives of graphene, such as graphene quantum dots (GQD) and graphene nanoribbons, which have also been studied for the development of improved photovoltaic performance and device stability.

Among the 2D materials beyond graphene and its derivatives, transitional metal dichalcogenides (TMD) are one of the most studied groups. They have a general formula MX_2, where M refers to the transition metal element and X stands for the chalcogen element, e.g., MoS_2, WS_2, TaS_2. In the bulk of TMD, the metal atoms in monolayer TMD are sandwiched between two layers of chalcogen atoms via covalent M-X bonding, while adjacent layers of TMD (in bulk forms) are coupled by weak van der Waals forces, enabling exfoliation into single layers [37,38]. Unlike the bulk counterparts with indirect bandgaps, 2D monolayers of TMD materials have a tunable direct bandgap, typically in the range 1.3-1.9 eV, depending also on the number of layers [39,40]. MXene have the general formula of $M_{n+1}X_nT_x$, where M stands for the transition metal, X for carbon and/or nitrogen and T for the terminal groups like -OH, -F, or -O, with n being a number between 1-3 [41-44]. MXene exhibit high conductivity, optical transmittance in the visible range, superior hydrophilicity, and high thermal stability. The choice of the transition metal, as well as the X element of the MXene, provides the possibility of tuning their electronic properties and work function, as needed for efficient interlayers in optoelectronics and photovoltaic applications [45-48]. Black phosphor (BP) is an allotrope of the most thermodynamically stable phosphorous in ambient conditions, in which each phosphorus atom bonds with three neighboring atoms through sp^3 - hybridized orbitals, resulting in a puckered honeycomb lattice formation. This leads to high charge carrier mobility, and highly anisotropic electrical, thermal, mechanical, and optical properties [49,

50, 51]. Unlike graphene, which exhibits zero bandgap, BP has a layer-dependent bandgap, which can be tuned from around 0.3 eV to approximately 2 eV [52]. It covers the gap between graphene (zero-bandgap) and TMD (typically with larger bandgaps), showing ideal properties for various near- and mid-infrared optoelectronic applications. Hexagonal boron nitrides are naturally hyperbolic materials, composed of alternating boron and nitrogen atoms with a honeycomb lattice arrangement, sharing a similar lattice structure as graphene. Owing to their insulating properties, they can be used as a dielectric layer in many optoelectronic devices, providing atomically smooth surfaces and superb chemical stability [53]. They possess a wide bandgap of around 6 eV [54]. Different 2D materials with varying bandgaps have been utilized for various applications utilizing different wavelength regimes, which is depicted in **Fig. 1** [55]. These 2D semiconductor materials exhibit ultralightweight and excellent mechanical properties in terms of high Young's modulus and high tensile strength, which can be very beneficial in several applications, also for flexible photovoltaic devices [56-58].
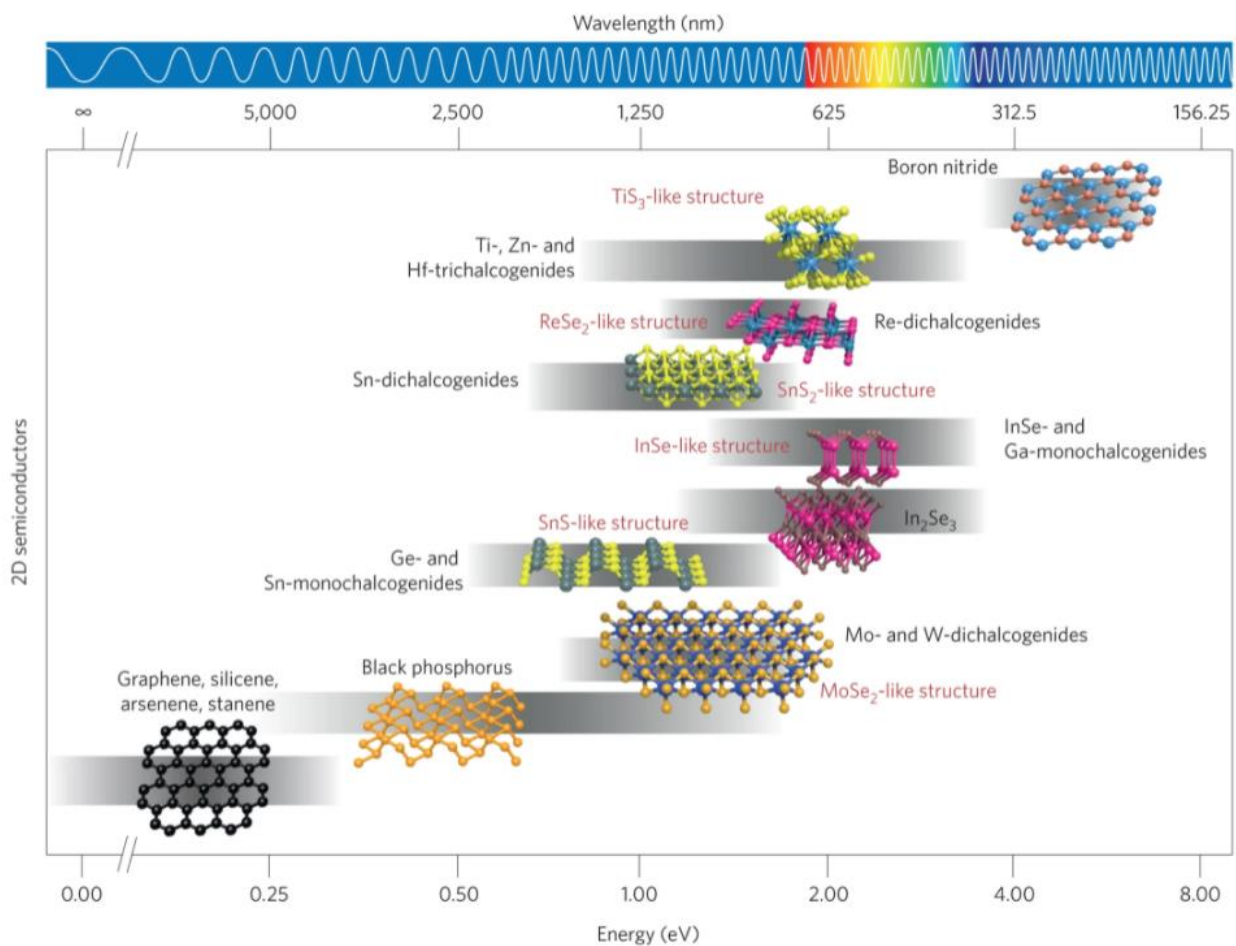

Fig. 1. Comparison of energy bandgaps of different 2D semiconductor material families studied so far. The crystal structures are also displayed to highlight the similarities and differences between the

different families. The gray horizontal bars indicate the range of bandgaps that can be spanned by changing the number of monolayers, straining or alloying. The broad bandgap range spanned by all these 2D semiconductors can be exploited in a wide variety of photonics and optoelectronics applications, such as thermal imaging, fiber optics communication, light-emitting diodes and photovoltaics. Reproduced with permission [55]. Copyright 2016, Nature Publishing Group.

2D materials have a lot of potential for use in efficient and stable thin-film solar cells, which can benefit from already established R2R processing production techniques. 2D materials are mainly used as electrodes, hole (HTL) or electron (ETL) transport layers, exciton blocking layers or encapsulation barriers in thin-film organic/perovskite solar cells. **Fig. 2** gives an overview of the different 2D materials used for PV applications, divided into the two main families of graphene and its derivatives, and 2D materials beyond graphene, i.e., transitional metal dichalcogenides (TMD), MXene, black phosphorous (BP) and boron nitrides. These are reviewed in this work.
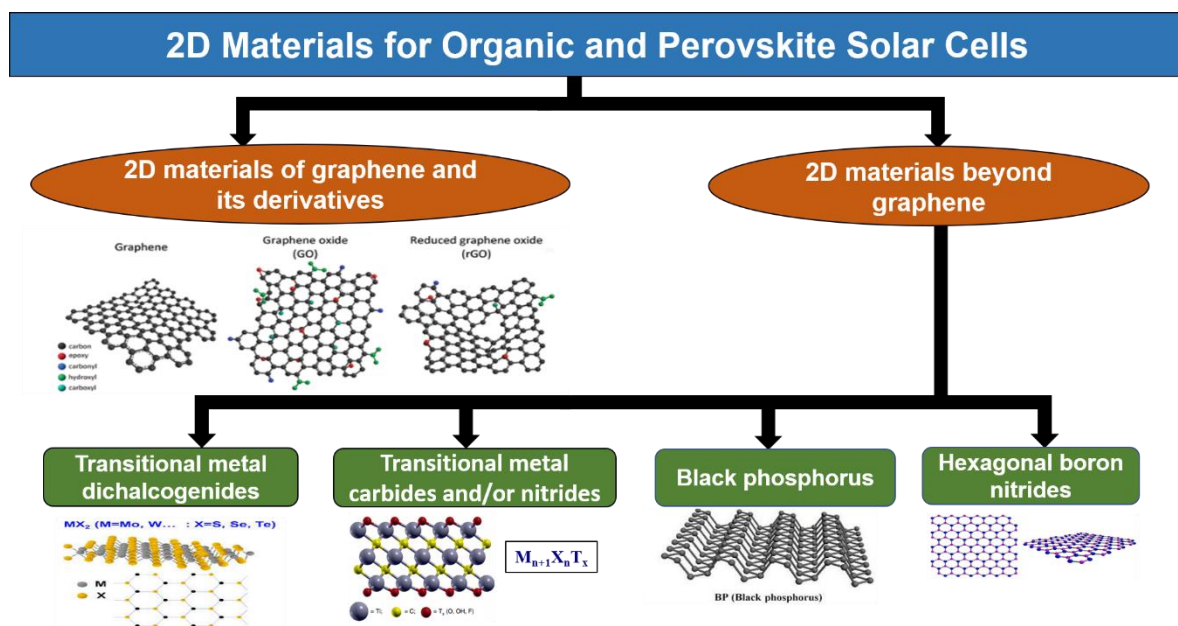

Fig. 2. Schematic representation of the different types of 2D materials for applications in various thin-film PV applications, i.e., organic and hybrid photovoltaics, reviewed in this work.

2. Organic Solar Cells

2.1 Graphene-based organic solar cells

Graphene possesses unique optical, electrical, and physical properties making it a very attractive candidate for thin-film device applications, especially OPV. Due to their high transparency and low sheet resistance, FTO and ITO are still the most used TCO in thin-film PV applications. However, despite their favorable properties, the TCO suffer from the use of rare-earth metal (indium), and their poor mechanical stability, i.e., brittleness, making their introduction into flexible devices challenging [59-63]. The high transparency and conductivity, optimum surface morphology, tunable work function, mechanical flexibility, full material abundance, and lower processing costs provided by graphene could enable future commercialization and industrialization of ITO-free electrode OPV [64,65]. The most applied derivatives of graphene are graphene oxides (GO is an oxidized single or multi-layered graphene), and reduced graphene oxides (r-GO), which opens up for bandgap and work function tuning, for example, as needed for PV interlayers. For hole transport layers, HTL, p-type wide bandgap semiconductors possessing large work functions that match the valence band/HOMO level of the active layer (donor material in OPV) are typically employed. Well-known candidates are PEDOT:PSS and high work function metal oxides such as molybdenum oxide [66-69]. P-type graphene, as well as graphene oxide and its derivatives, have demonstrated ohmic extraction properties and charge carrier selectivity for holes (exciton and electron blocking) in OPV [70-73], making them promising HTL alternatives. For electron transporting layers (ETL), low work function and electron selectivity are required, which can be provided by e.g., high bandgap n-type semiconductors. Typically, lithium fluoride (LiF), metal oxide semiconductors such as ZnO, TiO_x, SnO_x, or conjugated polymers are used as ETL in highly efficient OPV [69,74-80]. Graphene derivatives such as n-doped graphene oxide composites exhibit relatively high conductivity with sufficiently low work functions, making them suitable for efficient electron extraction as already demonstrated in some, although fewer, examples in the literature. The results of photovoltaic device performance obtained using graphene and its derivatives in OPV are summarized in **Table 1**.

Table 1. Summary of photovoltaic parameters using graphene, GO or r-GO in OPV. Graphene has been used either as a transparent conductive electrode (cathode or anode) or as a transport layer.

Cell Configuration	V_{OC} (V)	J_{SC} (mA/cm^2)	FF (%)	PCE (%)	Ref.
Graphene/PEDOT:PSS/P3HT:PC$_{61}$BM/LiF/Al	0.55	6.05	51.3	1.7	81
Graphene/PEDOT:PSS/DBP:C$_{60}$/BCP/Al	0.88	5.69	60.0	3.0	82
Graphene/PEDOT:PSS/P3HT:PC$_{61}$BM/Ca/Al	0.57	8.90	48.0	2.6	83
Graphene/PEDOT:PSS:PFI/PCDTBT:PC$_{71}$BM/Ca/Al	0.90	8.83	54.7	4.3	84
Graphene/ZnO/PTB7:PC$_{71}$BM/MoO$_3$/Ag	0.72	14.10	69.5	7.1	85
Graphene/PEDOT:PSS/MoO$_3$/PTB7:PC$_{71}$BM/Ca/Al	0.72	14.40	58.7	6.1	85
Graphene/PEDOT:PSS/PTB7-F40: PC$_{71}$BM/TiO$_x$/Al	0.68	12.10	67.0	5.5	86
Graphene/ZnO/PDTP-DFBT:PCBM/MoO$_3$/graphene	0.67	12.40	45.0	3.7	87
Graphene/PEDOT:PSS/PTB7:PC$_{71}$BM/Ba/Al	0.72	9.97	59.3	4.2	88
ITO/GO/PTB7:PC$_{71}$BM/LiF/Al	0.72	15.21	67.7	7.4	89
ITO/GO/P3HT:PC$_{61}$BM/Ca/Al	0.59	9.33	66.7	3.6	90
ITO/GO/PTB7:PC$_{71}$BM/Ca/Al	0.68	14.70	71.0	7.2	91
ITO/F-rGO/PTB7-Th:PC$_{71}$BM/PFN/Al	0.78	16.89	64.8	8.6	92
ITO/GO-Cl/PTB7:PC$_{71}$BM/GO-Li/TiOx/Al	0.76	19.59	60.5	9.1	93
ITO/PEDOT:PSS/P3HT:PC$_{61}$BM/r-GO-pyrene-PCBM/Al	0.64	9.78	62.0	3.9	94
ITO/PEDOT:PSS/PCDTBT:PC$_{71}$BM/GO/Al	0.86	12.36	63.0	6.7	95
ITO/PEDOT:PSS-GO/PM6:Y6/PDINO-G/Al	0.85	25.65	75.6	16.5	96
ITO/ZnO/PDINO-G/PM6:Y6/MoO$_3$/Ag	0.82	25.12	76.2	15.7	96
ITO/PEDOT:PSS/PTB7:PC$_{71}$BM/ZnO-RGO/Al	0.72	15.19	68.6	7.5	97
ITO/IT-RGO/ZnO:IT-RGO/PTB7-Th:PC$_{71}$BM/ MoO$_3$/Ag	0.78	18.61	65.4	9.5	98
ITO/PEDOT:PSS/PCDTBT:PC$_{71}$BM/GO-Li/TiO$_x$/Al	0.89	12.51	56.5	6.3	99

Wang et al. reported in 2009 on transparent, highly conducting few-layered graphene films as anode for OPV, produced by chemical vapor deposition method [81]. The non-covalent modification of the graphene films with 1-pyrenebutyric acid N-hydroxysuccinimide ester for the device architecture of graphene/PEDOT:PSS/P3HT:PC_{61}BM/LiF/Al exhibited a PCE of 1.71 %, which was about 55 % of that from a control devices based on ITO (PCE of 3.1 %). This result exemplifies the substitution of ITO in photovoltaic and electroluminescent devices with low-cost graphene-based films. Park et al. presented OPV devices with graphene anodes using the device structure of graphene/PEDOT:PSS/DBP:C_{60}/BCP/Al [82]. The graphene-based devices yielded a PCE of 3.01 %, while ITO-based reference devices achieved 3.20 %. The authors used vapor printing of PEDOT:PSS on the graphene surface, which supported well-defined patterns with smooth and complete coverage of PEDOT:PSS on the graphene electrodes for the improved performance of the graphene-based OPV. C. S. Hsu reported on large-area coverage of graphene sandwiching a thin layer of tetracyanoquinodimethane (TCNQ) to be used as a transparent electrode/HTL. [83]. The layer-by-layer molecularly doped graphene/tetracyanoquinodimethane (TCNQ)/graphene stacked films were used for P3HT:PC_{61}BM cells resulting in an average PCE of 2.58 %, mainly due to a significantly increased hole carrier concentration and decrease in the sheet resistance. Kim et al. presented graphene sheets (synthesized by chemical vapor deposition) as transparent conducting anode on polyethylene terephthalate (PET) substrates with a device structure of graphene/PEDOT:PSS:PFI/PCDTBT:PC_{70}BM/Ca/Al [84]. The perfluorinated ionomers (PFI) were added to pristine PEDOT:PSS to help forming a uniform PEDOT:PSS film on a graphene anode. A systematic study where the effect of the number of graphene layers (1 layer up to 7 layers) on the performance parameters of OPV was investigated, revealing that 3-layer graphene electrodes were ideal for OPV devices reaching a PCE of 4.33 %, mainly due to a sufficiently low series resistance (R_s), higher shunt resistance (R_{sh}) and relatively high transmittance. Park et al. published on the application of graphene as both anode and cathode electrodes in PTB7:PC_{71}BM OPV devices (shown in **Fig. 3a and 3b**) [85]. The graphene anode- or cathode-based devices were realized on flexible PEN substrates (**Fig. 3c**), and exhibited PCE of 6.1 % and 7.1 %, respectively, as illustrated in **Fig. 3d**. The flexible OPV also showed good stability under different bending conditions, demonstrating no performance drop after 100 flexing cycles using a bending radius of around 5 mm. Lee et al. also reported the use of PEDOT:PSS coated graphene (synthesized by chemical vapor deposition) as a transparent flexible electrode for PTB7-F40:PC_{71}BM devices [86]. The graphene layer coated with PEDOT:PSS exhibited significant enhancement reaching PCE of 5.5 % for standard configuration on

a glass substrate, PCE of 4.8 % for standard configuration on a flexible substrate, and PCE of 6.0 % for the inverted devices on a glass substrate. Song et al. reported graphene to be used in OPV as both the anode and the cathode, using a newly developed method for room temperature dry-transfer to fabricate flexible, transparent electrodes used in OPV [87]. The flexible devices were fabricated on polyethylene naphthalate (PEN) substrates with the device configuration of graphene/ZnO/PDTP-DFBT:PCBM/MoO$_3$/graphene achieving a PCE of 3.7 %, whereas using the same device configuration on rigid glass substrate improved the PCE to 4.1 %. Impressively, the graphene-based devices on flexible substrates exhibited optical transmittance higher than 60 % across the visible spectrum, demonstrating the potential of graphene for use in transparent solar cells with high transmittance, robustness and capacity to withstand significant mechanical bending without hampering the device performance. Ricciardulli et al. reported on the use of solution-processed transparent electrodes based on electrochemically exfoliated graphene applied as the anode in OPV devices [88]. The resulting graphene film exhibited relatively low sheet resistance, R_S ranging from 0.52 kΩ sq^{-1} at 70 % visible transmittance to 0.18 kΩ sq^{-1} at 55 % visible transmittance. On flexible PEN substrates, they achieved a PCE of 4.23 % using a device stack of graphene/PEDOT:PSS/PTB7:PC$_{71}$BM/Ba/Al, and thus demonstrating a route towards solution-processable, high-quality graphene as a transparent electrode in optoelectronic devices.

Murray et al. reported graphene oxide as a hole transport layer (HTL) for ITO/HTL/PTB7:PC$_{71}$BM-based OPV devices (illustrated in **Fig. 3e**) [89]. The J(V) characteristics of devices based on PEDOT:PSS and graphene oxide are similar, showing nearly identical PCE of 7.46 % and 7.39 % for the PEDOT:PSS and graphene oxide HTL, respectively (**Fig. 3f**). However, OPV devices fabricated using graphene oxide showed higher stability in accelerated thermal lifetime testing as depicted in **Fig. 3g**, presenting a clear advantage over PEDOT:PSS-based cells. The long-timescale degradation of the graphene oxide HTL is likely associated with edge-in diffusion of water and oxygen through the photoactive layer rather than an interfacial layer mediated failure mechanism as observed for the PEDOT:PSS due to its hygroscopic nature. This resulted in a 5-times enhancement in the thermal aging lifetime of the graphene oxide versus analogous PEDOT:PSS-based devices, and a 20-times enhancement in the humid ambient aging lifetime. Yun et al. reported on solution-processable r-GO as a novel alternative to PEDOT:PSS as HTL for OPV devices [90]. Conventional r-GO and a newly reduced graphene oxide (pr-GO), where p stands for the novel reductant p-toluenesulfonyl hydrazide (p-TosNHNH$_2$), were explored and used simultaneously for a comparative study towards high-performance OPV. The pr-GO devices demonstrated the best photovoltaic

characteristics with a PCE of 3.63 % based on ITO/HTL(r-GO or pr-GO)/P3HT:PC$_{61}$BM/Ca/Al devices. Moreover, the devices again showed stronger enhanced stability as compared to PEDOT:PSS-based devices. Yeo et al. reported on sulfonic acid-functionalized reduced graphene oxide (r-GO) as an HTL for OPV [91]. The solution-processable chemically converted graphene, sr-GO, functionalized with a sulfonic acid group on the edge and basal plane, exhibited good compatibility even with deep-lying HOMO level materials, via the improved work function and the presence of an interfacial dipole. It was used with different donor materials in OPV which resulted in PCE of 3.64 %, 4.80 %, 7.18 %, and 7.18 %, for P3HT, TQ1, PTB7 and PBDTTT-CF cells, respectively, employing a device configuration of ITO/graphene oxide/polymer:PCBM/Ca/Al (respective *J(V)* curves depicted in **Fig. 3h**). Furthermore, the sr-GO-based cells showed superior operational lifetime compared with those based on PEDOT:PSS. Thus, sr-GO could be an important alternative for the replacement of conventional PEDOT:PSS for the development of highly efficient stable OPV. Cheng et al. synthesized a reduced graphene oxide functionalized with fluorine atoms (F-rGO) and employed it as a HTL for OPV devices in ITO/F-rGO/PTB7-Th:PC$_{71}$BM/PFN/Al configuration [92]. The device with F-rGO as HTL enhanced the PCE to 8.6 %, as compared to 5.1 % using bare ITO, and 7.9 % using PEDOT:PSS. In addition, devices fabricated with F-rGO HTL exhibited a greatly enhanced device stability after 4600 min, retaining 63 % of its initial PCE as compared to the device with PEDOT:PSS which retained just about 23 % of its initial PCE. These results suggest that the F-rGO could be a promising hole transport material and an ideal replacement for conventional PEDOT:PSS for efficient and stable OPV cells. Konios et al. demonstrated how the WF tuning of the buffer layers can affect the performance of OPV devices and incorporated GO-Cl and GO-Li in the cells with ITO/GO-Cl/PTB7:PC$_{71}$BM/GO-Li/TiOx/Al configuration [93]. The WF of the photochlorinated GO layer and lithium-functionalized GO layer were perfectly aligned with the HOMO level of polymer donor and the LUMO level of the fullerene acceptor, respectively, resulting in excellent hole and electron transport towards the respective electrodes. The utilization of these graphene-based hole and electron transport layers in PTB7:PC71BM active layer devices resulted with PCE of 9.14 %, which is about 19 % enhancement in the PCE compared to that of the reference graphene-free device. Graphene and other 2D material-based derivatives have a great potential for such interface engineering approaches, making them excellent potential candidates for a wide range of new applications in the photovoltaic field.

Qu et al. reported a graphene-fullerene composition (r-GO-pyrene-PCBM), where PC$_{61}$BM attached to reduced graphene oxide (rGO) via the noncovalent functionalization approach, was

employed as an electron transporting layer in OPV [94]. The rGO-pyrene-PCBM was applied as ETL in the device stack of ITO/PEDOT:PSS/P3HT:PC$_{61}$BM/r-GO-pyrene-PCBM/Al, where the energy level diagram of the device with the incorporation of r-GO-pyrene-PCBM ETL is illustrated in **Fig. 3i**. The pyrene was used as the anchoring group to link PCBM and r-GO. The hybrid structure of r-GO-pyrene-PCBM was confirmed by various spectroscopic characterization, and the dispersity of r-GO-pyrene-PCBM in DMF was greatly improved due to the intramolecular π-π stacking interactions between the graphene sheet and pyrene-PCBM. The SEM images of GO, r-GO and r-GO-pyrene-PCBM with different length scales shown in **Fig. 3j**, suggest that the C$_{60}$ moiety acts as a bridge, enhancing the surface morphology. The devices with r-GO-pyrene-PCBM resulted in PCE of 3.89 %, whereas r-GO or pyrene-PCBM separately as ETL dramatically decreased the device performance (PCE of 2.53 % and 2.18 %, respectively), as illustrated in respective J(V) curves in **Fig. 3k**. These results symbolized the importance of composite formation of r-GO-pyrene-PCBM for improved electron extraction properties in OPV. Wang et al. proposed GO as ETL in a normal configuration, stretchable OPV with ITO/PEDOT:PSS/PCDTBT:PC$_{71}$BM/graphene oxide/Al structure [95]. Using graphene oxide as ETL boosted the PCE to 6.72 %, while the devices with ETL composed of graphene/TiO$_x$ achieved a PCE of 7.50 %. The graphene/TiO$_x$ yields the best PCE since it supports reduced series resistance, and improves electron charge transport. Furthermore, devices with the graphene/TiO$_x$ showed improved long-term stability when compared to reference devices, since the graphene layer helps to prevent oxygen penetration and negative moisture effects in the OPV devices. Pan et al. reported an efficient interfacial modification strategy, established by adding graphene to the classical cathode material, PDINO (PDINO–G) and employed it as ETL in both inverted and conventional OPV cells with ITO/ZnO/PDINO-G/PM6:Y6/MoO$_3$/Ag and ITO/PEDOT:PSS-GO/PM6:Y6/PDINO-G/Al configurations [96]. The dispersed graphene in PDINO–G was n-doped by the nitroxide radical of N-oxide in PDINO, and the PEDOT: PSS was doped with the GO, showing increased conductivity, reduced charge recombination and increased charge extraction rate. As such they were applied as ETL and HTL, respectively. The inverted device based on PM6:Y6 with PDINO–G showed PCE of 15.7 %, and the conventional device with both PDINO–G as ETL and PEDOT:PSS-GO as HTL exhibited a superior PCE of 16.5 %. The results reveal that the n-doped PDINO–G could be an excellent ETL for OPV and very useful in other optoelectronic devices considering its advantages of solution processability, low work function and high conductivity. Jayawardena et al. applied metal oxide/reduced graphene oxide nanohybrid composite layers as ETL for OPV cells with ITO/PEDOT:PSS/PTB7:PC$_{71}$BM/ZnO-RGO/Al structure [97]. The cells with the

solution processed ZnO/RGO ETL yielded PCE of 7.5 %, which was superior to that obtained using ZnO, BCP, TiO_2 and TiO_2/RGO. The incorporation of graphene oxide to form reduced graphene oxides with metal oxides leads to enhanced device performance, showcasing the advantageous nature of such complementary systems for electron extraction. The metal oxide/reduced graphene oxide nanohybrids also lead to more balanced electron and hole mobilities, as observed in higher FF. Therefore, incorporation of RGO with metal oxide could play a crucial role in OPV technology. Zheng et al. investigated nanostructured hybrid in situ thermally reduced graphene oxide (IT-RGO) layers, placed between the ITO and ZnO:IT-RGO hybrid layer, to form an IT-RGO/ZnO:IT-RGO hybrid ETL for use in inverted OPV cells with ITO/IT-RGO/ZnO:IT-RGO/PTB7-Th:PC_{71}BM/ MoO_3/Ag configuration [98]. The cells based on the IT-RGO/ZnO:IT-RGO yielded PCE of 9.49 % with PTB7-Th:PC_{71}BM and 8.04 % with PTB7:PC_{71}BM as the active layer. Here a one-step treatment was developed to reduce GO into IT-RGO and simultaneously assemble ZnO with IT-RGO, which significantly improves the electron conductivity of the devices and provides a well-organized, smooth nanostructure thin films with suitable energy levels for charge transfer. Thus, the hybrid ETL can boost the electron transport and extraction between the cathode and the active layer and reduce carrier recombination in the devices. This indicates the great potential in providing a facile pathway to fabricate large-scale, fast fabrication, and high performance OPV. Kakavelakis et al. presented lithium-neutralized graphene oxide (GO-Li) as ETL for OPV [99]. The GO-Li, developed with a high-throughput process, decreases the work function to -4.27 eV from the -4.95 eV (work function of GO). The resultant GO-Li material used as bilayer buffer structure with a device configuration of ITO/PEDOT:PSS/PCDTBT:PC_{71}BM/GO-Li/TiO_x/Al enhanced the PCE to 6.29 %, while the devices without the additional GO-Li layer showed PCE of only 5.51 %. The J(V) characteristics of devices without an ETL layer and with ETL layers of TiO_x, GO, and GO/TiO_x are depicted in **Fig. 3l.** The bilayer (GO-Li/TiO_x) buffer stack plays a crucial role in improving the ohmic contact between the ETL and the cathode, as well as the built-in potential of the device, which supports improved charge carrier transport. Additionally, stability investigations on such stacks reveal that for TiO_x as ETL, the PCE drops to 42 % of the initial value after 24 h of continuous exposure under 1 sun irradiation, whereas for GO-Li/TiO_x as ETL, a slower degradation rate was observed, preserving approximately 56 % of the initial PCE. The improved stability was assigned to GO-Li/TiO_x acting as an extra protection or passivation layer against oxygen (and humidity), and providing better device stability during prolonged illumination. In both devices, the degradation rate was almost saturated after ~100

h of solar irradiation, and the single-layer ETL (TiO_x) devices demonstrated $\sim$27 % of its initial PCE as compared to the bilayer ETL (GO-Li/TiO_x) devices that retained only 5 % of its initial PCE value.
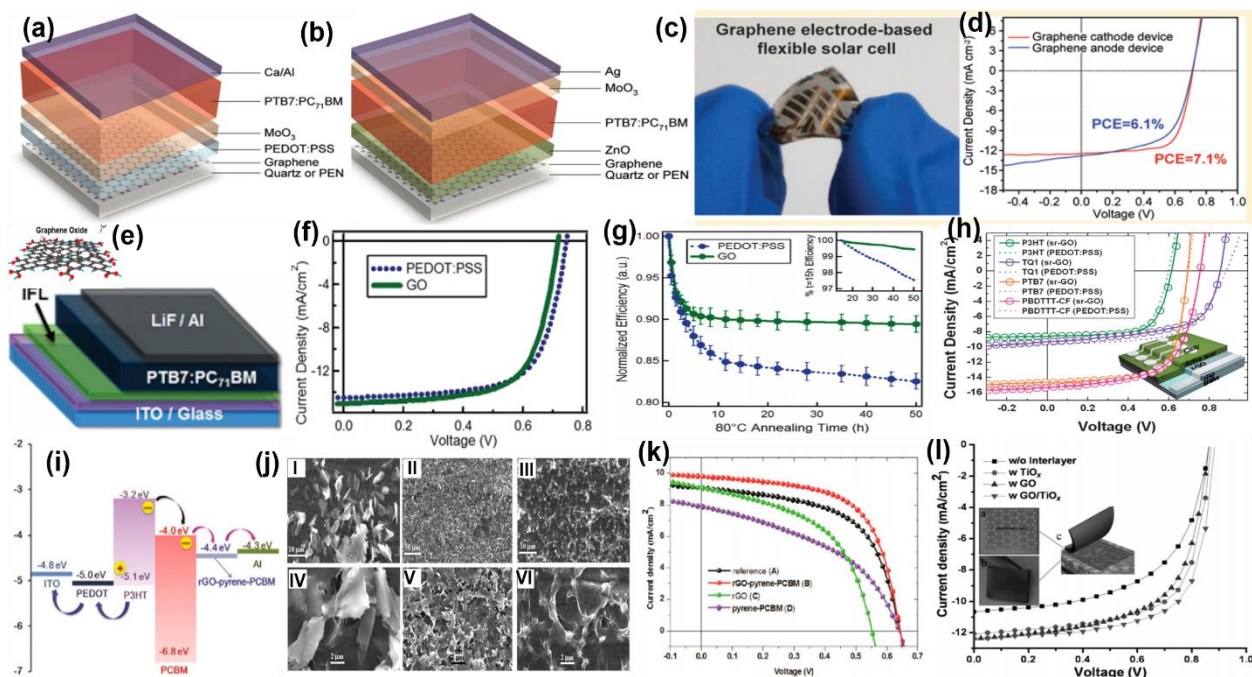
Fig. 3. Schematic diagram of (a) normal (b) inverted OPV, (c) representative image of graphene electrode solar cells and (d) AM 1.5G *J(V)* characteristics of a graphene-based device, where graphene has been used as cathode and anode. Reproduced with permission [85]. Copyright 2014, American Chemical Society. (e) Schematic of a standard OPV indicating the location of the interfacial layers, (f) *J(V)* characteristic under AM 1.5G spectrum for OPV fabricated with PEDOT:PSS and GO interfacial layers, (g) durability characteristics of PTB7:PC$_{71}$BM solar cells with PEDOT:PSS and GO interfacial layers, thermal degradation of encapsulated devices at 80 $^{\circ}$C in N$_2$ atmosphere. Inset: plot of the data between 15 and 50 h, normalized with respect to the PCE after 15 h. Reproduced with permission [89]. Copyright 2011, American Chemical Society. (h) *J(V)* curves of OPV made with different donor polymers, and employing sr-GO as the anode interfacial layer, compared against the conventional PEDOT:PSS-based devices as reference. Reproduced with permission [91]. Copyright 2014, Royal Society of Chemistry. (i) Energy level diagram of ITO/PEDOT:PSS/P3HT:PC$_{61}$BM/r-GO-pyrene-PCBM/Al, bulk heterojunction OPV device with the incorporation of r-GO-pyrene-PCBM as the electron extraction layer, (j) SEM images of GO (I and IV), r-GO (II and V) and r-GO-pyrene-PCBM (III and VI) at different length scales, (k) *J(V)* curves of the P3HT:PC$_{61}$BM, BHJ-PSC without (A) and with different electron extraction layers of rGOpyrene-PCBM (B), rGO (C), and pyrene-PCBM (D). The devices were thermally annealed and the measurements were carried out under AM 1.5 irradiation at an irradiation intensity of 100 mW/cm^{-2}. Reproduced with permission [94]. Copyright 2013, American Chemical Society. (l) *J(V)* characteristics of devices from

PCDTBT:PC$_{71}$BM BHJ without an ETL layer and with ETL layers of TiO$_x$, GO, and GO/TiO$_x$. Reproduced with permission [99]. Copyright 2014, American Chemical Society.

2.2 2D materials beyond graphene for organic solar cells

2D materials beyond graphene, such as transitional metal dichalcogenides, MXene, hexagonal boron nitrides and black phosphorus, have been representing an alternative class of materials that could potentially be utilized in OPV as an HTL or ETL interfacial layer with an added protective functionality. The charge transport layer engineering plays one of the key roles for the optimum operation of the OPV, to facilitate the extraction of the photogenerated carriers and their effective transport to the respective electrodes. The schematic diagram of 2D materials used as HTL, ETL and additive in photoactive layer in OPV is shown in **Fig. 4**.
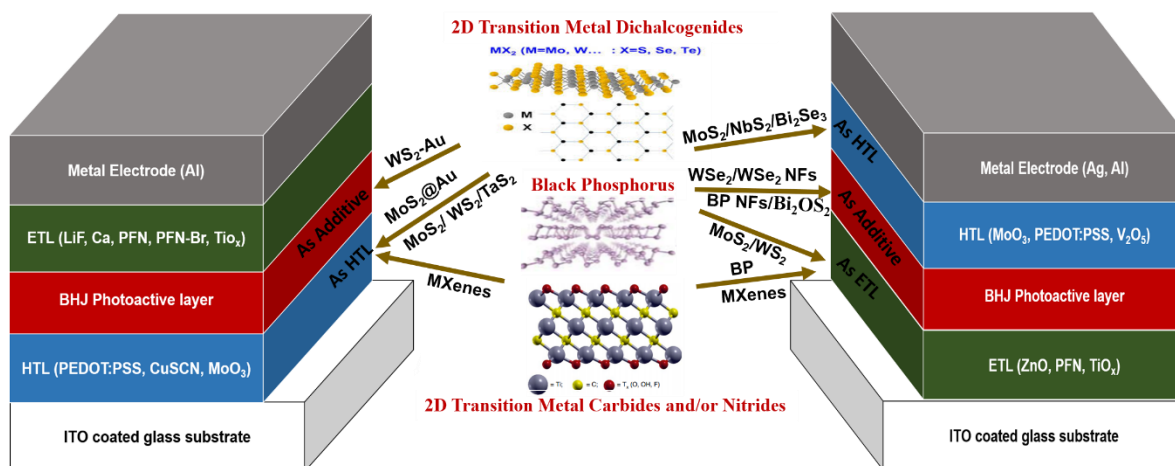

Fig. 4. Schematic diagram of the conventional and inverted OPV architectures. The illustration in the center depicts the 2D semiconductors used in the different layers.

2.2.1 2D hole transport materials for organic solar cells

The conductive conjugated polymer poly(3,4-ethylenedioxy-thiophene):poly(styrenesulfonate) (PEDOT:PSS) is one of the most widely used HTL for OPV. However, since PEDOT:PSS is acidic and hygroscopic, it could cause the degradation of the commonly used TCO materials such as ITO, as well as of the metal electrodes [100,101]. Transition metal oxides such as V$_2$O$_5$, MoO$_3$, WO$_3$ and NiO, have been applied to overcome those issues. [102-104] These materials may require high

annealing temperatures, and alternative materials, such as 2D semiconductors, have been investigated as possible alternatives. 2D semiconductors can be used as HTL in highly efficient OPV, owing to their compatibility with various OPV processing techniques, e.g., solution processing, and in particular, their ability to tune the work function, passivate the interfaces, and transport the charge carriers. A variety of 2D materials that have been investigated as HTL in the normal and inverted configuration of OPV are summarized in **Table 2**.

Table 2. Summary of results for 2D materials based HTL used in OPV

| Cell Configuration	V_{OC} (V)	J_{SC} (mA/cm^2)	FF (%)	PCE (%)	Ref
ITO/p-doped MoS$_2$/P3HT:PC$_{61}$BM/Ca/Al	0.59	8.62	66.2	3.4	105
ITO/ZnO/PTB7:PC$_{71}$BM/MoS$_2$/Ag	0.72	15.86	71.0	8.1	106
ITO/ZnO/PTB7:PC$_{71}$BM/NbSe$_2$/Ag	0.72	16.04	70.0	8.1	107
ITO/MoS$_2$/P3HT:PC$_{61}$BM/LiF/Al	0.50	7.74	63.0	2.4	108
ITO/TaS$_2$/P3HT:PC$_{61}$BM/LiF/Al	0.61	7.87	64.0	3.1	109
ITO/MoO$_3$/MoS$_2$/PBDTTT-CF:PC$_{71}$BM/Ca/Al	0.77	13.28	68.3	7.0	110
ITO/MoS$_2$/PTB7:PC$_{71}$BM/PFN/Al	0.73	14.98	69.9	7.6	111
ITO/MoS$_2$@Au/PTB7:PC$_{71}$BM/PFN/Al	0.72	15.44	65.2	7.3	112
ITO/WS$_2$/P3HT:PC$_{61}$BM/LiF/Al	0.49	8.06	61.0	2.4	113
ITO/WS$_2$/PEDOT:PSS/P3HT:PC$_{61}$BM/LiF/Al	0.52	8.71	67.7	3.1	113
ITO/ZnO/P3HT:PC$_{61}$BM/L-Bi$_2$Se$_3$/Ag	0.65	9.91	68.0	4.4	114
ITO/CuSCN/AMQS/PTB7-Th:PC$_{71}$BM/BCP/Al	0.79	17.10	65.2	8.8	115
ITO/MoS$_2$/PBDB-T-SF:PC$_{71}$BM/PFN-Br/Al	0.84	20.00	71.0	12.0	116
ITO/WS$_2$/PBDB-T-2F:Y6/PFN-Br/Al	0.84	25.90	73.0	15.8	116
ITO/WS$_2$/PBDB-T-2F:Y6:PC$_{71}$BM/PFN-Br/Al	0.84	26.00	78.0	17.0	116
ITO/MXene/PBDB-T:ITIC/Ca/Al	0.89	15.98	64.0	9.0	117
ITO/MXene/PBDB-T:ITIC/PFN-Br/Al	0.88	17.85	67.1	10.5	118
ITO/PEDOT:PSS/Ti$_3$C$_2$T$_X$/PM6:Y6/PFN-Br/Al	0.83	25.63	68.4	14.6	119
ITO/Mo$_{1.33}$C:PEDOT:PSS/PTB7-Th:PC$_{71}$BM/LiF/Al	0.80	16.86	68.7	9.2	120
ITO/PEDOT:PSS@α-In$_2$Se$_3$/PBDB-T:ITIC/PDINO/Al	0.91	17.31	71.1	11.2	121
ITO/PEDOT:PSS@α-In$_2$Se$_3$/PM6:Y6/PDINO/Al	0.84	25.47	74.5	15.9	121
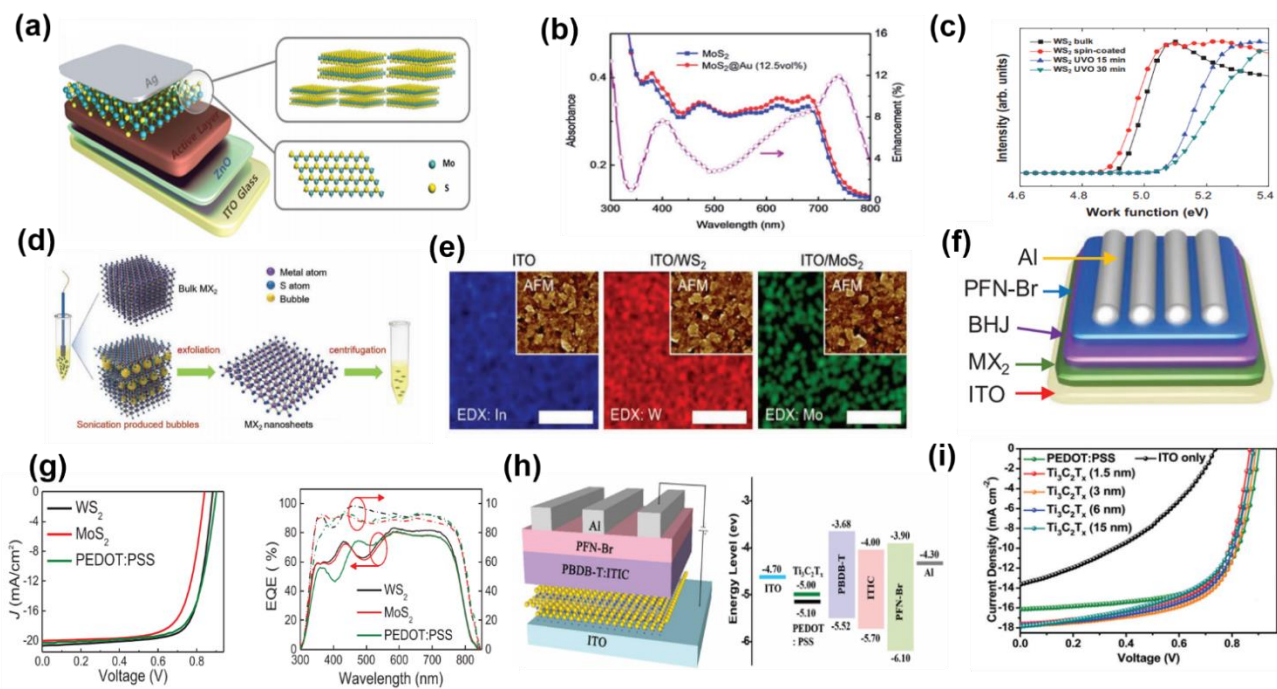
Fig. 5. (a) Schematic of inverted organic solar cells with MoS_2 buffer layer (side view) and the monolayer flakes of MoS_2 (top view). Reproduced with permission [106]. Copyright 2013, Wiley-VCH. (b) UV-Vis absorption spectra of PTB7:$PC_{71}BM$ BHJ films with MoS_2 HTL and multi-functional MoS_2@Au HTL, alongside the absorption enhancement after the incorporation of Au NPs onto MoS_2 sheets. Reproduced with permission [112]. Copyright 2014, Royal Society of Chemistry. (c) Change in the work function (measured from photoemission) of WS_2 in the bulk, spin-coated, and after UV-ozone treatment for 15 and 30 min. Reproduced with permission [113]. Copyright 2014, Wiley-VCH. (d) Schematic illustrating the process for sonication-assisted liquid exfoliation, which is used to prepare the MoS_2 and WS_2 suspensions, (e) element mapping of indium in ITO, tungsten in ITO/WS_2 (red), and molybdenum in ITO/MoS_2 (green), obtained using dispersive X-ray spectroscopy (EDX) (scale bar: 2 μm). Insets show the corresponding AFM images of the surface topography of each sample (1.3×1.3 μm), (f) schematic of the standard cell architectures employed, (g) $J(V)$ curves with quantum efficiency (QE) curves of PBDB-T-SF:IT-4F solar cells using WS_2, MoS_2, and PEDOT:PSS as the HTL. Reproduced with permission [116]. Copyright 2019, Wiley-VCH. (h) Schematic of the OPV architecture with the energy band diagrams of used materials, (i) $J(V)$ characteristics of devices with different HTL. Reproduced with permission [118]. Copyright 2019, Royal Society of Chemistry.

In 2013, Yun et al. reported the application of MoS_2 as an HTL in OPV [105]. By tuning the work function of MoS_2 and by applying p-type doping (with gold chloride trihydrate), the transport layer was more finely tuned to the energy level of the P3HT:PCBM absorber, resulting in an enhancement of PCE of ITO/MoS_2/P3HT:$PC_{61}BM$/Ca/Al devices to 3.38 %, as compared to the undoped MoS_2 devices with 2.84 %. Gu et al. reported ultrathin MoS_2 nanosheets as HTL in inverted OPV with ITO/ZnO/BHJ/MoS_2/Ag layout as depicted in **Fig. 5a** [106]. The PTB7:$PC_{71}BM$ and P3HT:$PC_{61}BM$ devices having MoS_2 nanosheets as HTL resulted in PCE of 8.11 % and 4.03 %, respectively, which was higher than the PCE of devices based on thermally evaporated MoO_3 with 7.54 % and 4.02 %, respectively. The untreated ultrathin MoS_2 nanosheets are superior in the transport of holes with a lower density of trapped states for the photogenerated charges. Furthermore, Gu et al. used a thin-layer of $NbSe_2$ nanosheets as an alternative hole transport layer to replace MoO_3 in OPV. [107] The $NbSe_2$ nanosheet acted as a well-functioning HTL, where the unique flake-like 2D structure provided a lower trap density and a suitable electrical dipole for charge extraction and suppression of charge recombination. As a result, a PCE of 8.10 % was obtained with PTB7:$PC_{71}BM$ inverted OPV, higher than using vacuum-deposited MoO_3. Le et al. presented MoS_2 nanosheets, formed through a simple sonication exfoliation method, employed as an HTL between ITO and P3HT:$PC_{61}BM$ photoactive layer [108]. While the initial work function of the non-treated MoS_2 was -3.9 eV, it decreased to -4.9 eV and further to -5.2 eV upon UVO-treatment for 15 min and 30 min, respectively. This adjustment of the work function resulted in further enhancement in the PCE of the final devices to 2.44 %. Furthermore, by inserting PEDOT:PSS between MoS_2 and the photoactive layer, the PCE improved to 2.81 %, which is comparable to that of the devices employing only PEDOT:PSS. The use of MoS_2 nanosheets significantly improved the device stability by protecting the ITO surface from the acidic nature of PEDOT:PSS. In addition, Le et al. reported the application of TaS_2 as an HTL in OPV with ITO/TaS_2/P3HT:$PC_{61}BM$/LiF/Al device stack, in which the PCE was improved to 3.06 % from 1.8 % for reference without TaS_2 [109]. The work function of TaS_2 changed to -4.95 eV from -4.4 eV after UVO-treatment, which was better fitting for hole extraction. Yun et al. applied MoS_2 nanosheets, synthesized via a one-step oxidation/exfoliation of bulk MoS_2 powder using H_2O_2 [110]. MoS_2 nanosheets with MoO_3 nanoparticles as HTL were effective in overcoming the disadvantages of PEDOT:PSS regarding its stability issues. The MoO_3/MoS_2 HTL used with PBDTTT-CF:$PC_{71}BM$ photoactive layer resulted in a PCE of 6.9 % with improved air-stability, whereas PEDOT:PSS HTL reached 6.8 % and a comparatively poorer stability. Furthermore, MoO_3/MoS_2 provides chemical neutrality and uniform surface morphology of the layer. Yang et al. reported the effect of the post-

treatments of the chemically exfoliated MoS_2 (ce-MoS_2) and its effect on the device performance of OPV [111]. Applying 2D MoS_2 sheets as hole extraction layer for OPV with ITO/MoS_2/ PTB7:$PC_{71}BM$/PFN/Al layout yielded a PCE of 7.64 %, which is 53 % higher than that of the OPV with as-deposited ce-MoS_2, and comparable to the PCE of 7.6 % obtained with PEDOT:PSS.

By taking advantage of plasmonic effects that arise from the incorporation of metallic nanoparticles in OPV, mainly the light absorption, but potentially also the charge extraction, and the performance of OPV, could be directly improved. By incorporating metallic nanoparticles made of Au and Ag into the HTL, the light absorption and charge extraction can be effectively improved. Yang et al. reported using Au NPs on 2D MoS_2 to promote a near-field enhanced optical absorption and improve the performance of OPV [112]. The MoS_2@Au composite layer enhanced the absorption spectrum of the PTB7:$PC_{71}BM$ devices, without disturbing the morphology of the photoactive layer. **Fig. 5b** illustrates the significant absorption enhancement of the PTB7:$PC_{71}BM$ films with MoS_2@Au as the HTL, compared to the same films when HTL composed of MoS_2 alone was employed. The plasmonic OPV devices with MoS_2@Au HTL resulted in a PCE of 7.25 %, corresponding to an enhancement of 17.3 % compared to the devices with an HTL consisting of 2D MoS_2 alone. Q. V. Le et al. reported the UVO-treated WS_2 HTL with a tunable work function, making it suitable to adjust and improve the charge extraction from P3HT to ITO [113]. After applying a sonication exfoliation method, WS_2 nanosheets were used as the HTL, where UVO-treatment adjusted the work function to -5.1 eV (optimum UVO-treatment for 30 min shown in **Fig. 5c**). A PCE of 2.4 % was obtained, while for the OPV without WS_2 it was 1.84 %. Furthermore, a combined WS_2/PEDOT:PSS layer was also examined and the PCE of 3.07 % was achieved, which is higher than using PEDOT:PSS alone, with 2.87 %. Yuan et al. reported layered Bi_2Se_3 as HTL in P3HT:$PC_{61}BM$ inverted OPV [114]. The high conductivity and ideal energy level alignment for this HTL resulted in a PCE of 4.37 % with a superior stability compared to the MoO_3 based devices with a PCE of 3.91 %.

Wang et al. in 2019 reported a 2D material, antimonene quantum sheets (AMQS) used with CuSCN as an HTL for OPV [115]. The bilayer CuSCN/AMQS used in the cell configuration ITO/CuSCN/AMQS/PTB7-Th:$PC_{71}BM$/BCP/Al obtained a PCE of 8.8 %, which was more than 12 % higher compared to the reference cells fabricated with pure CuSCN as an HTL (PCE of 7.86 %). To further extend this research, the authors tested CuSCN/AMQS HTL with two non-fullerene systems of PBDBT-2F:IT-4F and PTB7-Th:ITIC, where they obtained a PCE of 10.14 % and 7.15 % for PBDBT-2F:IT-4F and PTB7-Th:ITIC, respectively. Those PCE were 10 % higher for PBDB-T-2F:IT-4F and 5 % higher for PTB7-Th:ITIC-based cells containing CuSCN/AMQS HTL as compared

to the reference cells containing CuSCN HTL. The enhancement in photovoltaic performance with the insertion of AMQS was suggested to be a result of diminished recombination loss or exciton blocking, as it helps to passivate surface defects of CuSCN. Stability studies were conducted to compare the effect of these HTL on the long-term performance of ITO/HTL/PTB7-Th:PC$_{71}$BM/BCP/Al devices in a nitrogen-filled glovebox without encapsulation. The CuSCN/AMQS HTL based devices retained 68 % of the initial PCE, compared to 66 % of initial PCE for the CuSCN cells, and only 8 % for PEDOT:PSS after one month.

Lin et al. reported on the use of liquid exfoliated WS$_2$ and MoS$_2$ nanosheets as solution-processed HTL in a highly efficient non-fullerene acceptor (NFA) based OPV [116]. The measured work function of WS$_2$ (-5.2 eV) and MoS$_2$ (-5.4 eV) when coated on ITO was significantly higher than that of PEDOT:PSS (−4.8 eV). The spin-coated WS$_2$ exhibited better coverage on the ITO surface compared to MoS$_2$, due to the fact that WS$_2$ was primarily composed of a few monolayer flakes (1-3 monolayers), whereas MoS$_2$ was composed of a few multilayer flakes (2–7 monolayers). **Fig. 5d** illustrates how the deposition of MoS$_2$ and WS$_2$ covers over the ITO via spin-coating. **Fig. 5e** represents the EDX measurements and AFM images of the so-called MX2 films on ITO. The schematic of the device cell architectures employed is depicted in **Fig. 5f**. Among these HTL, OPV based on PBDB-T-SF:IT-4F with WS$_2$ HTL yielded a maximum PCE of 13.5 %, which is higher than the reference cells based on PEDOT:PSS (13.1 %); whereas the maximum PCE with MoS$_2$ was 12.0 % (corresponding $J(V)$ and QE curves shown in **Fig. 5g**). The V_{OC} and J_{SC} as a function of light intensity revealed bimolecular recombination losses in each type, showing that the insertion of HTL increases the charge selectivity and reduces the leakage current due to the minority carrier recombination, thus enhancing the overall device performance. To analyze these effects, PBDBT-2F:Y6 devices with WS$_2$ HTL (PCE of 15.8 %), ternary devices based on PBDB-T-2F:Y6:PC$_{71}$BM BHJ with WS$_2$ as HTL (PCE of 17.0 %), and the same ternary blend but with PEDOT:PSS as HTL (PCE of 16.4 %), were studied. The optical and carrier recombination characteristics revealed that the enhanced performance in WS$_2$- based OPV is due to a combination of favorable photonic structure and reduced bimolecular recombination losses. These remarkable efficiencies are the highest for OPV based on 2D interfacial layers to date, indicating a way to a cost-effective 2D HTL technology for the development of the future-generation OPV.

Yu et al. presented the application of MXene, Ti$_3$C$_2$T$_x$, as HTL in a non-fullerene OPV of ITO/MXene/ PBDB-T:ITIC/Ca/Al [117]. For the proper alignment of energy levels between the ITO and the photoactive layer, UVO- treatment and treatment with N$_2$H$_4$ were performed. The

devices with MXene as HTL exhibited a PCE of 9.02 %, which was comparable to the 9.67 % PCE of the reference devices using PEDOT:PSS. Moreover, Ho et al. applied $Ti_3C_2T_x$ MXene nanosheets as HTL in OPV as shown in **Fig. 5h** [118]. The OPV with an optimized thickness of $Ti_3C_2T_x$ had a PCE of 10.53 % while the reference with PEDOT:PSS as HTL gave a PCE of 10.11 %, with the corresponding *J(V)* curves illustrated in **Fig. 5i**. The well-aligned energy levels, high conductivity, and improved morphology of the photoactive layer with the MXene were mentioned to play a role in improving the charge transport and extraction. The Mxene-based devices without any encapsulation also showed better long-term stability under atmospheric conditions than the PEDOT:PSS-based devices. Further, Hou et al. also presented PEDOT:PSS/$Ti_3C_2T_x$ composite films as an efficient HTL for OPV devices based on ITO/PEDOT:PSS/$Ti_3C_2T_x$/PBDB-T:ITIC or PM6:Y6/PFN-Br/Al [119]. For the PM6:Y6 photoactive layer, the PCE of the devices increased to 14.55 % from 13.10 % for the PEDOT:PSS reference devices, and for PBDB-T:ITIC, the PCE for PEDOT:PSS/$Ti_3C_2T_x$ was measured to be 11.02 %. Interestingly, PEDOT:PSS/$Ti_3C_2T_x$ based devices also demonstrated improved long-term stability compared to PEDOT:PSS based devices. Liu et al. reported the use of $Mo_{1.33}C$ MXene mixed with PEDOT:PSS as HTL for OPV with ITO/$Mo_{1.33}C$:PEDOT:PSS/PTB7-Th:$PC_{71}BM$/LiF/Al architecture [120]. The HTL consisting of $Mo_{1.33}C$ mixed with PEDOT:PSS showed a higher device performance with a PCE of 9.24 %, compared to the pristine PEDOT:PSS devices with a PCE of 8.21 %. Further investigation into hole mobilities, charge extraction, and morphology reveals improvement in all the parameters, demonstrating that the improved hole transport properties of MXene can enhance the overall device performance. Wang et al. reported 2D α-In_2Se_3 nanosheets mixed with PEDOT:PSS with a high conductivity and suitable work function, applied in the device configuration ITO/PEDOT:PSS@α-In_2Se_3/donor:acceptor/PDINO/Al [121]. The conductivity of the PEDOT:PSS:α-In_2Se_3 HTL was enhanced to 1.54×10^{-2} S cm^{-1} upon addition of 0.15 wt. % of 2D α-In_2Se_3 nanosheets, from 2.21×10^{-3} S cm^{-1} of the pristine PEDOT:PSS, and it also demonstrated excellent optical transmittance. α-In2Se3 nanosheets with the negatively charged surface can attract the PEDOT chains, leading to a stronger interaction between PEDOT chains. This provides new conductive paths for PEDOT chains separated by PSS barriers, which may serve as physical linkers for PEDOT chains to increase the interfacial contact area between PEDOT chains and form a larger PEDOT conductive network. The PCE of devices with the PEDOT:PSS:α-In_2Se_3 HTL increased to 11.22 % from 10.21 % with pristine PEDOT:PSS HTL (for the PBDBT:ITIC system), and to 15.89 % from 14.50 % with pristine PEDOT:PSS HTL (for the PM6:Y6 system). The enhanced performance with improved J_{sc} and FF is facilitated by an enhanced hole extraction and

suppressed recombination. The composite HTL film improved also the stability of devices owing to the partial removal of the excess PSS.

2.2.2 2D electron transport and active layer additive in organic solar cells

Due to their high optical transparency, high charge carrier mobility, high stability, and aforementioned work function tunability, 2D materials have also been investigated a lot in recent years as electron transport layers (ETL) in OPV. This also goes for 2D materials used not directly on the cathode, but mixed as additives in the active bulk heterojunction (BHJ) layer in OPV. The different reported 2D materials applied as ETL and additives in BHJ system for OPV are summarized in **Table 3.**

Table 3. Summary of the results using 2D materials as electron transporting layer and the additive material in the BHJ organic solar cells

| Cell Configuration	V_{OC} (V)	J_{SC} (mA/cm^2)	FF (%)	PCE (%)	Ref.
ITO/WS$_2$/P3HT:PC$_{61}$BM/V$_2$O$_5$/Al	0.58	9.31	55.3	3.0	122
ITO/MoS$_2$/P3HT:PC$_{61}$BM/V$_2$O$_5$/Al	0.58	11.19	51.6	3.4	122
ITO/PEIE/MoS$_2$/P3HT:PC$_{60}$BM/MoO$_3$/Ag	0.65	8.17	66.7	3.5	123
ITO/PEIE/MoS$_2$/PTB7-Th:PC$_{71}$BM/MoO$_3$/Ag	0.80	17.02	66.6	9.1	123
ITO/ZnO/BP/PTB7:PC$_{71}$BM/MoO$_3$/Ag	0.72	18.78	61.0	8.3	124
ITO/MXene/PBDB-T:ITIC/MoO$_3$/Al	0.87	17.36	60.0	9.1	117
ITO/PEDOT:PSS/PCDTBT:WS$_2$-Au:PC$_{71}$BM /Ca/Al	0.89	12.30	58.4	6.3	131
ITO/PFN/PTB7:WSe$_2$:PC$_{71}$BM/MoO$_3$/Ag	0.73	17.69	71.7	9.5	132
ITO/ZnO/PTB7-Th:WSe$_2$NFs:PC$_{71}$BM/MoO$_3$/Ag	0.78	17.54	69.0	9.2	133
ITO/ZnO/PTB7-Th:BPNFs:PC$_{71}$BM/MoO$_3$/Ag	0.78	17.34	69.1	9.2	133
ITO/ZnO/PTB7-Th:IEICO-4F:BPNFs/MoO$_3$/Ag	0.71	23.44	73.0	12.2	134
ITO/ZnO/PBDB-T:ITIC:Bi$_2$OS$_2$/MoO$_3$/Ag	0.94	18.61	70.6	12.3	135
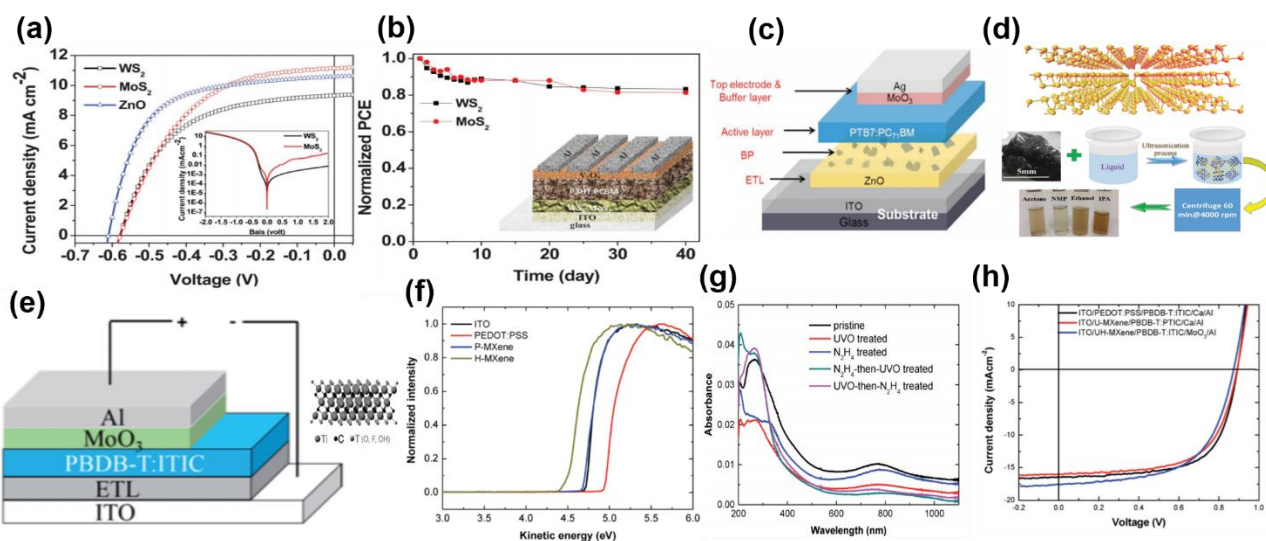
Fig. 6. (a) Illuminated *J(V)* curves of inverted device structures featuring WS$_2$ and MoS$_2$ as the buffer layer. Inset: Dark *J(V)* curves, (b) stability of solar cells featuring WS$_2$ and MoS$_2$ as electron extraction layers. Inset: inverted device structure. Reproduced with permission [122]. Copyright 2013, Royal Society of Chemistry. (c) Schematic device structure, (d) crystal structure of black phosphorous (BP) illustrating also the BP solution fabrication. Exfoliated BP in acetone, IPA, ethanol, and NMP solvents. Reproduced with permission [124]. Copyright 2016, Wiley-VCH. (e) evice architecture of the inverted device: ITO/ETL/PBDB-T:ITIC/ MoO$_3$/Al, (f) UPS spectra of bare ITO, PEDOT:PSS and MXene thin films, untreated and treated with N$_2$H$_4$, (g) absorption spectra of MXene thin films, untreated and treated with UVO and N$_2$H$_4$, (h) *J(V)* curves of PBDB-T:ITIC OPV with the inverted and normal architecture, where UH-MXene is used as the electron extraction layer in an inverted OPV, and U-MXene for hole extraction in the normal OPV, alongside with the reference devices with PEDOT:PSS as the HTL and Ca as the ETL. Reproduced with permission [117]. Copyright 2019, Royal Society of Chemistry.

Ibrahem et al. reported in 2013 on a method for solution processing of 2D nanosheets of TMD (transitional metal dichalcogenides) such as MoS_2 and WS_2 for use in OPV [122]. These were used as ETL in an inverted structure of OPV, prepared at relatively low annealing temperatures with the device architecture of ITO/TMD/P3HT:$PC_{61}BM$/V_2O_5/Al. Devices incorporating MoS_2 or WS_2 as ETL showed promising PCE of 3.35 % and 2.98 %, respectively. The MoS_2 used as ETL resulted in improved *J(V)* characteristics (higher FF), both under illumination and in dark (shown in **Fig. 6a**), which is an indication of reduced extraction barrier and recombination at the contacts compared to WS_2. **Fig. 6b** illustrates the results of the stability measurements of the devices prepared with WS_2 and MoS_2 as ETL, where there is an almost negligible drop in PCE after 40 days, as these TMD showed high stability in ambient environments and was barely affected by moisture and oxygen. Lee et al. reported MoS_2 nanosheets as an interlayer ETL in inverted OPV devices with ITO/PEIE/MoS_2/doner:acceptor/MoO_3/Ag configuration, where donor:acceptor refers to either P3HT:$PC_{60}BM$, PTB7:$PC_{71}BM$, or PTB7-Th:$PC_{71}BM$ [123]. The MoS_2 nanosheet interlayer plays an important role as a sub-photo sensitizer and an electron transport layer, and provides effective charge separation for the enhancement of device performance, with PCE of 3.5 %, 8.12 % and 9.08 % as compared to reference control device with PCE of 2.79 %, 7.15 % and 7.86 % (with P3HT:$PC_{60}BM$, PTB7:$PC_{71}BM$ and PTB7-Th:$PC_{71}BM$ as the photoactive layers, respectively). Experimentally used finite-difference-time-domain modeling and time-correlated single photon counting measurements confirmed that the MoS_2 nanosheet plays a crucial role for enhancing photovoltaic performance and electron transport mechanism of the devices. Lin et al. reported 2D black phosphorous (BP) applied as an interfacial layer with ZnO in ITO/ZnO/BP/PTB7:$PC_{71}BM$/MoO_3/Ag as illustrated in **Fig. 6c** [124]. The exfoliated BP in various solvents such as acetone, IPA, ethanol, and NMP are shown in **Fig. 6d**. The devices utilizing BP achieved a PCE of 8.25 % compared to ZnO as ETL with a PCE of 7.37 %. The optimized BP was also demonstrated to lead to a cascade band structure. Thus, with the correct work function, BP acts as an efficient ETL, which also demonstrates a better device stability in OPV, when used with a thickness of around 10 nm. Z. Yu et al. presented the application of MXene, $Ti_3C_2T_x$ as electron and hole transporting layer for ITO/MXene/PBDB-T:ITIC/MoO3/Al as illustrated in **Fig. 6e** [117]. Treating MXene with N_2H_4 or UVO was performed to adjust the work function in the range of -4.08 eV to -4.95 eV, whereas the untreated MXene showed a work function of -4.68 eV, as shown in **Fig. 6f**. The mechanisms for the work function variations are due to either oxidation or reduction of the C element of $Ti_3C_2T_x$ by UVO or N_2H_4, respectively. The MXene films also showed high transmittance

in the visible and near-infrared region, as shown in **Fig. 6g**. The OPV with MXene as ETL had PCE of 9.06 %, and as HTL had 9.02 %, comparable to those of the control OPV, as represented in *J(V)* curves in **Fig. 6h**. These highly transparent and conductive MXene could thus play a vital role in optoelectronic applications.

A few of the limiting factors for BHJ OPV are the relatively low charge carrier mobility, and relatively short exciton diffusion length [125,126]. The appropriate insertion of a third material in the photoactive layer, to form the ternary BHJ blend, could possibly minimize these limitations and result in enhanced photovoltaic parameters [127-130]. Careful selection of the 2D materials with a high charge carrier mobility, appropriate electronic band structures, solution-processability, and matching energy levels compared to the energy levels of the donor and the acceptor material, is here of utmost importance. The results regarding the utilization of 2D materials as additional component in BHJ of OPV are tabulated in **Table 3**.

Sygletou et al. reported the incorporation of WS_2-Au NPs as additive into the photoactive layers of BHJ OPV [131]. The nanoparticle (NP) density was readily controlled by laser-induced anchoring of Au NP onto the nanosheet basal plane and edges, and resulted in enhanced light harvesting that is potentially useful for OPV. The decoration process was analyzed with the variation of laser fluence, the number of pulses irradiating the mixed solution of the 2D material and metallic precursor, and the concentration of the metallic precursor in the mixed solution (1 %, 1.5 and 2.5 % v/v Au concentrations). The best performance was achieved for the 1.5 % v/v concentration of Au NP within the WS_2 solution, used in a blend absorber in ITO/PEDOT:PSS/PCDTBT:WS_2-Au:PC_{71}BM /Ca/Al devices. This resulted in a PCE of 6.3 %, more than 13 % higher than the reference system. The photovoltaic performances with reference devices and with different concentrations of Au NPs within the WS_2 are illustrated in **Fig. 7a** and **7b**. A noticeable enhancement in the photocurrent and the PCE of the respective OPV was ascribed to the plasmon-enhanced absorption of Au NPs, and the improved energy level alignment between the polymer and the intermediate WS_2 nanosheets. Kakavelakis et al. reported the incorporation of 2D materials in the BHJ blend in the inverted OPV [132]. The authors showed quantitative interplay between 2D crystals and fullerene domains sizes, in which the lateral size of the liquid phase exfoliated (LPE) WSe_2 flakes was aligned with that of the fullerene (PC_{71}BM), by combining an ultrasonication process with sedimentation based separation (SBS) to produce three different WSe_2 samples (1, 2 and 3) with a fine-tuned areas (70, 240, and 720 nm^2) and thicknesses (2.6, 6.1 and 8.5 nm), respectively. Among these three different WSe_2 flake samples, the performance of the blend having PTB7 as donor and

PC$_{71}$BM as acceptor reached PCE of 9.45 %, compared to the reference without additive devices with a PCE of 8.10 %. The schematic of the OPV with the addition of WSe$_2$ flakes in the BHJ, and the respective energy levels, are depicted in **Fig. 7c**. The optimal performance could be linked to the improved morphology of the added 2D additive component. For the study of the effect of WSe$_2$ on the charge carrier generation and transport, the photocurrent densities (J$_{ph}$) of the reference and the different additive added in BHJ cells incorporating WSe$_2$ flakes are plotted in **Fig. 7d**, with the calculation of their respective maximum exciton generation rates (G$_{max}$) and charge collection probabilities P(E, T). The highest calculated G$_{max}$ is correlated to the highest absorption of incident photons, amongst others, which resulted in an overall increased exciton generation rates for the best performing OPV. Time-resolved photoluminescence (TRPL) spectroscopy was conducted to determine the exciton lifetime, and the PL intensity decay profiles obtained for the different blends on silicon substrate are displayed in **Fig. 7e**. The corresponding effective exciton lifetimes, τ_{exc}, are determined to be 69, 59, 34, and 49 ps for the reference and samples 1, 2, and 3 of the WSe$_2$ blends, respectively. The fast decay time (i.e., 34 ps) of sample 2 of the additive based blend is associated with efficient exciton dissociation, thus with a more efficient charge carrier generation. In addition to this, the best charge carrier mobility ratio (μ_h/μ_e~1.09) improved the photovoltaic performances of OPV, using these third components in the photoactive material blend. Yang et al. compared two solutions, the exfoliated black phosphorus (BPNF) and tungsten diselenide (WSe$_2$NF), as the third component adding with the binary solution of PTB7-Th:PC$_{71}$BM [133]. These materials act as both an electrode modifier and the third component in the bulk, owing to their high charge carrier mobility and their matching electronic band structure. PCE of the devices based on WSe$_2$NFs was 9.24 % while it was 9.20 % for devices based on BP and 8.60 % for reference devices. The photoluminescence (PL) spectra of the pure donor, acceptor, donor mixed with BPNFs or WSe$_2$NFs, and acceptor mixed with BPNF or WSNF are shown in **Fig. 7f and 7g**. The PL is quenched by BPNF and WSNF, indicating efficient exciton dissociation and charge transfer between acceptor molecules and the 2D nanoflakes, which could provide efficient exciton dissociation and charge transfer pathways within the blend. **Fig. 7h** shows the Cole-Cole plot of the impedance data obtained by the electrochemical impedance spectroscopy (EIS). The reduced bulk resistance after incorporation with BPNF and WSNF could be attributed to the more efficient charge transfer pathways. **Fig. 7i** illustrates the frequency-dependent imaginary parts of impedance for different devices used for calculating the relaxation time (τ) from the reciprocal characteristic frequency (f$_{max}$), located at the peak. The calculated τ of the WSNF and BPNF was 15.8 ns and 50.1 ns, respectively, which is remarkably

smaller than that of the reference devices (79.4 ns). The lower value of τ indicates a more efficient dissociation of excitons and a faster charge transfer at the D/A interfaces of the BHJ incorporating WSNF and BPNF. The device stability under various test conditions was studied, and normalized PCE stability curves for unencapsulated devices kept at 30 ºC for 110 h at a relative humidity of 50 % are shown in **Fig. 7j**. As shown, the devices containing BPNF and WSNF retain 80 % of their initial PCE, while reference devices drop to less than 60 % of the initial PCE. Devices were also tested under continuous illumination at elevated temperatures, where the reference OPV suffered from a steep loss in PCE within 1 h and a total loss of their performance after 5 h, which was slowed down in devices with BPNF or WSNF. This could be explained by the ability of the BPNF and WSNF to partially prevent or slow down the degradation related to moisture and oxygen permeation into the BHJ blends **Fig. 7k**. Yang et al. applied 2D BPNF as a morphological modifier in the device fabrication of fullerene-free OPV device of configuration ITO/ZnO/PTB7-Th:IEICO-4F:BPNFs/MoO3/Ag [134]. The PTB7-Th:IEICO-4F blends incorporated with BPNF showed more ordered π-π stacking and promoted domain purity, contributing to lower charge transport resistance and suppressed charge recombination within the BHJ which resulted with a superior FF of 0.73 and PCE of 12.2 %. Moreover, the BPNF maintained the morphological stability of the devices probably by retarding the phase mixing in the BHJ during the aging period. The morphological stability of the OPV incorporated with BPNF was investigated by thermal treatment at 150 °C in N_2 atmosphere for various periods, and compared with those of the reference device. The device employing BPNF retained 73 % of its initial PCE after thermal treatment for over 3 h, while the reference device retained only 60 % of its initial PCE under the same condition. Notably, the VOC and FF losses were reduced in presence of BPNF. The embedded BPNF help improve the morphological stability of the devices probably by retarding the phase mixing in the BHJ during the aging period. The thermal-induced VOC and FF losses were generally attributed to aggravated phase separation and extended amorphous intermixing phase within the blends. It could be confirmed that the BPNF nanoflakes might be able to lock the refined phase separation microstructure by a spatial confinement effect, resulting in improved morphological stability of the blends. Thus, the 2D nanoflakes can act as an effective morphology modifier for efficient OPV. Huang et al. synthesized 2D Bi-based semiconductor nanomaterial (Bi_2OS_2) and introduced it into the active layer of OPV device in configuration ITO/ZnO/PBDB-T:ITIC:Bi_2OS_2/MoO$_3$/Ag [135]. When the optimized 1 wt % concentration of 2D Bi_2OS_2 is introduced into the active layer, the PCE was enhanced to 12.31 % from 10.51 %, as compared to the reference cells without Bi_2OS_2. Mainly the 2D Bi_2OS_2 plays a great

role in the improvement of charge transport, surface morphology and crystallization of active layer, which is demonstrated in an enhancement in PCE of more than 17 %. Moreover, the cell with 2D Bi_2OS_2 exhibited good stability, with about 92 % of original PCE retained upon 400 h storage (without encapsulation), as compared to the cells without 2D Bi_2OS_2 which retained only about 78 % of original PCE. The enhancement of the active layer crystallinity and the adequate surface morphology can prevent the O_2 and H_2O penetration and subsequent reactions with the active layer. While introducing excessive amounts of 2D Bi_2OS_2, a great deal of PBDB-T or ITIC are nucleated and then aggregated, resulting in drastic phase separation and surface roughness. However, with an optimized amount of 2D Bi_2OS_2 in PBDB-T:ITIC, enhanced surface morphology of the active layer was observed. Thus, the 2D Bi_2OS_2 impacted the role of the heterogeneous nucleation in the active layer, resulting in the enhanced crystallization of PBDB-T and ITIC, thus boosting the exciton dissociation and charge collection with improved charge carrier transport and reduced charge recombination. Thus, the introduction of 2D Bi_2OS_2 into the active layer shows a worthy potential application in photovoltaic devices. Overall, a lot of progress has been made in incorporating 2D materials as ETL or as a third compound in OPV active layers, in order to improve mainly charge carrier generation, charge transport and charge extraction at the cathode interface. This is mostly due to the tunability of the work function and the energy levels of the 2D materials, to enhance the electron extraction from the electron acceptor material.
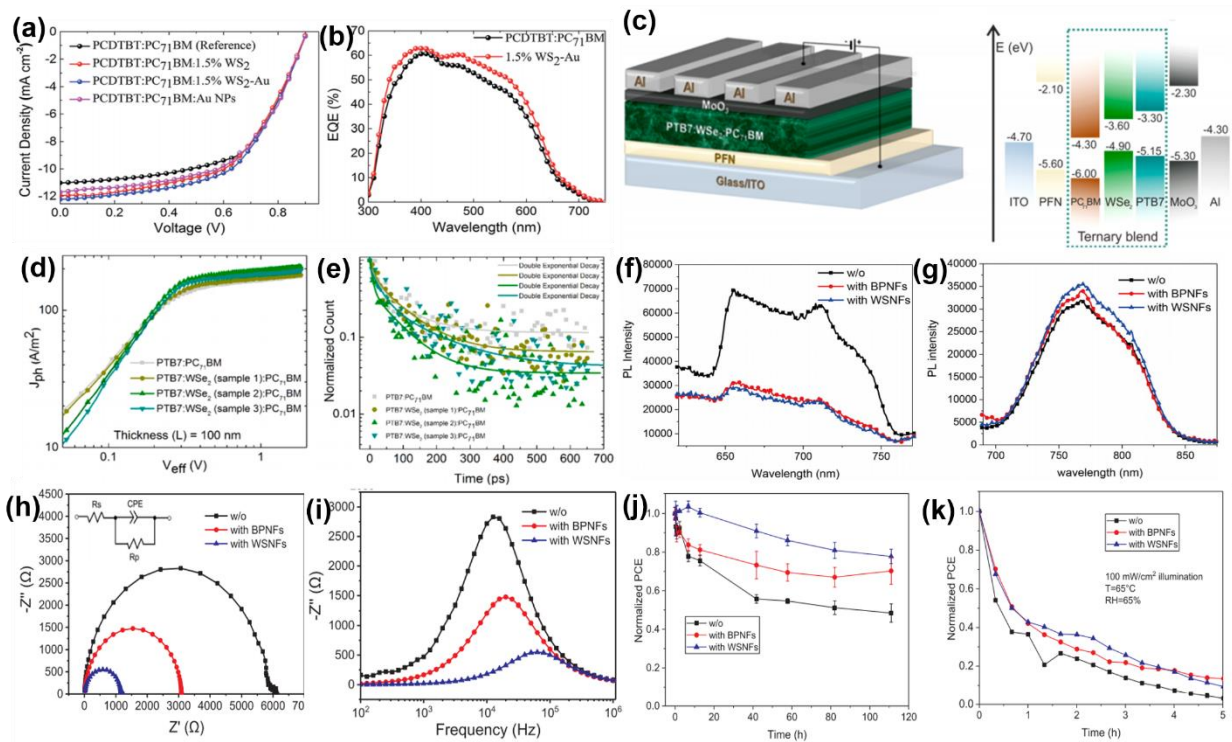
Fig. 7. (a) *J(V)* characteristics of the optimized devices incorporating the reference PCDTBT:PC$_{71}$BM, the PCDTBT:Au:PC$_{71}$BM, the PCDTBT:WS$_2$-Au:PC$_{71}$BM and the PCDTBT:WS$_2$-Au:PC$_{71}$BM blends, (b) IPCE spectra for the control devices and the one containing the WS$_2$-Au assemblies as a third component. Reproduced with permission [131]. Copyright 2016, Royal Society of Chemistry. (c) Schematic representation of the fabricated OPV with the addition of WSe$_2$ flakes in the BHJ with energy levels of the inverted devices under flat-band conditions, (d) photocurrent density (J$_{ph}$) versus effective voltage (V$_{eff}$) curves of the devices fabricated with and without different WSe$_2$ flakes in the active layer, (e) TRPL decay profiles of the reference and the different WSe$_2$ samples. Reproduced with permission [132]. Copyright 2017, American Chemical Society. (f) PL spectra of the acceptors - pure PC$_{71}$BM (black line), PC$_{71}$BM mixed with BPNFs (red line), PC$_{71}$BM mixed with WSNFs (blue line), (g) PL spectra of the donors - pure PTB7-Th (black line), PTB7-Th mixed with BPNFs (red line), PTB7-Th mixed with WSNFs (blue line), (h) Cole-Cole plots of devices under different conditions. Inset is an equivalent circuit employed for fitting different impedance curves, (i) frequency-dependent imaginary parts in the impedances spectra of the devices under different conditions; (j) normalized PCE of different devices as a function of storage time in the ambient, (k) Maximum Power Point (MPP) tracking of different devices under 100 mW/cm^2 irradiation. Reproduced with permission [133]. Copyright 2019, Elsevier.

3. Perovskite Solar Cells

3.1 Graphene-based perovskite solar cells

Recently, the incorporation of graphene and its derivatives in organic-inorganic hybrid perovskite materials has been utilized for the development of efficient PSC with improved photovoltaic performances and operational stability. The high conductivity and transparency of graphene make it possible to replace the traditional TCO or metal electrodes. Owing to its mechanical robustness, and being a very abundant material, graphene has become a center of attention in the development of flexible, highly efficient semitransparent PSC [136,137]. Furthermore, as graphene-based materials can be dispersed in water and other organic solvents, it has been widely used in solution-processed PSC. The graphene derivatives have been used in various forms and with different functionalities, either incorporated in mesoscopic or in planar device configuration [138,139]. The graphene derivatives such as GO or r-GO have been employed as HTL or dopants in the HTL to enhance the hole extraction in PSC [140], and several graphene-based materials have been used as charge transport and extraction layers, to enhance the photovoltaic performance while extending the long-term stability of PSC [139,141,142]. These materials can also be effective for reducing charge recombination pathways and decrease the leakage currents, with a similar role as in OPV [143-145]. The results presented in the literature on photovoltaic performance using different graphene and its derivatives in PSC are summarized in **Table 4**.

Table 4. Summary of performance results of graphene-based PSC

| Cell Configuration	V_{OC} (V)	J_{SC} (mA/cm^2)	FF (%)	PCE (%)	Ref.
FTO/TiO$_2$/MAPbI$_{3-x}$Cl$_x$/Spiro-OMeTAD/ PEDOT:PSS/Graphene	0.95	17.75	71.7	12.0	146
Graphene/MoO$_3$/PEDOT:PSS/MAPbI$_3$/C$_{60}$/BCP/LiF/Al	1.06	21.50	75.0	17.1	147
Graphene/MoO$_3$/PEDOT: PSS/MAPbI$_3$/C$_{60}$/BCP/LiF/Al	0.96	21.20	70.0	14.2	148
Graphene/MoO$_3$/PEDOT:PSS/MAPbI$_3$/C$_{60}$/BCP/LiF/Al	1.00	21.70	68.0	16.8	149
ITO/GO/MAPbI$_{3-x}$Cl$_x$/PCBM/ZnO/Au	1.00	17.46	71.0	12.4	150
ITO/r-GO/MAPbI$_3$/PC$_{61}$BM/BCP/Ag	0.95	14.81	71.1	10.8	151
ITO/GO/MAPbI$_{3-x}$Cl$_x$/BCP/LiF/Al	0.92	14.51	72.0	9.6	152
FTO/c-TiO$_2$/m-TiO$_2$/MAPbI$_3$/r-GO/Au	0.95	11.50	60.5	6.6	153
FTO/ Oxo-G$_1$/MAPbI$_3$/PC$_{61}$BM/ZnO/Al	1.08	18.06	78.0	15.2	154
ITO/TiO$_2$/MAPbI$_3$Cl$_{3-x}$/RGO-4FPH/spiro-OMeTAD/Au	1.11	21.5	78.6	18.7	155
ITO/PEDOT: PSS-GO:NH$_3$/MAPbI$_{3-x}$Cl$_x$/ PCBM/Bphen/Ag	1.03	22.06	71.0	16.1	156
ITO/GO/MAPbI$_3$:GO/PCBM/Ag	0.93	20.71	65.1	15.2	157
FTO/c-TiO$_2$/m-TiO$_2$/GO-Li/MAPbI$_3$/Spiro-OMeTAD/Au	0.86	19.61	70.3	11.8	158
FTO/c-TiO$_2$ /m-TiO$_2$:r-GO/MAPbI$_3$/Spiro-OMeTAD/Au	1.11	21.98	80.0	19.5	159
ITO/PEDOT:PSS/MAPbI$_3$/PCBM/EFGnPs-F/Al	0.98	18.50	78.0	14.3	160
ITO/PEDOT:PSS/MAPbI$_3$/graphene nanoribbon/Al	0.93	22.68	78.0	16.5	161
ITO/SnO$_2$:G/perovskite/spiro-OMeTAD/Au	1.09	23.06	72.0	18.1	162
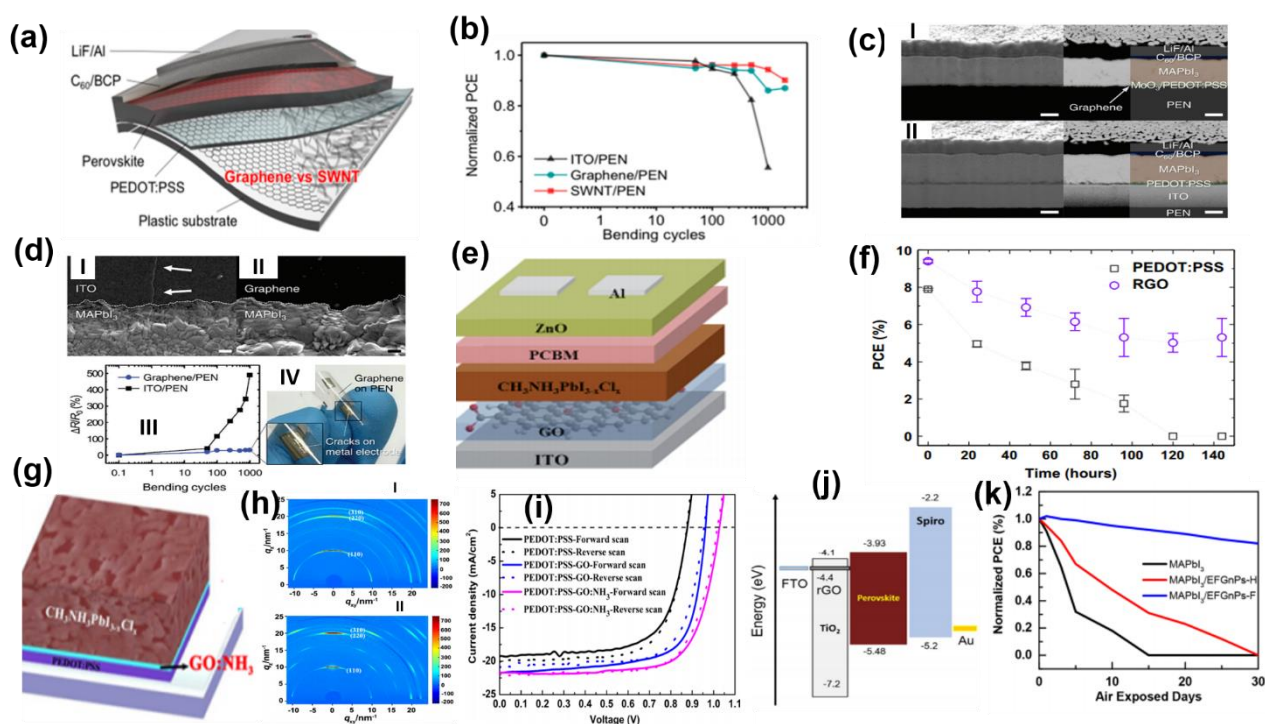
Fig. 8. (a) Schematic illustration of the flexible PSC using graphene and SWNT on a PEN substrate, (b) cyclic flexural test results for flexible PSC using ITO/PEN (black), graphene/PEN (green), and SWNT/PEN (red). Reproduced with permission [148]. Copyright 2017, American Chemical Society. (c) Cross-sectional images; focused ion-beam assisted SEM images of complete perovskite devices fabricated on (I) a Gr-Mo (MoO$_3$- decorated graphene) on PEN substrate (II) PEN/ITO, (d) SEM cross-section and degradation plot of MAPI PSC on (I) PEDOT:PSS/ITO/PEN and (II) PEDOT:PSS/Gr-Mo/PEN films, measured after 1000 bending cycles at R = 4 mm (scale bar, 200 nm). (III) Relative resistance change ($\Delta R/R_0$) of the Gr-Mo/PEN and ITO/PEN films as a function of bending cycles at R = 4 mm, and (IV) Photograph of a Gr-Mo/PEN substrate on which rectangular Al/Au/Cr electrodes were formed. When the substrate was bent twice at R = 4 mm, linear cracks were generated on the metal electrodes due to the weak adhesion between the graphene and the metal surfaces. Reproduced with permission [149]. Copyright 2017, Royal Society of Chemistry. (e) Schematic of a pin type PSC with GO as HTL. Reproduced with permission [150]. Copyright 2014, Royal Society of Chemistry. (f) variation in the photovoltaic parameters as a function of exposure time to ambient atmosphere for PEDOT:PSS and r-GO PSC. Reproduced with permission [151]. Copyright 2015, Elsevier. (g) Schematic of the pin configuration PSC with GO-NH$_3$ layer, (h) 2D-grazing incidence X-ray diffraction profile of perovskite films on two different substrates, (I) ITO/PEDOT:PSS and (II) ITO/ PEDOT:PSS-GO:NH$_3$, (i) forward and reverse *J(V)*characteristics of three perovskite solar cells under 100 mW/cm^2 AM 1.5G irradiation. Reproduced with permission [156]. Copyright 2016, American Chemical Society. (j) Energy level diagram of r-GO PSC. Reproduced with permission [159]. Copyright 2016, Wiley-VCH. (k) Stability of MAPbI$_3$ devices with EFGnPs-H and EFGnPs-F layers over 30 days. Reproduced with permission [160]. Copyright 2017, American Chemical Society.

You et al. reported for the first time in 2014 on laminated stacked CVD graphene as the top transparent electrode in semitransparent perovskite solar cells [146]. The graphene electrode maintained a good electrical contact with the HTL, i.e., the spiro-OMeTAD over the perovskite layer, showing a maximum PCE of 12.03 %. The CVD graphene is mechanically flexible and can be used as a transparent electrode for PSC, as needed for flexible perovskite solar cells fabricated by printing and R2R processing techniques. Sung et al. reported on graphene as a transparent conducting anode for PSC [147]. For comparative analysis, graphene and graphene with MoO_3 were used as the anode for inverted PSC, with device architecture consisting of graphene covered with MoO_3/PEDOT:PSS/MAPbI$_3$/C$_{60}$/BCP/LiF/Al. Using an optimized MoO_3 layer thickness of 2 nm, a PCE of 17.1 % was measured, while with ITO, the PCE was 18.8 %. The MoO_3 doped graphene improved the interface by forming a more desirable energy level alignment for the anode contact. Jeon et al. presented the widely-used single-walled carbon nanotube (SWNT) and graphene, as the bottom electrode in pin configuration PSC (**Fig. 8a**) [148]. The obtained PCE of the graphene-based PSC was 14.2 % on glass, and 13.3 % on PEN substrates, which is higher than that of the SWNT-based PSC with a PCE of 12.8 % for glass and 11.0 % for PEN. This is because graphene enabled a better surface morphology, as shown by AFM analysis, and a higher transparency, as evidenced by UV−vis spectroscopy. The SWNT-based flexible devices exhibited marginally higher mechanical stability than the graphene-based devices as analyzed with Raman spectroscopy and cyclic flexural testing (**Fig. 8b**). This was ascribed to the entangled nature of the nanotube network, and their inherent defect-free lattice, as compared to graphene. Yoon et al. reported on the utilization of graphene as a replacement for ITO on flexible PEN substrates in PSC [149]. Cross-sectional focused ion-beam assisted SEM (FIB-SEM) images of complete perovskite devices fabricated on PEN/graphene and PEN/ITO are shown in **Fig. 8c**. The photovoltaic performance using graphene reached a PCE of 16.8 %, without hysteresis, whereas for ITO electrodes the PCE was 17.3 %. The devices with graphene electrodes exhibited extremely good bending stabilities, maintaining 90 % of their original PCE after 1000 bending cycles, and 85 % after 5000 bending cycles, at a bending radius of 2 mm. For ITO electrodes, the PCE drops to less than 40 % of its initial value after 1000 bending cycles, and below 20 % after bending 5000 times (**Fig. 8d**). This superior robustness against mechanical deformation of the graphene-based perovskite solar cells further suggests application in foldable flexible devices.

Wu et al. reported in 2014 on the use of GO as an HTL for PSC in pin configuration as shown in **Fig. 8e** [150]. The PCE of the devices with GO as HTL was 12.4 %. The perovskite film on the GO layer formed highly textured perovskite crystal domains and preferential in-plane orientation of

the (110) plane, as confirmed by the GIXRD measurements. The homogenous large domains, crystal orientation and improved surface coverage of films with GO as HTL provided a good compatibility between the perovskite layer and interlayers, which is fruitful for the fabrication of efficient PSC. J.-S. Yeo reported a solution-processed method at room temperature to use reduced graphene oxide (r-GO) as an HTL for highly stable PSC [151]. The PSC with device architectures of glass/ITO/r-GO/$CH_3NH_3PbI_3$/PC_{61}BM/BCP/Ag obtained a PCE of 10.8 %, which was higher than the reference PEDOT:PSS and GO-based devices, with PCE of 9.14 and 4.04 %, respectively. As r-GO has a higher conductivity, improved energy level alignment, and enhances the crystallinity of the perovskite $CH_3NH_3PbI_3$ layer, PSC with r-GO exhibited a more effective charge collection with a reduced recombination. PSC with r-GO also showed an extended cell operation time compared to PSC employing the conventional PEDOT:PSS. In ambient stability testing, PSC with r-GO exhibited a promising device-stability retaining a PCE of about 6 % (62 % of the initial value) after 140 h of exposure to air, compared to PEDOT:PSS based PSC that drastically deteriorated and showed complete failure in photovoltaic characteristics after just 120 h of exposure, as illustrated in **Fig. 8f**. Kim et al. reported using GO, synthesized by the oxidation of natural graphite powder using Hummers' method, as HTL in PSC [152]. The obtained PCE for device configuration of ITO/GO/$MAPbI_{3-x}Cl_x$/BCP/LiF/Al was 9.62 % for GO-based PSC, in comparison to a PCE of 9.93 % obtained from the PEDOT:PSS based devices. Palma et al. used r-GO, prepared by an easy and efficient reduction method, as HTL for mesoscopic PSC [153]. The shelf-life stability of the PSC based on r-GO showed a PCE of 6.6 % after 1987 h, whereas for the devices based on Spiro-OMeTAD, the PCE dropped to approximately 6.5 %. During the light-soaking stability test, r-GO-based PSC have retained 26 % of the initial PCE, while spiro-OMeTAD dropped to almost 10 % of its initial PCE. Moreover, from the open circuit voltage decay measurements, it was confirmed that the r-GO also reduced the charge carrier recombination, in these PSC devices. Chen et al. reported introducing oxo-functionalized graphene (oxo-G_1) as a HTL in PSC with FTO/Oxo-G_1/$MAPbI_3$/PC_{61}BM/ZnO/Al configuration [154]. The solution-processed oxo-G_1 was employed to substitute the hydrophilic PEDOT:PSS, which resulted in a PCE of 15.2 %. Moreover, the environmental light-soaking stability of the unpackaged inverted architecture perovskite solar cells were significantly enhanced by oxo-G1. Oxo-G_1 not only acts as an efficient hole-extraction layer, but more importantly, in contrast to PEDOT:PSS, contributes to stabilizing PSC by suppressing moisture ingress due to its hydrophobic nature. This could be fruitful for moisture diffusion control and development of efficient environmentally stable PSC. Li et al. developed chemically modified

graphene oxides which provide surface passivation of perovskite layers, and act as efficient interlayer to reduce interfacial recombination and enhance hole extraction of the PSC [155]. The MAPbI$_3$Cl$_{3-x}$/rGO-4FPH based solar cells yielded a VOC of 1.11 V with PCE of 18.75 %. By combining the passivation effects of various functionalized organic groups and the hole transporting properties, the functionalized reduced graphene oxides significantly reduced the energy loss and increased the V$_{OC}$, along with providing high efficiency of PSC. Thus, such interlayers could well substitute the conventional single-function materials to realize high performance devices. Feng et al. reported the introduction of GO:NH$_3$ layer into PSC with a device structure of ITO/PEDOT:PSS-GO:NH$_3$/CH$_3$NH$_3$PbI$_{3-x}$Cl$_x$/PC$_{61}$BM/Bphen/Ag (**Fig. 8g**) [156]. Results from GIXRD (**Fig. 8h**), SEM, ultraviolet photoelectron spectroscopy (UPS), XPS, and UV−visible absorption measurements demonstrated that the perovskite films with GO:NH3 showed improved crystallization, improved morphology and a better energy-level-alignment at the perovskite interface, as compared to the reference devices. The PCE was measured to be more than 16 % for GO:NH$_3$ devices, whereas for PEDOT:PSS the PCE was 11.38 %, and for the PEDOT:PSS-GO layer it was 14.71 %, as illustrated by the *J(V)* characteristics in **Fig. 8i**. Moreover, the GO:NH$_3$ interfacial layer improved the stability of PSC in the ambient condition, which suggests that the chemically modified graphene oxide interfacial layer is effective for stable high-performance PSC. Chung et al. reported GO as an anode contact layer for pin structured PSC with device architecture of ITO/GO/perovskite:GO/PCBM/Ag [157]. The optimized GO used in the hybrid perovskite composite yielded a PCE of 15.2 %, which was much higher than that of a GO-based planar heterojunction devices (PCE of 12.3 %). The devices with GO mixed in the photoactive layer enhanced the charge generation, reduced the charge recombination and balanced the charge mobility, overall resulting in the best device performance. The possibility of using cost-effective solution-processing at low temperature for perovskite:GO, with GO used as HTL, enhanced the photovoltaic performance with a high reproducibility while maintaining good stability.

Agresti et al. presented lithium neutralized graphene oxide (GO-Li) as the ETL on top of the mesoporous TiO$_2$ layer of PSC [158]. The modified graphene exhibited a work function of -4.3 eV, aligning well with the conduction band of TiO$_2$, thus leading to a significant enhancement of the electron extraction from the perovskite to the TiO$_2$ layer. The PSC with GO-Li layer improved the photovoltaic performance to 11.8 %, with a higher J$_{sc}$, FF and lower hysteresis, whereas the reference devices without GO-Li layer showed a PCE of 10.3 %. Simultaneously, the GO-Li-based devices showed an improved stability under 1 Sun irradiation. Cho et al. reported on the effect of Li-treated

r-GO with mesoporous TiO_2 in hybrid PSC as illustrated in **Fig. 8j** [159]. The devices with r-GO showed a highly improved PCE of about 19.54 %, whereas the control reference devices obtained a PCE of 18.89 %. The devices made with r-GO with Li-treated m-TiO_2 had improved transportation and injection of photoexcited electrons, resulting in the improved overall performance of the PSC. Kim et al. presented edge-selective fluorine functionalized graphene nanoplatelets (EFGnPs-F) as an ETL in ITO/PEDOT:PSS/$MAPbI_3$/PCBM/EFGnPs-F/Al devices [160]. Although the PCE dropped slightly with the usage of EFGnPs-F to 14.3 %, compared to the reference with 14.7 %, it showed a superior stability, maintaining 82 % of initial PCE over 30 days without encapsulation in ambient humidity of ~50 % at room temperature, while the pristine perovskite devices were completely degraded after 30 days as depicted in **Fig. 8k**. Water contact angle measurements showed high water-repelling properties compared to pristine perovskite films, as the contact angle for $MAPbI_3$/PCBM/EFGnPs-F changed to 65.5º from the reference perovskite films value of 30.2º. This indicates that the F substitution on EFGnPs provides hydrophobic properties which slow down the chemical degradation. Castro et al. synthesized cove-edge graphene hPDI3-Pyr-hPDI3 nanoribbons and used them as ETL in inverted planar PSC with ITO/PEDOT:PSS/$MAPbI_3$/graphene nanoribbon/Al configuration [161]. Devices based on the graphene nanoribbons yielded PCE of 16.5 % with negligible hysteresis and superior long-term stability, while a maximum PCE of 14.9 % is achieved with counter reference device based on $PC_{61}BM$. Due to ease of control of the electronic structure and hydrophobicity of the graphene nanoribbons, this is an efficient ETL alternative to PCBM in PSC devices. Zhu et al. demonstrated solution-processed graphene ink doped SnO_2 nanoparticles as the ETL for planar-structured PSC with ITO/SnO_2:G/perovskite/spiro-OMeTAD/Au configuration [162]. The graphene-SnO_2 based PSC exhibited higher PCE of 18.11 % than the control SnO_2 devices which yielded 17.01 %, combined with superior ambient stability of the cells. It maintained of 90 % of the initial PCE after aging in ambient condition for 300 h. Therefore, the incorporation of the graphene in the SnO_2 matrix has been an effective strategy to simultaneously enhance the electron mobility and carrier extraction and suppress the interfacial charge recombination.

3.2 2D materials beyond graphene for perovskite solar cells

The outstanding characteristics of 2D materials, as described under the organic solar cell section, have also been very attractive for perovskite solar cells technology. 2D materials based on transitional

metal dichalcogenides, TMD, and black phosphorus, BP, exhibit very good potential as exciton blocking layers with tunable bandgap, in contrast to graphene 2D materials. The integration of 2D materials beyond graphene in PSC architectures (mesoscopic and planar) is depicted in **Fig. 9.**
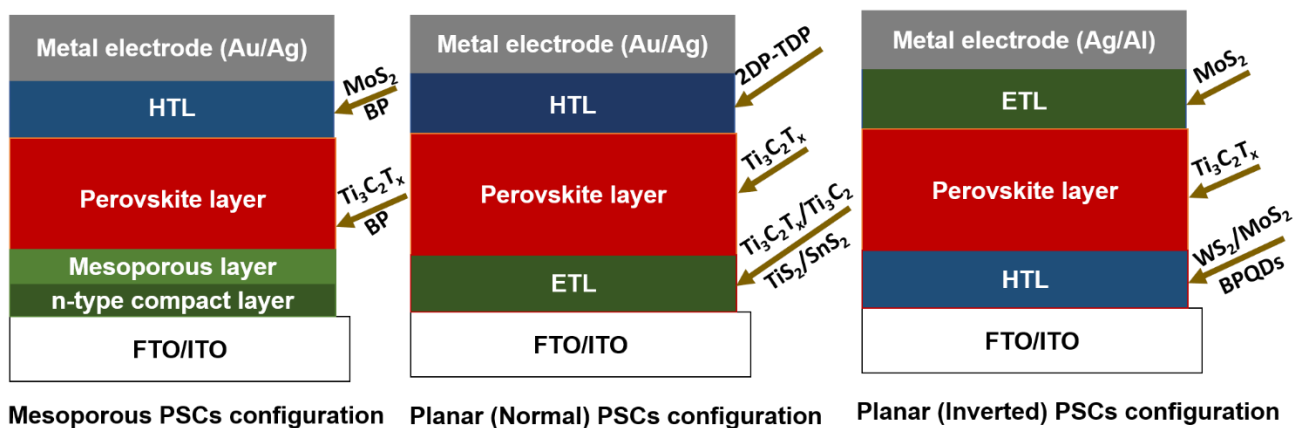

Fig. 9. Schematic representation of the different configurations of PSC with the incorporation of different 2D materials beyond graphene.

3.2.1 2D materials beyond graphene as HTL for perovskite solar cells

For PSC, the charge transport interlayers play an important role in the photovoltaic performance and long-term device stability. Materials with high hole mobilities, efficient electron and exciton blocking ability, good chemical stability, and alignment of valence band/HOMO levels with the perovskite valence band, are ideal HTL candidates for PSC. Due to the unique optoelectronic properties, such as high carrier mobilities, thickness-dependent band structure, ultra-thin thickness, smooth surface without dangling bonds, and high compatibility with printable and flexible electronics, 2D material based HTL can improve the photovoltaic performance and long-term stability of PSC. The photovoltaic performances of various 2D materials beyond graphene used as HTL are summarized in **Table 5**.

Table 5. Summary of the results of 2D materials HTL in PSC

| Cell Configuration	V_{OC} (V)	J_{SC} (mA/cm^2)	FF (%)	PCE (%)	Reference
ITO/WS$_2$/CH$_3$NH$_3$PbI$_{3-x}$Cl$_x$/PC$_{61}$BM/BCP/LiF/Al	0.82	15.91	64.0	8.0	152
ITO/MoS$_2$/CH$_3$NH$_3$PbI$_{3-x}$Cl$_x$/PC$_{61}$BM/BCP/LiF/Al	0.96	15.89	67.0	9.5	152
FTO/c-TiO$_2$/m-TiO$_2$/CH$_3$NH$_3$PbI$_3$/MoS$_2$/spiro-OMeTAD/Au	0.93	21.50	66.7	13.3	163
ITO/MoS$_2$/CH$_3$NH$_3$PbI$_3$/PC$_{61}$BM/Al	0.84	12.60	57.0	6.1	164
ITO/PEDOT:PSS+MoS$_2$-PAS/CH$_3$NH$_3$PbI$_3$/PC$_{61}$BM/Ag	0.998	24.03	62.5	16.5	165
ITO/MoS$_2$/CH$_3$NH$_3$PbI$_3$/C$_{60}$/BCP/Al	0.88	20.94	78.0	14.4	166
ITO/WS$_2$/CH$_3$NH$_3$PbI$_3$/C$_{60}$/BCP/Al	0.97	21.22	73.0	15.0	166
FTO/c-TiO$_2$/m-TiO$_2$/MAPbI$_3$/BP/spiro-OMeTAD/Au	1.06	20.22	76.1	16.4	167
ITO/PTAA/MoS$_2$/CH$_3$NH$_3$PbI$_3$/PC$_{61}$BM/PFN/Al	1.01	20.71	78.0	16.4	168
ITO/PTAA/antimonene/CH$_3$NH$_3$PbI$_3$/PCBM/Bphen/Al	1.11	23.42	76.8	20.1	169
ITO/MoS$_2$/CH$_3$NH$_3$PbI$_3$/TiO$_2$/Ag	0.93	26.25	84.0	20.5	170
FTO/c-TiO$_2$/SnO$_2$ QDs/ CsFAMA/MoS$_2$/PTAA/Au	1.05	22.02	79.9	18.5	171
FTO/c-TiO$_2$/SnO$_2$ QDs/CsFAMA/WS$_2$/PTAA/Au	1.05	23.59	76.6	19.0	172
ITO/PTAA/WS$_2$/CH$_3$NH$_3$PbI$_3$/PCBM/BCP/Ag	1.15	22.75	80.6	21.1	173
ITO/SnO$_2$/CH$_3$NH$_3$PbI$_3$/2DP-TDP/MoO$_3$/Ag	1.16	24.02	79.6	22.1	174
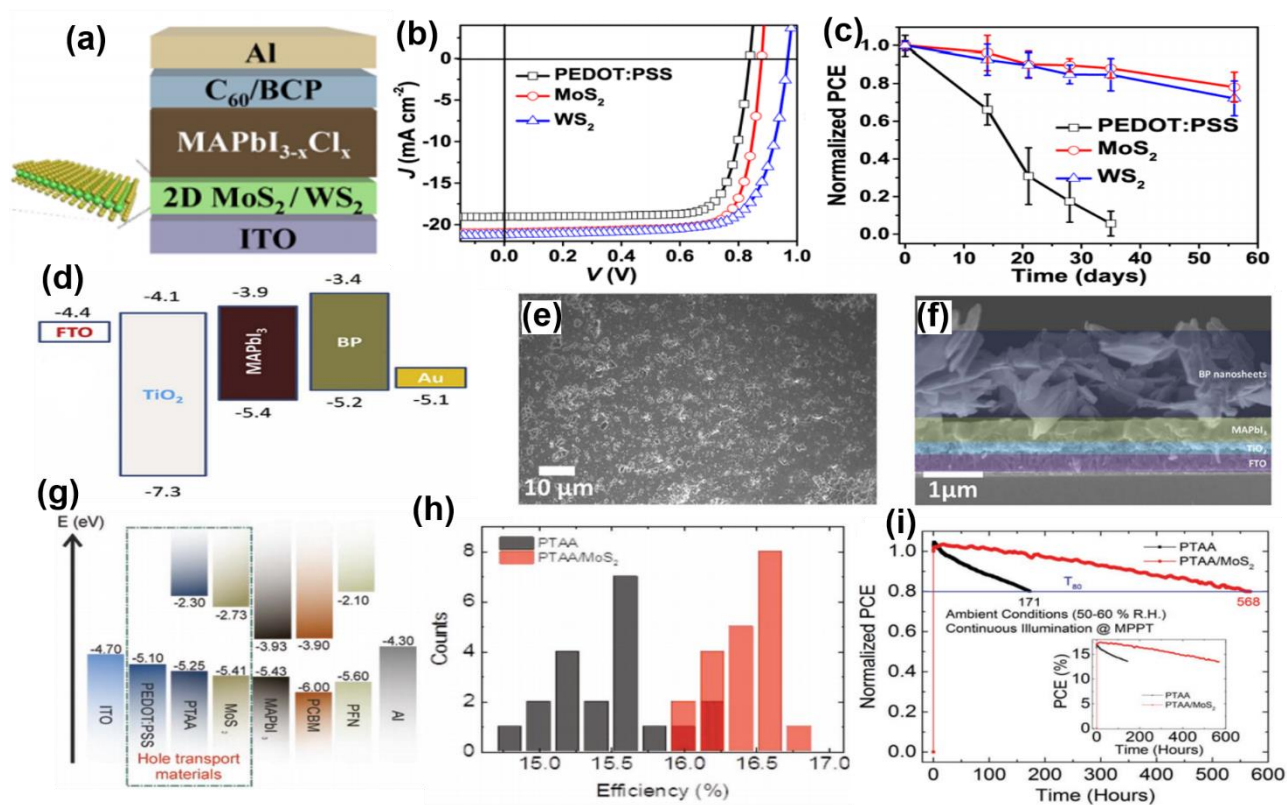
Fig. 10. (a) p-i-n device configuration of PSC, (b) *J(V)* curves of PSC with PEDOT:PSS, MoS$_2$, and WS$_2$ as HTL, and (c) shelf-life stability of PSC based on PEDOT:PSS, MoS$_2$, and WS$_2$, where 20 cells were measured for each HTL. Reproduced with permission [166]. Copyright 2017, American Chemical Society. (d) Band energy diagram of MAPI cells using BP nanosheets as HTL (e) FE-SEM image of BP nanosheets on MAPbI$_3$, and (f) cross-sectional FE-SEM image of the fabricated perovskite solar cells with BP nanosheets as HTL. Reproduced with permission [167]. Copyright 2017, Elsevier. (g) Energy-band diagram under flat-band conditions, (h) PCE distribution of the devices with (red) and without (black) MoS$_2$ interlayer extracted from 20 identical devices, (i) long-term stability of encapsulated PSC under continuous illumination at the MPP (maximum power point) tracking of devices with (red scatter) and without MoS$_2$ (black scatter). Reproduced with permission [168]. Copyright 2018, Wiley-VCH.

Kim et al. reported on the use of MoS_2 and WS_2 as HTL in mixed halide $CH_3NH_3 PbI_{3-x}Cl_x$ PSC [152]. The polycrystalline structure of these materials was synthesized by a chemical deposition method, and the HTL layers were then deposited using a uniformly spin-coated $(NH_4)MoS_4$ and $(NH_4)WS_4$ precursor solution. The roughness of all the samples was found low enough not to interrupt the perovskite layer above it. The measured work functions of MoS_2 and WS_2 were found to be -4.95 eV and -5.0 eV, respectively, showing proper alignment with the valence band of the perovskite layer. The PCE using MoS_2 and WS_2 as HTL was 9.53 % and 8.02 % respectively, while for PEDOT:PSS it was 9.93 %. Capasso et al. reported the use of MoS_2 flakes in FTO/c-TiO_2/m-TiO_2/$CH_3NH_3PbI_3$/MoS_2/spiro-OMeTAD/Au [163], incorporated between $MAPbI_3$ photoactive absorber and the Spiro-OMeTAD HTL, vastly used in a mesoscopic PSC. The flakes acted both as a protective layer by preventing the formation of shunt contacts between the perovskite and the Au electrode, and as a hole transport layer with a suitable energy level alignment between the photoactive layer and the gold anode. The PSC with MoS_2 exhibited a PCE of 13.3 % compared to reference devices without MoS_2. The improved stability ($\Delta\eta/\eta = -7$ % for MoS_2 vs. $\Delta\eta/\eta = -34$ % for the reference device) was mainly due to the surface passivation of the perovskite layer provided by the MoS_2, which prevents the iodine migration from the perovskite into the HTL. The authors have also fabricated larger area cells (1.05 cm^2), reaching a PCE of 11.5 %. Dasgupta et al. presented a method for forming uniform and homogeneous single or multilayer MoS_2 films, to be introduced as HTL in planar MAPI PSC [164]. These devices show a modest PCE of 6.01 %, which was higher than the HTL-free reference devices. These devices exhibited a significantly lower PCE compared to the previously reported works exploiting MoS_2 as the HTL, where doping of the MoS_2 through UV-ozone treatment resulted in a suitable energy band alignment between the valance band of the inorganic HTL and the valance band of $CH_3NH_3PbI_3$. Dai et al. reported on a method to functionalize MoS_2 with phenylacetylene silver (PAS), by dispersing it in solvents like DMF and water, and using it, blended together with PEDOT:PSS, as HTL in planar heterojunction PSC [165]. The PSC with MoS_2–PAS obtained a PCE of 16.47 %, whereas the reference devices with only PEDOT:PSS showed a PCE of 14.69 %. The stability of the devices was improved when MoS_2–PAS was used, showing a decrease in the performance by only 13 % (after 10 days), compared to a drop of around 52 % for the reference devices. Huang et al. studied two water-soluble 2D materials, i.e., MoS_2 and WS_2, employed as HTL in PSC, as represented in **Fig. 10a** [166]. The MoS_2 and WS_2 HTL based cells showed superior photovoltaic performance with PCE of 14.35 % and 15.00 %, respectively, whereas PEDOT:PSS showed a PCE of only 12.44 % (**Fig. 10b**). This significant enhancement of the PCE is

mainly due to the improved energy level alignment between the modified HTL and the valence band of the perovskite, which facilitates an efficient hole extraction. Moreover, the non-encapsulated solar cells containing MoS_2 and WS_2 as HTL exhibited a superior stability, as illustrated in **Fig. 10c.**

Muduli et al. reported in 2017 on liquid exfoliated layers of BP nanosheets as an HTL for PSC [167]. Using photoelectron spectroscopy, the valence band level of the BP nanosheets was measured to be -5.2 eV, which is suitable for hole extraction from $MAPbI_3$. The band alignment of perovskite solar cells with BP nanosheets as HTL is illustrated in **Fig. 10d**. The PSC device performance with BP nanosheets + Spiro-OMeTAD reached a PCE of 16.4 %, whereas spiro-OMeTAD alone reached 13.1 %, and BP nanosheets alon 7.88 %. The FE-SEM image of BP nanosheets on $MAPbI_3$ and cross-sectional FE-SEM image of the fabricated perovskite solar cells with BP nanosheets as HTM (**Fig. 10e and 10f**) illustrate the presence of a highly crystalline perovskite film over the BP nanosheets. Photoluminescence quenching and impedance measurements further support the significance of the role of BP in the hole extraction and transport towards the anode. Kakavelakis et al. introduced solution-processed MoS_2 flakes between the poly(triarylamine) (PTAA) HTM and the $MAPbI_3$ absorber in pin PSC [168]. **Fig. 10g** compares the energy levels of PEDOT:PSS with PTAA and MoS_2 vs. the absorber layer. The devices with MoS_2 show higher device efficiencies with (16.42 %), compared to 15.51 % from reference devices. The PCE distribution of the devices with and without the MoS_2 interlayer, extracted from 20 identical devices, is depicted in **Fig. 10h**, demonstrating the device reproducibility of the MoS_2- based HTM PSC. The stability of the devices with MoS_2 significantly improved for encapsulated devices tested under continuous light exposure. After 568 h of continuous operation, the PCE retained ~80 % of its initial PCE, as depicted in **Fig. 10i**. This improved stability was attributed to the interlayer shielding the perovskite from the contact to the doped PTAA. The superior mechanical strength of the MoS_2/PTAA compared to the bare doped PTAA, under electrical bias stressing, prohibits the water molecules to reach the photoactive layer through the ITO and HTL material. In addition, it blocks indium ion migration from ITO towards the interface between the HTL and the perovskite photoactive layer. A PSC with an 0.5 cm^2 active area using this MoS_2 interlayer approach demonstrated a PCE of 13.17 %. Zhang et al reported 2D antimonene nanosheets employed as HTL in planar inverted PSC with ITO/PTAA/antimonene/$CH_3NH_3PbI_3$/PCBM/Bphen/Al configuration [169]. 2D antimonene HTL ensures efficient hole transfer and fast hole extraction at the perovskite/hole transport layer interface, resulting with enhanced PCE of 20.05 % for the cells with 2D antimonene sheets, as compared to 17.60 % of control devices without antimonene sheets.

Kohnehpoushi et al. reported on the use of MoS_2 based HTL for the exploitation of low-cost planar nip type $MAPbI_3$ PSC with $ITO/MoS_2/CH_3NH_3PbI_3/TiO_2/Ag$ device configuration [170]. In this study, the impact of the HTL and the perovskite layer thicknesses was discussed and optimized to lower the recombination rates and enhance the light absorption in the cells. The optimum 1.34 nm thickness for MoS_2 and 350 nm of $MAPbI_3$ layer, yielded the best PCE of 20.53 %, whereas the PCE of the HTL-free PSC was only 10.41 %. Hemasiri et al. reported the use of the intercalated Li^+ based solution-processable 2D-MoS_2 flakes as an interfacial layer between the dopant-free poly(triarylamine) (PTAA) and perovskite layer of triple cation $\{Cs_{0.1}FAPbI3(0.81)MAPbBr_{3(0.09)}\}$ perovskite (CsFAMA) based n-i-p type PSC [171]. The cells with MoS_2 showed the PCE of 18.54 % along with superior lifetime as compared to the controlled device without MoS_2 (15.05 % PCE). The interfacial layer with HTL exhibited great role to improve the performance of the cells as ascribed to the efficient hole extraction with the stabilization of the perovskite/HTM interface, band alignment and mitigating the degradation in the photoactive layer. Furthermore, Hemasiri et al. mentioned Li^+ intercalated liquid-phase exfoliated 2D-WS_2 as an interfacial layer between the dopant-free PTAA and perovskite layer of triple cation (CsFAMA) based n-i-p type PSC [172]. The use of the WS_2 layer helped to enhance the PCE to 19.02 % from 15.7 % as reference device owing to the boosted V_{OC} and FF. And, the PSC with the 2D-WS_2 layer retained 80 % of their initial photocurrent for 100h when keeping the unencapsulated cells in continuous illumination under an ambient atmosphere, but the control reference PSC maintained 80 % of their initial photocurrent after only 8 h. The interfacial layer exhibited crucial role to minimize the energy barrier and charge accumulation at the interface and thus intensified the extraction of detrapped charges and charge transfer dynamics for stabilized efficiency of over 19 %. Cao et al. presented liquid-phase-exfoliated WS_2 flakes introduced as growth templates for van der Waals epitaxial growth of mixed perovskite films, leading to perovskite grains with enlarged sizes and a preferred orientation along (001). They have applied them in inverted PSC devices with $ITO/PTAA/WS_2/CH_3NH_3PbI_3/PCBM/BCP/Ag$ configuration [173], where perovskite films with high crystallinity and low defect density were obtained, and the WS_2 interlayer enhanced the charge extraction at the interface and suppressed interfacial charge recombination. The cells with WS_2 interlayer resulted in PCE of 21.1 % as compared to 18.5 % of control reference devices, along with excellent device stability. Fu et al. reported a solution-processable multifunctional 2D conjugated polymer, namely, 2DP-TDB, synthesized and applied as dopant-free HTM in the planar n-i-p PSC with $ITO/SnO_2/CH_3NH_3PbI_3/2DP-TDP/MoO_3/Ag$ configuration [174]. It is found that the 2D polymer with extended π-electron delocalization in two dimensions offers a deeper energy level

in comparison to spiro-OMeTAD, which could form a more matched energy level alignment with the VB of perovskite, leading to efficient charge transport and reduced energy loss. As a result, PSC containing 2DP-TDP as dopant-free HTL showed a superior PCE of 22.17 %. Importantly, the unencapsulated devices using dopant-free 2D conjugated HTL retained about 95 % of their initial efficiency upon storage in the ambient atmosphere for 1000 h, whereas the doped spiro-OMeTAD devices retained only 64 % of their original efficiency. The versatile 2DP-TDP characteristics, like dominant face-on packing orientation, good charge transport properties, efficient perovskite surface passivation capability and hydrophobicity play a vital role for both high efficiency and stability.

3.2.2 2D materials beyond graphene as ETL and as absorber additives in perovskite solar cells

Besides graphene and its derivatives, 2D materials have shown to be beneficial for use as ETL in perovskite devices. In contrast to 2D materials for HTL, materials with high electron mobilities, efficient hole blocking ability, good chemical stability, and proper LUMO levels that can match well with the perovskite conduction band, are sought after as ETL candidates. Moreover, 2D materials doping of the perovskite absorber could adjust the energy level alignment at the perovskite and related interfaces, and play a great role to reduce the trap-mediated recombination in perovskite cells. Again, 2D materials of TMD, MXene, black phosphorous and hexagonal boron nitrides are good material candidates for transport layers in PSC due to the possibility to adjust the aforementioned properties by doping and surface termination. The photovoltaic performance of various 2D materials beyond graphene used as ETL and as absorber additives in perovskite solar cells are summarized in **Table 6**.

Table 6. Summary of the results of 2D materials used as ETL and as absorber additives in PSC

| Cell Configuration	V_{OC} (V)	J_{SC} (mA/cm^2)	FF (%)	PCE (%)	Reference
FTO/TiS$_2$/MAPbI$_3$/Spiro-OMeTAD/Au	1.05	23.38	71.0	17.4	175
ITO/PEDOT:PSS/GO/MAPbI$_3$/PC$_{61}$BM/MoS$_2$/Ag	1.14	22.83	73.8	19.14	176
ITO/TiS$_2$/CH$_3$NH$_3$PbI$_3$/spiro-OMeTAD/Au	1.00	24.75	75.0	18.8	177
ITO/SnO$_2$-Ti$_3$C$_2$/CH$_3$NH$_3$PbI$_3$/Spiro-OMeTAD/Ag	1.06	23.14	75.0	18.3	178
ITO/Ti$_3$C$_2$T$_x$/CH$_3$NH$_3$PbI$_3$/Spiro-OMeTAD/Ag	1.08	22.63	70.0	17.2	179
ITO/SnS$_2$/CH$_3$NH$_3$PbI$_3$/spiro-OMeTAD/Au	1.16	23.55	73.0	20.12	180
ITO/Bi$_2$O$_2$Se/MAPbI$_3$/Spiro-OMeTAD/MoOx/Ag	0.99	16.16	57.0	9.12	181
ITO/SnO$_2$/Bi$_2$O$_2$Se/MAPbI$_3$/Spiro-OMeTAD/MoOx/Ag	1.07	23.48	75.85	19.06	181
FTO/cTiO$_2$/SnO$_2$/perovskite+BP/Spiro-OMeTAD/Ag	1.08	23.31	82.2	20.65	182
ITO/SnO$_2$/perovskite+MXene/ Spiro-OMeTAD/Ag	1.03	22.26	76.0	17.4	183
FTO/cTiO$_2$+MXene/mTiO$_2$+MXene/MXene/ perovskite+MXene/spiro-OMeTAD/Au	1.09	23.82	77.6	20.1	48
ITO/NiO/perovskite/PCBM+MXene/BCP/Ag	1.07	21.54	76.0	17.5	184
ITO/NiO/perovskite+MXene/PCBM+MXene/BCP/Ag	1.09	22.88	77.0	19.2	184
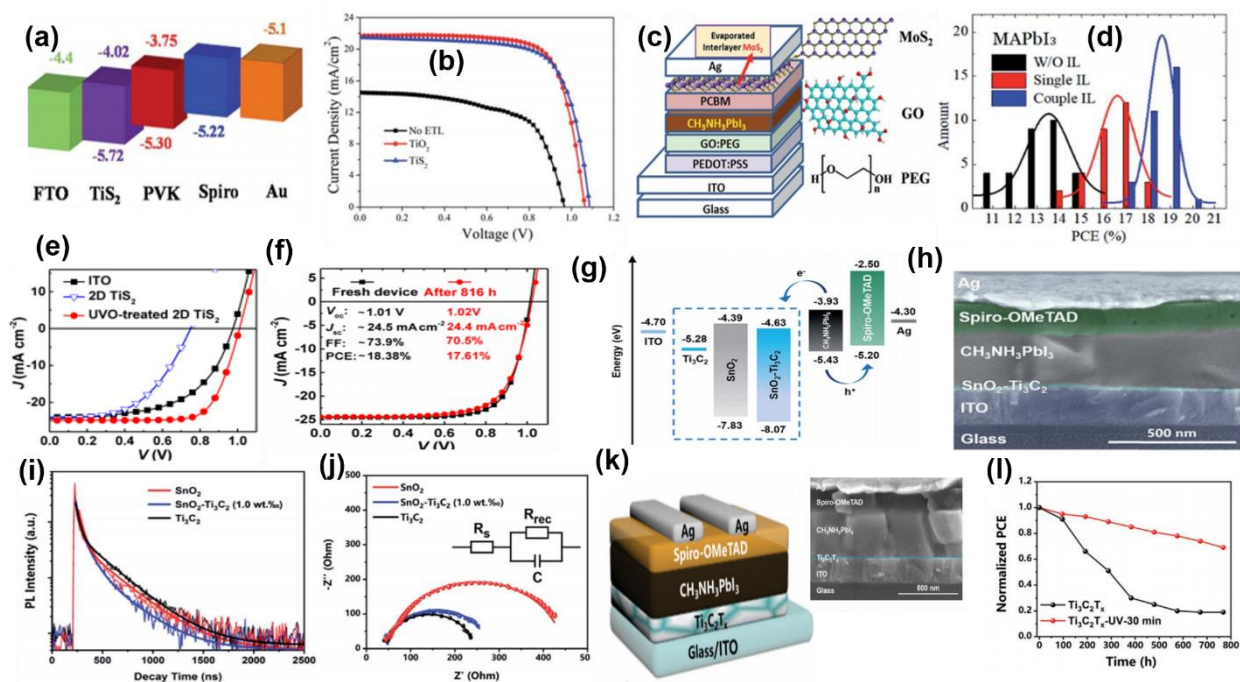
Fig. 11. (a) Energy level diagram, and (b) *J(V)* curves of the best-performing PSC with TiS_2 or TiO_2 as ETL, and without ETL. Reproduced with permission [175]. Copyright 2018, Royal Society of Chemistry. (c) Schematic diagram of the device structure and molecular structures of 2D interfacial materials, (d) statistics of the PCE distribution of MAPI devices with different IL (interface layers), each including an average of over 30 cells, in which single IL refers to only MoS_2, and coupled IL refers to both MoS_2 and GO. Reproduced with permission [176]. Copyright 2018, Royal Society of Chemistry. (e) Typical *J(V)*curves of the PSC with different ETL under the illumination, (f) *J(V)*curves of PSC with UVO-treated 2D TiS_2 as an ETL, taken from the first day and after 816 h storage at atmosphere conditions with an RH of ~10 % [177]. Reproduced with permission [177]. Copyright 2018, American Chemical Society. (g) Schematic energy level diagram of n-i-p type perovskite devices, (h) cross-sectional SEM image of the ITO/ETL/$CH_3NH_3PbI_3$/Spiro-OMeTAD/Ag PSC devices with SnO_2–Ti_3C_2 as the ETL, (i) transient photoluminescence spectra of MAPI perovskite utilizing different ETL, (j) Nyquist plots of the PSC with SnO_2, SnO_2–Ti_3C_2, or Ti_3C_2 [178]. Reproduced with permission [178]. Copyright 2019, Royal Society of Chemistry. (k) Device architecture of ITO/ETL/$CH_3NH_3PbI_3$/Spiro-OMeTAD/Ag, with $Ti_3C_2T_x$ as ETL, and cross-sectional SEM image of the PSC device, (l) stability of PSC using pristine $Ti_3C_2T_x$ and $Ti_3C_2T_x$, after 30 min of UV-ozone treatment of ETL, in ambient air (relative humidity ≈ 20 %) at 25 °C without encapsulation. Reproduced with permission [179]. Copyright 2019, Wiley-VCH.

Yin et al. reported on the 2D-TiS$_2$ prepared with a simple chemical exfoliation process, to replace TiO$_2$ as an ETL in planar PSC, as illustrated in **Fig. 11a**. [175]. The TiS$_2$ films prepared at low temperature by a solution coating process exhibited efficient electron transport and extraction ability comparable to that of TiO$_2$ films. The optimized devices with TiS$_2$, resulted in a PCE of 17.37 %, and improved stability compared to the devices employing conventional TiO$_2$ ETL. The respective *J(V)* curves of the best-performing PSC with TiS$_2$ or TiO$_2$ as ETL and without ETL are depicted in **Fig. 11b.** Wang et al. used MoS$_2$ as ETL and GO with PEDOT:PSS for electron blocking in pin type PSC (**Fig. 11c**) [176]. The perovskite material with GO and MoS$_2$ layers achieved a PCE of 19.14 % and *V$_{OC}$* of 1.135 V. Statistical PCE distribution for 30 cells based on MAPI perovskite with/without MoS$_2$ as the interfacial layer is shown in **Fig. 11d**. The J(V) curves show no hysteresis between forward and reverse sweep for the MoS$_2$ ETL. Huang et al. reported room-temperature aqueous solution-processed 2D TiS$_2$ prepared by exfoliation, and used it as ETL in planar nip type PSC with ITO/TiS$_2$/CH$_3$NH$_3$PbI$_3$/spiro-OMeTAD/Au layer stack [177]. The incorporation of the UVO- treated 2D TiS$_2$ ETL, yielded the PCE of 18.79 %. The UVO-treatment resulted in a very good energy alignment between the ETL and perovskite conduction band, resulting in the corresponding *J(V)* curves depicted in **Fig. 11e**). In addition, the nip type PSC with the UVO- treated 2D TiS$_2$ as an ETL showed an extremely high stability. Unencapsulated PSC exposed to atmosphere conditions with 10 % relative humidity (RH) maintained 95.8 % of their initial PCE after 816 h storage, as depicted in **Fig. 11f**, and when the RH was increased to 45−60 % the devices retained about 80 % of initial PCE upon100 h.

L. Yang et al. presented the use of Ti$_3$C$_2$ MXene as ETL in organic-inorganic lead halide PSC [178]. The schematic energy-level diagram of each layer with a cross-sectional SEM image of the PSC devices is illustrated in **Fig. 11g** and **11h.** An optimization of the fraction of Ti$_3$C$_2$ MXene nanocomposites mixed in the SnO$_2$ (0, 0.5, 1.0, 2.0, and 2.5 wt %) was conducted. At 1.0 wt %, the optimized PCE was reached, with a PCE of 18.34 %, whereas the pristine SnO$_2$ and pristine Ti$_3$C$_2$ MXene achieved PCE of 17.23 % and 5.28 %, respectively. Steady-state and transient PL spectra (**Fig. 11i**), SCLC (space-charge limited current) and electrochemical impedance spectroscopy (EIS) (**Fig. 11j**) show that the devices with SnO$_2$–Ti$_3$C$_2$ layer exhibit excellent electron extraction, electron mobility and low interfacial charge transfer resistance, provided by good charge transfer paths. Further, L. Yang et al. fabricated planar MAPI PSC in a nip configuration using Spiro-OMeTAD as HTL and Ti$_3$C$_2$T$_x$ MXene nanosheets as ETL (**Fig. 11k**) [179]. UV-ozone treatments were applied for tuning the optoelectronic properties of MXene, where the 30 min treatment yielded the peak

performance with a PCE of 17.17 %. Since the UV-ozone treatment generates additional oxide-like Ti-O bonds, it improved the interface properties between the $Ti_3C_2T_x$ and the perovskite layer, which led to an enhancement of the photovoltaic parameters. Moreover, UV-ozone treatment of $Ti_3C_2T_x$ also contributed to a better device stability, keeping over 70 % of the initial PCE after 800 h of storage, whereas pristine Ti_3C_2Tx -based PSC dropped to 30 % of their initial PCE within 384 h, as illustrated in **Fig. 11l**. Zhao et al. reported a 2D SnS_2 ETL for highly efficient planar PSC with $ITO/SnS_2/CH_3NH_3PbI_3/spiro$-OMeTAD/Au configuration [180]. A PCE of 20.12 % was achieved with the 2D ETL based PSC, along with an impressive V_{OC} of 1.161 V, while the reference device with SnO_2 yielded PCE of 17.72 % and V_{OC} of 1.09 V. The Pb···S interaction facilitates the formation of so-called microcosmic mosaic structure at the interface between the perovskite crystals and SnS_2, which enables a balanced electron/hole extraction at interfaces between ETL/perovskite and perovskite/HTL with suppressing interfacial charge recombination. Chen et al. synthesized 2D Bi_2O_2Se nanoflakes with a high charge mobility by facile composited molten salt growth method, and employed it as ETL in PSC with $ITO/SnO_2/Bi_2O_2Se/MAPbI_3/Spiro$-OMeTAD/MoOx/Ag configuration [181]. The PSC employing single 2D Bi_2O_2Se nanoflakes as ETL yielded a PCE of 9.12 %, which is 110 % higher than those without ETL (4.32 %). To fill the pinholes, defects on the surface and to effectively reduce recombination at the hetero-interface, new hybrid ETL SnO_2/Bi_2O_2Se was employed. The PSC employing SnO_2/Bi_2O_2Se hybrid ETL exhibited a higher average PCE of 19.06 %, which is 17 % improvement compared to devices based on single SnO_2 ETL (16.29 %). Further, the stability of PSC is enhanced with the application of hybrid ETL. The 2D Bi_2O_2Se could improve crystallization of perovskite thin film as well as facilitate charge transfer and reduce carrier recombination.
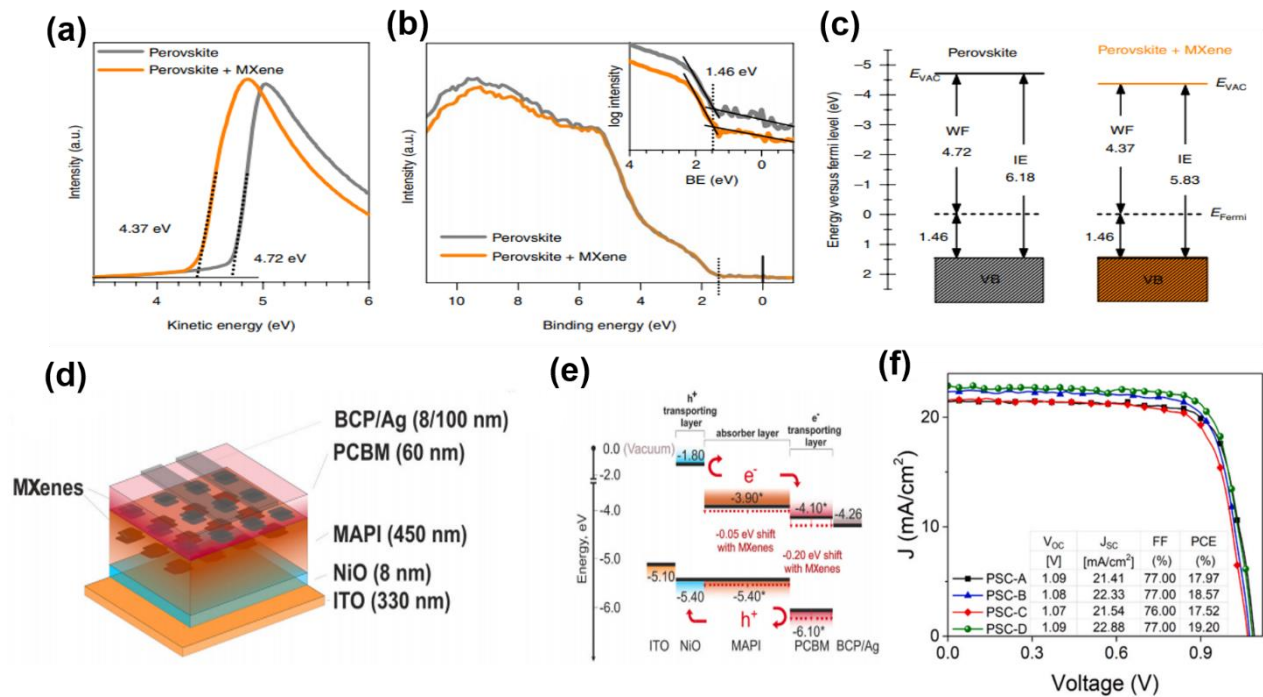
Fig. 12. (a) UPS spectra around the secondary electron cut-off, (b) UPS spectra in the valence band (VB) region. For the pristine perovskite, the valence band maximum, determined by the intercept with zero of the intensity plotted on a logarithmic scale (see inset in b) is at 1.46 eV below the Fermi level (E_{Fermi}), (c) energy scheme as measured by UPS, of pristine and MXene-doped perovskite with respect to the E_{Fermi}, where, IE is the ionization energy, E_{VAC} is the vacuum level, and BE is the binding energy. Reproduced with permission [48]. Copyright 2019, Springer Nature. (d) Schematic representation of MXene-based pin type PSC, (e) related energy band diagram of the different functional layers relative to vacuum. The band alignments are not to scale and show only the relative position, (f) *J(V)* curves of the best-efficient device for each of the tested device structures, acquired at 1 sun irradiation. The inset table shows the V_{OC}, J_{SC}, FF and PCE values extracted by the respective *J(V)* curves in which the layer stack of PSC-A is ITO/NiO/perovskite/PCBM/BCP/Ag, of PSC-B is ITO/NiO/perovskite+MXene/PCBM/BCP/Ag, of PSC-C is ITO/NiO/perovskite/PCBM+MXene/BCP/Ag, and of PSC-D is ITO/NiO/perovskite+MXene/PCBM+MXene/BCP/Ag. Reproduced with permission [184]. Copyright 2021, Elsevier.

Wang et al. reported incorporating BP into perovskite layer of the device with FTO/cTiO$_2$/SnO$_2$/perovskite+BP/Spiro-OMeTAD/Ag configuration [182]. The cells with BP improved the photovoltaic performance to 20.65 % PCE. In addition, their photostability was significantly enhanced - cells with BP retained about 94 % of initial PCE after 1000 h of continuous exposure to white light LED illumination in a dry N$_2$ glovebox, while their counterparts without BP decreased to 30 % of the initial PCE value. Addition of BP in perovskite material can simultaneously inhibit Pb$_0$ defect formation and elongate the picosecond charge recombination process, thereby providing not only a higher photovoltaic performance but also reducing the photo-induced damage or decomposition resulting in a significantly enhanced photostability under continuous illumination. Guo et al. reported on introducing a 2D-layered Ti$_3$C$_2$T$_x$ MXene into the perovskite precursor of the solar cells in the configuration ITO/SnO$_2$/perovskite+MXene/Spiro-MeOTAD/Ag [183]. The optimized 0.03 wt % of MXene additive used in the perovskite absorber layer enhanced the PCE to 17.41 % from the reference PCE of 15.54 %. It is proposed that the basic fluorine on the surface of Ti3C2Tx can enable protonation with hydrogen atoms of the CH3NH3 (MA), thus forming the interaction between fluorine and MA. The OH groups are hypothesized to form O-H···I$^-$ van der Waals interaction with MAI. Due to the interaction between the additive and MAI, during the antisolvent dripping, the nucleus generates around the additive and the number of the nucleus is suppressed, implying retardation in the nucleation process. By studying nucleation and growth route, using UV-vis spectroscopy and SEM, it could be shown that MXene retards the crystallization rate and increases the crystal size of the perovskite layer. Furthermore, the high electrical conductivity and mobility of MXene can accelerate the carrier transport behavior of the perovskite film. Moreover, Agresti et al. reported on introducing MXene in both the perovskite absorber and the TiO$_2$ ETL, providing tailored interface engineering at the perovskite/ETL interface for the FTO/cTiO$_2$+ MXene/mTiO$_2$+ MXene/MXene/perovskite + MXene/spiro-OMeTAD/Au devices [48]. The MXene work function tunability was shown to be very beneficial for the perovskite absorber and transporting layers in PSC. Moreover, the spectroscopy measurements and density functional theory calculations revealed that the addition of Ti$_3$C$_2$T$_x$ to the halide perovskite and TiO$_2$ layers permits tuning of the materials' work function without affecting other electronic properties. The combined MXene-doped layers and MXene-engineered interfaces exhibited a highly improved cell efficiency (more than 26 %) with respect to the reference cells, achieving a final maximum efficiency of 20.14 %, and an almost complete suppression of the cell hysteresis. The influence of the MXene additives on the work functions and valence band spectrum of the perovskite layers was measured by

UPS and shown in **Fig. 12a-c**. The low work function of MXene could be exploited to finely align the energy levels between the perovskite absorber layer and the cathode transport layer. The strong potential of MXene in work function tuning of perovskite absorbers and ETL, without affecting other properties of those materials, could inspire innovative designs of PSC and other perovskite-based devices. Saranin et al. demonstrated the potential role of MXene doping for both perovskite absorber and electron transport layers in ITO/NiO/perovskite+MXene/PCBM+MXene/BCP/Ag devices, as shown in **Fig. 12d** [184]. The proper alignment of the MXene conduction band with the perovskite conduction band and ETL LUMO level, combined with the passivation of trap states, resulted in an improved charge carrier extraction. **Fig. 12e** depicts the relative energy band diagram with Mxene included in the perovskite absorber and cathode transporting layer. These cells exhibited superior performance with a PCE of 19.20 %, in comparison to reference devices with 17.97 % for ITO/NiO/perovskite/PCBM/BCP/Ag, 18.57 % for ITO/NiO/perovskite+MXene/PCBM/BCP/Ag and 17.52 % for ITO/NiO/perovskite/PCBM+MXene/BCP/Ag, with respective *J(V)* curves shown in **Fig. 12f**. The incorporation of MXene in both perovskite absorber and ETL exhibited the vital role of interface band alignment optimization for improved charge extraction and charge transport properties. Thus, incorporation of 2D MXene into PSC has shown promising results for both the initial device performance, and importantly also for the device stability, although more studies at relevant light soaking levels would be an interesting outlook.

4. Summary and future outlook

In this review, we have described the recent progress made with the implementation of 2D materials such as graphene, graphene derivatives and 2D materials beyond graphene, i.e., transitional metal dichalcogenides, transitional metal carbides and/or nitrides and black phosphorus, as interlayers in the fabrication of organic (OPV) and perovskite (PSC) solar cells. Due to their unique properties such as high charge carrier mobility, high conductivity and high optical transparency, they show a great potential to be incorporated in optoelectronic applications replacing conventional materials. The abundance of their building block elements, compatibility with solution-processing techniques, and tunable work functions for energy level alignment with both organic and organic-inorganic perovskite photoactive materials, have revealed an avenue for the development of high performance organic and perovskite solar cells based on 2D materials. The 2D materials have been successfully applied as electrodes, hole (HTL) and electron (ETL) transport layers and the third component in bulk

heterojunction (BHJ) for OPV and PSC active layers, using which one can exhibit a higher absorption coefficient in the visible and near-infrared part of the solar spectrum, and more efficient charge carrier extraction, resulting in enhanced photovoltaic performance.

Among these 2D materials, graphene exhibits outstanding mechanical stability, and its convenient preparation finds use when employed as a transparent conducting electrode instead of existing transparent conductive oxides such as FTO and ITO. This is very useful for flexible OPV and PSC developed by printing or R2R processing techniques, which is considered as the avenue for future production. TMD such as MoS_2, WS_2, WSe_2, NbS_2, Bi_2Se_3, TaS_2, TiS_2, besides MXene and BP, have similar structural features, but versatile chemical and electronic properties, for which they have been incorporated as charge carrier extraction layers in organic and perovskite solar cells. 2D materials used in solar cells play a crucial role in facilitating the charge extraction with minimum recombination to improve the PCE, but also in increasing the long-term stability of easily processible organic and perovskite solar cells. However, scalable production of 2D materials could be challenging for fabricating large-area, high-performance solar cells, and there should still be found a way around their susceptibility to degradation in air. Therefore, for the fabrication of highly stable and efficient 2D material-based solar cells, the focus for the future should be on the development of air-stable and uniform 2D materials on large scale. The improved stability can be explored by different approaches e.g., via interface passivation effects and blocking of ion migration, but also by synthesis modifications and optimization of the device architecture. Much research attention should be focused on the interaction of 2D materials with organic and perovskite semiconductor materials, and their synergistic effects on the optoelectronic properties of the interfaces and devices. This requires many detailed interface studies and further stability studies, to gain a more in-depth understanding of the degradation effects at the new interfaces formed with the insertion of the 2D materials in these devices. As 2D materials exhibit a high mechanical flexibility, high environmental stability, low electrical resistivity, and low environmental impact, they can support the development of lightweight, eco-friendly and cost-effective high-performance flexible solar cells in the future.

Corresponding Author

* Corresponding author: madsen@mci.sdu.dk

References:

[1] C. Li, M. Liu, N. G. Pschirer, M. Baumgarten, K. Mullen, Polyphenylene-based materials for organic photovoltaics, Chem. Rev. 110 (2010) 6817-6855.

[2] G. Li, R. Zhu, Y. Yang, Polymer solar cells, Nat. Photonics 6 (2012) 153-161.

[3] M. Green, A. Ho-Baillie, H. Snaith, The emergence of perovskite solar cells, Nature Photon 8 (2014) 506-514.

[4] S. Dai, X. Zhan, Nonfullerene acceptors for semitransparent organic solar cells, Adv. Energy Mater. 8 (2018) 1800002.

[5] S. Li, L. Ye, W. Zhao, H. Yan, B. Yang, D. Liu, W. Li, H. Ade, J. Hou, A wide band gap polymer with a deep highest occupied molecular orbital level enables 14.2 % efficiency in polymer solar cells, J. Am. Chem. Soc. 140 (2018) 7159-7167.

[6] K. Dou, X. Wang, Z. Du, H. Jiang, F. Li, M. Sun, R. Yang, Synergistic effect of side-chain and backbone engineering in thieno[2,3-f]benzofuran-based conjugated polymers for high performance nonfullerene organic solar cells, J. Mater. Chem. A 7 (2019) 958-964.

[7] G. Wang, F. S. Melkonyan, A. Facchetti, T. J. Marks, All-polymer solar cells: recent progress, challenges, and prospects, Angew. Chem. Int. Ed. 58 (2019) 4129-4142.

[8] C. Gai, J. Wang, Y. Wang, J. Li, The low-dimensional three-dimensional tin halide perovskite: film characterization and device performance, Energies 13 (2020) 2.

[9] X. Dai, K. Xu, F. Wei, Recent progress in perovskite solar cells: the perovskite layer, Beilstein J. Nanotechnol. 11 (2020) 51-60.

[10] D. D. C. Rasi, R. A. J. Janssen, Advances in solution-processed multijunction organic solar cells, Adv. Mater. 31 (2019) 1806499.

[11] A. Urbina, The balance between efficiency, stability, and environmental impacts in perovskite solar cells: a review, J. Phys.: Energy 2 (2020) 022001.

[12]   Y. Cui, H. Yao, J. Zhang, T. Zhang, Y. Wang, L. Hong, K. Xian, B. Xu, S. Zhang, J. Peng, Z. Wei, F. Gao, J. Hou, Over 16 % efficiency organic photovoltaic cells enabled by a chlorinated acceptor with increased open-circuit voltages, Nat. Commun. 10 (2019) 2515.

[13]   Y. Cui, H. Yao, J. Zhang, K. Xian, T. Zhang, L. Hong, Y. Wang, Y. Xu, K. Ma, C. An, C. He, Z. Wei, F. Gao, J. Hou, Single-junction organic photovoltaic cells with approaching 18 % efficiency, Adv. Mater. 32 (2020) 1908205.

[14]   Q. Liu, Y. Jiang, K. Jin, J. Qin, J. Xu, W. Li, J. Xiong, J. Liu, Z. Xiao, K. Sun, S. Yang, X. Zhang, L. Ding, 18 % Efficiency organic solar cells, Science Bulletin, 65 (2020) 272-275.

[15]   Y. Cui, Y. Xu, H. Yao, P. Bi, L. Hong, J. Zhang, Y. Zu, T. Zhang, J. Qin, J. Ren, Z. Chen, C. He, X. Hao, Z. Wei, J. Hou, Single-junction organic photovoltaic cell with 19 % efficiency, Adv. Mater. (2021) 2102420.

[16]   J. J. Yoo, G. Seo, M. R. Chua, M.R. *et al.*, Efficient perovskite solar cells via improved carrier management, *Nature* 590 (2021) 587–593.

[17]   N. J. Jeon, H. Na, E. H. Jung, T.-Y. Yang, Y. G. Lee, G. Kim, H.-W. Shin, S. I. Seok, J. Lee, J. Seo, A fluorene-terminated hole-transporting material for highly efficient and stable perovskite solar cells, Nat. Energy 3 (2018) 682.

[18]   S. Jiang, P.-X. Hou, M.-L. Chen, B.-W. Wang, D.-M. Sun, D.-M. Tang, Q. Jin, Q.-X. Guo, D.-D. Zhang, J.-H. Du, K.-P. Tai, J. Tan, E. I. Kauppinen, C. Liu, H.-M. Cheng, Ultra-high performance transparent conductive films of carbon-welded isolated single-wall carbon nanotubes, Sci. Adv. 4 (2018) 9264.

[19]   I.-J. Park, T. I. Kim, T. Yoon, S. Kang, H. Cho, N. S. Cho, J.-I. Lee, T.-S. Kim, S.-Y. Choi, Flexible and transparent graphene electrode architecture with selective defect decoration for organic light-emitting diodes, Adv. Funct. Mater. 28 (2018) 1704435.

[20]   T. Mochizuki, Y. Takigami, T. Kondo, H. Okuzaki, Fabrication of flexible transparent electrodes using PEDOT:PSS and application to resistive touch screen panels, J. Appl. Polym. Sci. 135 (2018) 45972.

[21]   Y.-Z. Zhang, Y. Wang, Q. Jiang, J. K. El-Demellawi, H. Kim, H. N. Alshareef, MXene printing and patterned coating for device applications, Adv. Mater. 32 (2020) 1908486.

[22]   J. H. Seo, I. Hwang, H. D. Um, S. Lee, K. Lee, J. Park, H. Shin, T. H. Kwon, S. J. Kang, K. Seo, Cold isostatic-pressed silver nanowire electrodes for flexible organic solar cells via room temperature processes, Adv. Mater. 29 (2017) 1701479.

[23]   D. Angmo, F. C. Krebs, Flexible ITO-free polymer solar cells, J. Appl. Polym. Sci. 129 (2013) 1-14.

[24]   H. Park, J. A. Rowehl, K. K Kim, V. Bulovic, J. Kong, Doped graphene electrodes for organic solar cells, Nanotechnology 21 (2010) 505204.

[25]   H. Wang, Y. Wu, X. Yuan, G. Zeng, J. Zhou, X. Wang, J. W. Chew, Clay-inspired MXene-based electrochemical devices and photo-electrocatalyst: state-of-the-art progresses and challenges, Adv. Mater. 30 (2018) 1704561.

[26]   M. Naguib, V. N. Mochalin, M. W. Barsoum, Y. Gogotsi, 25th anniversary article: MXene: a new family of two-dimensional materials, Adv. Mater. 26 (2014) 992-1005.

[27]   A. K. Geim, Graphene: status and prospects, Science 324 (2009) 1530-1534.

[28]   Q. H. Wang, K. Kalantar-Zadeh, A. Kis, J. N. Coleman, M. S. Strano, Electronics and optoelectronics of two-dimensional transition metal dichalcogenides, Nat. Nanotechnol. 7 (2012) 699-712.

[29]   H. Kim, H. H. Kim, J. I. Jang, S. K. Lee, G.-W. Lee, J. T. Han, K. Cho, Doping graphene with an atomically thin two-dimensional molecular layer, Adv. Mater. 26 (2014) 8141.

[30]   S. V. Morozov, K. S. Novoselov, M. I. Katsnelson, F. Schedin, D. C. Elias, J. A. Jaszczak, A. K. Geim, Giant intrinsic carrier mobilities in graphene and its bilayer, Phys. Rev. Lett. 100 (1) (2008) 016602.

[31]   Y.-J. Yu, Y. Zhao, S. Ryu, L. E. Brus, K. S. Kim, P. Kim, Tuning the graphene work function by electric field effect, Nano Lett. 9 (2009) 3430.

[32]   Y. Shi, K. K. Kim, A. Reina, M. Hofmann, L.-J. Li, J. Kong, Work function engineering of graphene electrode *via* chemical doping, ACS Nano 4 (2010) 2689-2694.

[33]   B. Radisavljevic, A. Radenovic, J. Brivio, V. Giacometti, A. Kis, Single-layer MoS_2 transistors, Nature Nanotech. 6 (2011) 147-150.

[34]   W.S. Hummers, R. E. Offeman, Preparation of graphitic oxide, J. Am. Chem. Soc. 80 (1958) 1339.

[35]   K.P. Loh, Q. Bao, G. Eda, M. Chhowalla, Graphene oxide as a chemically tunable platform for optical applications, Nat. Chem. 2 (12) (2010) 1015-1024.

[36]   G. Eda, C. Mattevi, H. Yamaguchi, H. Kim, M. Chhowalla, Insulator to semimetal transition in graphene oxide, J. Phys. Chem. C 113 (35) (2009) 15768-15771.

[37]   D. Jariwala, V. K. Sangwan , L. J. Lauhon, T. J. Marks, M. C. Hersam, Emerging device applications for semiconducting two-dimensional transition metal dichalcogenides, ACS Nano 8 (2) (2014) 1102-1120.

[38]   Y. Yi, C. Wu, H. Liu, J. Zeng, H. He, J. Wang, A study of lateral Schottky contacts in WSe_2 and MoS_2 field effect transistors using scanning photocurrent microscopy, Nanoscale 7 (2015) 15711-15718.

[39]   K. F. Mak, C. Lee, J. Hone, J. Shan, T. F. Heinz, Atomically thin MoS_2: a new direct-gap semiconductor, Phys. Rev. Lett. 105 (2010) 136805.

[40]   A. Splendiani, L. Sun, Y. Zhang, T. Li, J. Kim, C.-Y. Chim, G. Galli, F. Wang, Emerging photoluminescence in monolayer MoS_2. Nano Lett. 10 (2010) 1271-1275.

[41]   M. Naguib, M. Kurtoglu, V. Presser, J. Lu, J. Niu, M. Heon, L. Hultman, Y. Gogotsi, M. W. Barsoum, Two-dimensional nanocrystals produced by exfoliation of Ti_3AlC_2, Adv. Mater. 23 (2011) 4248-4253.

[42]   M. Hong Ng, H. Huang, K. Zhou, P. S. Lee, W. Que, J. Z. Xu, L. B. Kong, Recent progress in layered transition metal carbides and/or nitrides (MXene) and their composites: synthesis and applications, J. Mater. Chem. A 5 (2017) 3039-3068.

[43]   M. R. Lukatskaya, O. Mashtalir, C. E. Ren, Y. D. Agnese, P. Rozier, P. L. Taberna, M. Naguib, P. Simon, M. W. Barsoum, Y. Gogotsi, Cation intercalation and high volumetric capacitance of two-dimensional titanium carbide, Science 341 (2013) 1502-1506.

[44]   M. Naguib, V. N. Mochalin, M. W. Barsoum, Y. Gogotsi, MXene: a new family of two- dimensional materials, Adv. Mater. 26 (2014) 992-1005.

[45]   M. Khazaei, A. Ranibar, M. Arai, T. Sasaki, S. Yunoki, S. Electronic properties and application of MXene: a theoretical review, J. Mater. Chem. C. 5 (2017) 2488-2503.

[46]   M. Khazaei, M. Arai, T. Sasaki, A. Ranjbar, Y. Liang, S. Yunoki, OH-terminated two-dimensional transition metal carbides and nitrides as ultralow work function materials, Phys. Rev. B 92 (2015) 1-10.

[47]   T. Hu, Z. Li, M. Hu, J. Wang, Q. Hu, Q. Li, X. Wang, Chemical origin of termination-functionalized MXene: $Ti_3C_2T_2$ as a case study, J. Phys. Chem. C 121 (2017) 19254-19261.

[48]   A. Agresti, A. Pazniak, S. Pescetelli, A. Di Vito, D. Rossi, A. Pecchia, M. Auf der Maur, A. Liedl, R. Larciprete, D. V. Kuznetsov, D. Saranin, A. Di Carlo, Titanium-carbide MXene for work function and interface engineering in perovskite solar cells, Nat. Mater. 18 (2019) 1228-1234.

[49]   J. Qiao, X. Kong, Z.-X. Hu, F. Yang, W. Ji, High-mobility transport anisotropy and linear dichroism in few-layer black phosphorus, Nature Commun. 5 (2014) 4475.

[50]   M. Engel, M. Steiner, P. Avouris, Black phosphorus photodetector for multispectral, high-resolution imaging, Nano Lett. 14 (2014) 6414-6417.

[51]   F. Xia, H. Wang, Y. Jia, Rediscovering black phosphorus as an anisotropic layered material for optoelectronics and electronics, Nat. Commun. 5 (2014) 4458.

[52]   H. Liu, Y. Du, Y. Deng, P. D. Ye, Semiconducting black phosphorus: synthesis, transport properties and electronic applications, Chem. Soc. Rev. 44 (9) (2015) 2732-2743.

[53]   C. R. Dean, A. F. Young, I. Meric, C. Lee, L. Wang, S. Sorgenfrei, K. Watanabe, T. Taniguchi, P. Kim, K. L. Shepard, J. Hone, Boron nitride substrates for high-quality graphene electronics, Nat. Nanotechnol. 5 (10) (2010) 722-726.

[54]   K. Watanabe, T. Taniguchi, H. Kanda, Direct-bandgap properties and evidence for ultraviolet lasing of hexagonal boron nitride single crystal, Nat. Mater. 3 (6) (2004) 404-409.

[55]   A. Castellanos-Gomez, Why all the fuss about 2D semiconductors? Nat. Photonics 10 (2016) 202-204.

[56]   X. Li, M. Sun, C. Shan, Q. Chen, X. Wei, Mechanical properties of 2D materials studied by in situ Microscopy techniques, Adv. Mater. Interfaces 5 (2018) 1701246.

[57]   X. Yu, K. Sivula, Toward large-area solar energy conversion with semiconducting 2D transition metal dichalcogenides, ACS Energy Lett. 1 (2016) 315-322.

[58]   J. Y. Lee, J.-H. Shin, G.-H. Lee, C.-H. Lee, Two-dimensional semiconductor optoelectronics based on van der Waals heterostructures, Nanomaterials 6 (2016) 193.

[59]   F. Bonaccorso, Z. Sun, T. Hasan, A. Ferrari, Graphene photonics and optoelectronics, Nat. Photonics 4 (2010) 611-622.

[60]   Y.-Y. Choi, K.-H. Choi, H. Lee, H. Lee, J.-W. Kang, H.-K. Kim, Nano-sized Ag-inserted amorphous $ZnSnO_3$ multilayer electrodes for cost-efficient inverted organic solar cells, Sol. Energy Mater. Sol. Cells, 95 (2011) 1615-1623.

[61]   J.-H. Park, K.-J. Ahn, S.-I. Na, H.-K. Kim, Effects of deposition temperature on characteristics of Ga-doped ZnO film prepared by highly efficient cylindrical rotating magnetron sputtering for organic solar cells, Sol. Energy Mater. Sol. Cells 95 (2011) 657-663.

[62]   H. Park, S. Chang, X. Zhou, J. Kong, T. Palacios, S. Gradečak, Flexible graphene electrode-based organic photovoltaics with record-high efficiency, Nano Lett. 14 (2014) 5148-5154.

[63]   B. H. Lee, J. H. Lee, Y. H. Kahng, N. Kim, Y. J. Kim, J. Lee, T. Lee, K. Lee, Graphene-conducting polymer hybrid transparent electrodes for efficient organic optoelectronic devices, Adv. Funct. Mater. 24 (2014) 1847-1856.

[64]   H. Park, P. R. Brown, V. Bulović, J. Kong, Graphene as transparent conducting electrodes in organic photovoltaics: studies in graphene morphology, hole transporting layers, and counter electrodes, Nano Lett. 12 (2011) 133-140.

[65]   R. Garg, S. Elmas, T. Nann, M. R. Andersson, Deposition methods of graphene as electrode material for organic solar cells, Adv. Energy Mater. 7 (2017) 1601393.

[66]   Y. H. Kim, C. Sachse, M. L. Machala, C. May, L. Müller-Meskamp, K. Leo, Highly conductive PEDOT:PSS electrode with optimized solvent and thermal post-treatment for ITO-free organic solar cells, Adv. Funct. Mater. 21 (2011) 1076-1081.

[67]   E. Destouesse, M. Top, J. Lamminaho, H.-G. Rubahn, J. Fahlteich, M. Madsen, Slot-die processing and encapsulation of non-fullerene based ITO-free organic solar cells and modules, Flexible and Printed Electronics, 4 (2019) 045004.

[68]   M. Ahmadpour, A. L. F. Cauduro, C. Methivier, B. Kunert, C. Labanti, R. Resel, V. Turkovic, H.-G. Rubahn, N. Witkowski, A. K. Schmid, M. Madsen, Crystalline molybdenum oxide layers as efficient and stable hole contacts in organic photovoltaic devices, ACS Appl. Energy Mater. 2 (2019) 420-427.

[69]   S. Olthof, T. Riedl, Chapter 3: Metal-oxide interface materials for organic and perovskite solar cell, World Sci. Ref. Hybrid Mater. 2 (2019) 61-104.

[70]   S. Bae, J. U. Lee, H.-S. Park, E.H. Jung, J.W. Jung, W. H. Jo, Enhanced performance of polymer solar cells with PSSA-g-PANI/graphene oxide composite as hole transport layer, Sol. Energy Mater. Sol. Cells 130 (2014) 599-604.

[71]   E. Stratakis, K. Savva, D. Konios, C. Petridis, E. Kymakis, Improving the efficiency of organic photovoltaics by tuning the work function of graphene oxide hole transporting layers, Nanoscale 6 (2014) 6925-6931.

[72]   M. Li, W. Ni, B. Kan, X. Wan, L. Zhang, Q. Zhang, G. Long, Y. Zuo, Y. Chen, Graphene quantum dots as the hole transport layer material for high-performance organic solar cells, Phys. Chem. Chem. Phys. 15 (2013) 18973–18978.

[73]   S.-S. Li, K.-H. Tu, C.-C. Lin, C.-W. Chen, M. Chhowalla, Solution-processable graphene oxide as an efficient hole transport layer in polymer solar cells, ACS nano 4 (2010) 3169-3174.

[74]   M. Mirsafaei, P. B. Jensen, M. Ahmadpour, H. Lakhotiya, J. L. Hansen, B. Julsgaard, H.-G. Rubahn, R. Lazzari, N. Witkowski, P. Balling, M. Madsen, Sputter-deposited titanium oxide layers as efficient electron selective contacts in organic photovoltaic devices, ACS Appl. Energy Mater. 3 (2020) 253-259.

[75]   Z. Lin, C. Jiang, C. Zhu, J. Zhang, Development of inverted organic solar cells with TiO_2 interface layer by using low-temperature atomic layer deposition, ACS Appl. Mater. Interfaces 5 (2013) 713-718.

[76]   S. Shao, K. Zheng, T. Pullerits, F. Zhang, Enhanced performance of inverted polymer solar cells by using poly(ethylene oxide)-modified ZnO as an electron transport layer. ACS Appl. Mater. Interfaces 5 (2013) 380-385.

[77]   U. K. Aryal, V. M. Arivunithi, S. S. Reddy, J. Kim, Y.-S. Gal, S.-H. Jin, Efficient dual cathode interfacial layer for high performance organic and perovskite solar cells, Organic Electronics 63 (2018) 222-230.

[78]   Z. Liang, Q. Zhang, L. Jiang, G. Cao, ZnO cathode buffer layers for inverted polymer solar cells, Energy Environ. Sci. 8 (2015) 3442-3476.

[79]   N. Chakravarthi, U. K. Aryal, K. Gunasekar, H.-Y. Park, Y.-S. Gal, Y.-R. Cho, S. I. Yoo, M. Song, S.-H. Jin, Triazine-based polyelectrolyte as an efficient cathode interfacial material for polymer solar cells, ACS Appl. Mater. Interfaces 9 (2017) 24753-24762.

[80]   H. You, J. Zhang, Z. Zhang, C. Zhang, Z. Lin, J. Chang, G. Han, J. Zhang, G. Lu, Y. Hao, Low temperature aqueous solution-processed ZnO and polyethylenimine ethoxylated cathode buffer bilayer for high performance flexible inverted organic solar cells. Energies 10 (2017) 494.

[81]   Y. Wang, X. Chen, Y. Zhong, F. Zhu, K. P. Loh, Large area, continuous, few-layered graphene as anodes in organic photovoltaic devices, Appl. Phys. Lett. 95 (2009) 209.

[82]   H. Park, R. M. Howden, M. C. Barr, V. Bulovic, K. Gleason, J. Kong, Organic solar cells with graphene electrodes and vapor printed poly(3,4-ethylenedioxythiophene) as the hole transporting layers, ACS Nano 6 (2012) 6370-6377.

[83]   C.-L. Hsu, C.-T. Lin, J.-H. Huang, C.-W. Chu, K.-H. Wei, L.-J. Li, Layer-by-layer graphene/TCNQ stacked films as conducting anodes for organic solar cells, ACS Nano 6 (2012) 5031-5039.

[84]   H. Kim, S.-H. Bae, T.-H. Han, K.-G. Lim, J.-H. Ahn, T.-W. Lee, Organic solar cells using CVD-grown graphene electrodes, Nanotechnology 25 (2014) 014012.

[85]   H. Park, S. Chang, X. Zhou, J. Kong, Ts Palacios, S. Gradečak, Flexible graphene electrode-based organic photovoltaics with record-high efficiency, Nano Lett. 14 (2014) 5148-5154.

[86]   B. H. Lee, J.H. Lee, Y.H. Kahng, N. Kim, Y.J. Kim, J. Lee, T. Lee, K. Lee, Graphene-conducting polymer hybrid transparent electrodes for efficient organic optoelectronic devices, Adv. Funct. Mater. 24 (2014) 1847-1856.

[87]   Y. Song, S. Chang, S. Gradecak, J. Kong, Visibly-transparent organic solar cells on flexible substrates with all-graphene electrodes, Adv. Energy Mater. 6 (2016) 1600847.

[88]   A. G. Ricciardulli, S. Yang, X. Feng, P. W. Blom, Solution-processable high-quality graphene for organic solar cells, ACS Appl. Mater. Interfaces 9 (2017) 25412-25417.

[89]   I. P. Murray, S. J. Lou, L. J. Cote, S. Loser, C. J. Kadleck, T. Xu, J. M. Szarko, B. S. Rolczynski, J. E. Johns, J. Huang, Graphene oxide interlayers for robust, high-efficiency organic photovoltaics, J. Phys. Chem. Lett. 2 (2011) 3006-3012.

[90]   J. M. Yun, J. S. Yeo, J. Kim, H. G. Jeong, D. Y. Kim, Y. J. Noh, S. S. Kim, B. C. Ku, S. I. Na, Solution-processable reduced graphene oxide as a novel alternative to PEDOT:PSS hole transport layers for highly efficient and stable polymer solar cells, Adv. Mater. 23 (2011) 4923.

[91]   J.-S. Yeo, J.-M. Yun, Y.-S. Jung, D.-Y. Kim, Y.-J. Noh, S.-S. Kim, S.-I. Na, Sulfonic acid-functionalized, reduced graphene oxide as an advanced interfacial material leading to donor polymer-independent high-performance polymer solar cells, J. Mater. Chem. A 2 (2014) 292-298.

[92]   X. Cheng, J. Long, R. Wu, L. Huang, L. Tan, L. Chen, Y. Chen, Fluorinated reduced graphene oxide as an efficient hole-transport layer for efficient and stable polymer solar cells, ACS Omega 2 (2017) 2010-2016.

[93]   D. Konios, G. Kakavelakis, C. Petridis, K. Savva, E. Stratakis, E. Kymakis, Highly efficient organic photovoltaic devices utilizing work-function tuned graphene oxide derivatives as the anode and cathode charge extraction layers, J. Mater. Chem. A 4 (2016) 1612-1623.

[94]   S. Qu, M. Li, L. Xie, X. Huang, J. Yang, N. Wang, S. Yang, Noncovalent functionalization of graphene attaching [6,6]-phenyl-c61-butyric acid methyl, ACS Nano 7 (2013) 4070-4081.

[95]   D. H. Wang, J. K. Kim, J. H. Seo, I. Park, B. H. Hong, J. H. Park, A. J. Heeger, Transferable graphene oxide by stamping nanotechnology: electron-transport layer for efficient bulk-heterojunction solar cells, Angew. Chem. Int. Ed. 52 (2013) 2874-880.

[96]   F. Pan, C. Sun, Y. Li, D. Tang, Y. Zou, X. Li, S. Bai, X. Wei, M. Lv, X. Chen, Y. Li, Solution-processable n-doped graphene-containing cathode interfacial materials for high-performance organic solar cells, Energy Environ. Sci. 12 (2019) 3400-3411.

[97]   K. D. G. I. Jayawardena, R. Rhodes, K. K. Gandhi, M. R. R. Prabhath, G. D. M. R. Dabera, M. J. Beliatis, L. J. Rozanski, S. J. Henley, S. R. P. Silva, Solution processed reduced graphene oxide/metal oxide hybrid electron transport layers for highly efficient polymer solar cells, J. Mater. Chem. A 1 (2013) 9922-9927.

[98]   D. Zheng, W. Huang, P. Fan, Y. Zheng, J. Huang, J. Yu, Preparation of reduced graphene oxide:ZnO hybrid cathode interlayer using in situ thermal reduction/annealing for interconnecting nanostructure and its effect on organic solar cell, ACS Appl. Mater. Interfaces 9 (2017) 4898-4907.

[99]   G. Kakavelakis, D. Konios, E. Stratakis, E. Kymakis, Enhancement of the efficiency and stability of organic photovoltaic devices via the addition of a lithium-neutralized graphene oxide electron-transporting layer, Chem. Mater. 26 (2014) 5988-5993.

[100]   M. D. Jong, L. V. Ijzendoorn, M. D. Voigt, Stability of the interface between indium-tin-oxide and poly(3,4-ethylenedioxythiophene)/poly(styrenesulfonate) in polymer light-emitting diodes, Appl. Phys. Lett. 77 (2000) 2255.

[101]   E. Voroshazi, B. Verreet, A. Buri, R. Muller, D. D. Nuzzo, P. Heremans, Influence of cathode oxidation via the hole extraction layer in polymer:fullerene solar cells, Org. Electron. 12 (2011) 736-744.

[102]   V. Shrotriya, G. Li, Y. Yao. C. W. Chu, Y. Yang, Transition metal oxides as the buffer layer for polymer photovoltaic cells, Appl. Phys. Lett. 88 (2006) 073508.

[103]   J. R. Manders, S.-W. Tsang, M. J. Hartel, T.-H. Lai, S. Chen, C. M. Amb, J. R. Reynolds, F. So, Solution-processed nickel oxide hole transport layers in high efficiency polymer photovoltaic cells, Adv. Funct. Mater. 23 (2013) 2993-3001.

[104]   X. Yu, T. J. Marks, A. Facchetti, Metal oxides for optoelectronic applications, Nat. Mater. 15 (2016) 383-396.

[105]   J.-M. Yun, Y.-J. Noh, J.-S. Yeo, Y.-J. Go, S.-I. Na, H.-G. Jeong, J. Kim, S. Lee, S.-S. Kim, H.Y. Koo, T.-W. Kim, D.-Y. Kim, Efficient work-function engineering of solution-processed MoS_2 thin-films for novel hole and electron transport layers leading to high-performance polymer solar cells, J. Mater. Chem. C 1 (2013) 3777.

[106]   X. Gu, W. Cui, H. Li, Z. Wu, Z. Zeng, S.-T. Lee, H. Zhang, B. Sun, A solution processed hole extraction layer made from ultrathin MoS_2 nanosheets for efficient organic solar cells, Adv. Energy Mater. 3 (2013) 1262-1268.

[107]   X. Gu, W. Cui, T. Song, C. Liu, X. Shi, S. Wang, B. Sun, Solution-processed 2D niobium diselenide nanosheets as efficient hole-transport layers in organic solar cells, ChemSusChem 7 (2014) 416-420.

[108]   Q. V. Le, T. P. Nguyen, H. W. Jang, S. Y. Kim, The use of UV/ozone-treated MoS_2 nanosheets for extended air stability in organic photovoltaic cells, Phys. Chem. Chem. Phys. 16 (2014) 13123-13128.

[109]   Q. V. Le, T. P. Nguyen, K. S. Choi, Y.-H. Cho, Y. J. Hong, S. Y. Kim, Dual use of tantalum disulfides as hole and electron extraction layers in organic photovoltaic cells, Phys. Chem. Chem. Phys. 2014, 16, 25468-25472.

[110]   J. M. Yun, Y. J. Noh, C. H. Lee, S. I. Na, S. Lee, S. M. Jo, H. I. Joh, D.Y. Kim, Exfoliated and partially oxidized MoS_2 nanosheets by one-pot reaction for efficient and stable organic solar cells, Small 10 (2014) 2319-2324.

[111]   X. Yang, W. Fu, W. Liu, J. Hong, Y. Cai, C. Jin, M. Xu, H. Wang, D. Yang and H. Chen, Engineering crystalline structures of two dimensional MoS_2 sheets for high-performance organic solar cells, J. Mater. Chem. A, 2 (2014) 7727-7733.

[112]   X. Yang, W. Liu, M. Xiong, Y. Zhang, T. Liang, J. Yang, M. Xu, J. Ye, H. Chen, Au nanoparticles on ultrathin MoS_2 sheets for plasmonic organic solar cells, J. Mater. Chem. A 2 (2014) 14798-14806.

[113]   Q. V. Le, T. P. Nguyen, S. Y. Kim, UV/ozone-treated WS_2 hole-extraction layer in organic photovoltaic cells, Phys. Status Solidi RRL 8 (5) (2014) 390-394.

[114]   Z. Yuan, Z. Wu, S. Bai, W. Cui, J. Liu, T. Song, B. Sun, Layered bismuth selenide utilized as hole transporting layer for highly stable organic photovoltaics, Org. Electron. 26 (2015) 327-333.

[115]   Z. Wang, M. Zhao, Y. Zhou, B. Zhao, Y. Miao, P. Liu, Y. Hao, H. Wang, B. Xu, Y. Wu, S. Yin, Novel 2D material from AMQS-based defect engineering for efficient and stable organic solar cells, 2D Mater. 6 (2019) 045017.

[116]   Y. Lin, B. Adilbekova, Y. Firdaus, E. Yengel, H. Faber, M. Sajjad, X. Zheng, E. Yarali, A. Seitkhan, O. M. Bakr, A. El-Labban, U. Schwingenschlögl, V. Tung, I. McCulloch, F. Laquai,

and T. D. Anthopoulos, 17 % Efficient organic solar cells based on liquid exfoliated WS_2 as a replacement for PEDOT:PSS, Adv. Mater. 31 (2019) 1902965.

[117]   Z. Yu, W. Feng, W. Lu, B. Li, H. Yao, K. Zeng, J. Ouyang, MXene with tunable work functions and their application as electron- and hole-transport materials in non-fullerene organic solar cells, J. Mater. Chem. A 7 (2019) 11160-11169.

[118]   C. Hou, H. Yu, C. Huang, Solution-processable $Ti_3C_2T_x$ nanosheets as an efficient hole transport layer for high-performance and stable polymer solar cells, J. Mater. Chem. C 7 (2019) 11549-11558.

[119]   C. Hou, H. Yu, Modifying the nanostructures of PEDOT:PSS/$Ti_3C_2T_x$ composite hole transport layers for highly efficient polymer solar cells, J. Mater. Chem. C 8 (2020) 8, 4169-4180.

[120]   Y. Liu, Q. Tao, Y. Jin, X. Liu, H. Sun, A. El Ghazaly, S. Fabiano, Z. Li, J. Luo, J. Rosen, F. Zhang, $Mo_{1.33}C$ MXene-assisted PEDOT:PSS hole transport layer for high performance bulk-heterojunction polymer solar cells, ACS Appl. Electron. Mater. 2 (2020) 163-169.

[121]   J. Wang, H. Yu, C. Hou, J. Zhang, Solution-processable PEDOT:PSS:α-In2Se3 with enhanced conductivity as a hole transport layer for high-performance polymer solar cells, ACS Appl. Mater. Interfaces 12 (2020) 26543-26554.

[122]   M. A. Ibrahem, T.-W. Lan, J. K. Huang, Y.-Y. Chen, K.-H. Wei, L.-J. Li, C. W. Chu, High quantity and quality few-layers transition metal disulfide nanosheets from wet-milling exfoliation, RSC Adv. 3 (2013) 13193-13202.

[123]   K. S. Lee, Y. J. Park, J. Shim, C. H. Lee, G. H. Lim, H. Y. Kim, J. W. Choi, C. L. Lee, Y. Jin, K. Yu, H. S. Chung, B. Angadi, S. I. Nah, D. I. Son, Effective charge separation of inverted polymer solar cells using versatile MoS2 nanosheets as an electron transport layer, J. Mater. Chem. A 7 (2019) 15356-15363.

[124]   S. Lin, S. Liu, Z. Yang, Y. Li, T.W. Ng, Z. Xu, Q. Bao, J. Hao, C.-S. Lee, C. Surya, F. Yan, S. P. Lau, Solution-processable ultrathin black phosphorus as an effective electron transport layer in organic photovoltaics, Adv. Funct. Mater. 26 (2016) 864–871.

[125]   S. Foster, F. Deledalle, A. Mitani, T. Kimura, K.- B. Kim, T. Okachi, T. Kirchartz, J. Oguma, K. Miyake, J. R. Durrant, S. Doi, Electron collection as a limit to polymer:PCBM solar cell efficiency: effect of blend microstructure on carrier mobility and device performance in PTB7:PCBM, Adv. Energy Mater. 4 (2014) 1400311.

[126]   O. V. Mikhnenko, H. Azimi, M. Schrarber, M. Morana, P. W. M. Blom, M. A. Loi, Exciton diffusion length in narrow bandgap polymers, Energy Environ. Sci. 5 (2012) 6960-6965.

[127]   W. Liu, H. Shi, W. Fu, L. Zuo, L. Wang, H. Chen, Efficient ternary blend polymer solar cells with a bipolar diketopyrrolopyrrole small molecule as cascade material, Org. Electron. 25 (2015) 219-224.

[128]   N. Gasparini, L. Lucera, M. Salvador, M. Prosa, G. D. Spyropoulos, P. Kubis, H. J. Egelhaaf, C. J. Brabec, T. Ameri, High-performance ternary organic solar cells with thick active layer exceeding 11 % efficiency, Energy Environ. Sci. 10 (2017) 885-892.

[129]   L. Zhan, S. Li, H. Zhang, F. Gao, T.-K. Lau, X. Lu, D. Sun, P. Wang, M. Shi, C.-Z. Li, H. Chen, A near-infrared photoactive morphology modifier leads to significant current improvement and energy loss mitigation for ternary organic solar cells, Adv. Sci. 5 (2018) 1800755.

[130]   H. Hu, L. Ye, M. Ghasemi, N. Balar, J. J. Rech, S. J. Stuard, W. You, B. T. O'Connor, H. Ade, Highly efficient, stable, and ductile ternary nonfullerene organic solar cells from a two-donor polymer blend, Adv. Mater. 31 (2019) 1808279.

[131]   M. Sygletou, P. Tzourmpakis, C. Petridis, D. Konios, C. Fotakis, E. Kymakis , E. Stratakis, Laser induced nucletion of plasmonic nanoparticles on two-dimensional nanosheets for organic photovoltaics, Journal of Materials Chemistry A 4 (2016) 1020-1027.

[132]   G. Kakavelakis, A. E. Castillo, V. Pellegrini, A. Ansaldo, P. Tzourmpakis, R. Brescia, M. Prato, E. Stratakis, E. Kymakis, F. Bonaccorso, Size-tuning of WSe_2 flakes for high efficiency inverted organic solar cells, ACS Nano 11 (2017) 3517-3531.

[133]   W. Yang, Z. Ye, T. Liang, J. Ye, H. Chen, Facilitate charge transfer at donor/acceptor interface in bulk heterojunction organic photovoltaics by two-dimensional nanoflakes, Solar Energy Materials and Solar Cells 190 (2019) 75-82.

[134]   W. Yang, L. Ye, Fenfa Yao, C. Jin, H. Ade, H. Chen, Black phosphorus nanoflakes as morphology modifier for efficient fullerene-free organic solar cells with high fill-factor and better morphological stability, Nano Res. 12 (2019) 777-783.

[135]   C. Huang, H. Yu, Enhanced carrier mobility and power conversion efficiency of organic solar cells by adding 2D Bi_2OS_2, 2D Mater. 7 (2020) 025023.

[136]   I. Jeon, T. Chiba, C. Delacou, Y. Guo, A. Kaskela, O. Reynaud, E. I. Kauppinen, S. Maruyama, Y. Matsuo, Single-walled carbon nanotube film as electrode in indium-free planar

heterojunction perovskite solar cells: investigation of electron-blocking layers and dopants, Nano Lett. 15 (2015) 6665-6671.

[137]   P. You, Z. Liu, Q. Tai, S. Liu, F. Yan, Efficient semitransparent perovskite solar cells with graphene electrodes, Adv. Mater. 27 (2015) 3632-3638.

[138]   J. T. Wang, J. M. Ball, E. M. Barea, A. Abate, J. A. Alexander-Webber, J. Huang, M. Saliba, I. Mora-Sero, J. Bisquert, H. J. Snaith, R. J. Nicholas, Low-temperature processed electron collection layers of graphene/TiO2 nanocomposites in thin film perovskite solar cells, Nano Lett. 14 (2014) 724-730.

[139]   W. Li, H. Dong, X. Guo, N. Li, J. Li, G. Niu, L. Wang, Graphene oxide as dual functional interface modifier for improving wettability and retarding recombination in hybrid perovskite solar cells, J. Mater. Chem. A 2 (2014) 20105-20111.

[140]   J.-S. Yeo, R. Kang, S. Lee, Y.-J. Jeon, N. Myoung, C.-L. Lee, D.-Y. Kim, J.-M. Yun, Y.-H. Seo, S.-S. Kim, S.-I. Na, Highly efficient and stable planar perovskite solar cells with reduced graphene oxide nanosheets as electrode interlayer, Nano Energy 12 (2015) 96-104.

[141]   G. S. Han, Y. H. Song, Y. U. Jin, J.-W. Lee, N.-G. Park, B. K. Kang, J.-K. Lee, I. S. Cho, D. H. Yoon, H. S. Jung, Reduced graphene oxide/mesoporous TiO2 nanocomposite based perovskite solar cells, ACS Appl. Mater. Interfaces 7 (2015) 23521-23526.

[142]   M. Batmunkh, C. J. Shearer, M. J. Biggs, J. G. Shapter, Solution processed graphene structures for perovskite solar cells, J. Mater. Chem. A 4 (2016) 2605-2616.

[143]   E. Stratakis, K. Savva, D. Konios, C. Petridis, E. Kymakis, Improving the efficiency of organic photovoltaics by tuning the work function of graphene oxide hole transporting layers, Nanoscale 6 (2014) 6925-6931.

[144]   D. Konios, G. Kakavelakis, C. Petridis, K. Savva, E. Stratakis, E. Kymakis, Highly efficient organic photovoltaic devices utilizing work-function tuned graphene oxide derivatives as the anode and cathode charge extraction layers, J. Mater. Chem. A 4 (2016) 1612-1623.

[145]   G. Kakavelakis, D. Konios, E. Stratakis, E. Kymakis, Enhancement of the efficiency and stability of organic photovoltaic devices via the addition of a lithium-neutralized graphene oxide electron-transporting layer, Chem. Mater. 26 (2014) 5988-5993.

[146]   P. You, Z. Liu, Q. Tai, S. Liu, F. Yan, Efficient semitransparent perovskite solar cells with graphene electrodes, Adv. Mater. 27 (2015) 3632-3638.

[147]   H. Sung, N. Ahn, M. S. Jang, J. K. Lee, H. Yoon, N. G. Park, M. Choi, Transparent conductive oxide-free graphene-based perovskite solar cells with over 17 % efficiency, Adv. Energy Mater. 6 (2016) 1501873.

[148]   I. Jeon, J. Yoon, N. Ahn, M. Atwa, C. Delacou, A. Anisimov, E. I. Kauppinen, M. Choi, S. Maruyama, Y. Matsuo, Carbon nanotubes versus graphene as flexible transparent electrodes in inverted perovskite solar cells, J. Phys. Chem. Lett. 8 (2017) 5395-5401.

[149]   J. Yoon, H. Sung, G. Lee, W. Cho, N. Ahn, H. S. Jung, M. Choi, Superflexible, high-efficiency perovskite solar cells utilizing graphene electrodes: towards future foldable power sources, Energy Environ. Sci. 10 (2017) 337.

[150]   Z. Wu, S. Bai, J. Xiang, Z. Yuan, Y. Yang, W. Cui, X. Gao, Z. Liu, Y. Jin, B. Sun, Efficient planar heterojunction perovskite solar cells employing graphene oxide as hole conductor, Nanoscale 6 (2014) 10505-10510.

[151]   J.-S. Yeo, R. Kang, S. Lee, Y.-J. Jeon, N. S. Myoung, C.-L. Lee, D.-Y. Kim. J.-M. Yun, Y.-H. Seo, S.-S. Kim, S.-I. Na, Highly efficient and stable planar perovskite solar cells with reduced graphene oxide nanosheets as electrode interlayer, Nano Energy 12 (2015) 96.

[152]   Y. G. Kim, K. C. Kwon, Q. V. Le, K. Hong, H. W. Jang, S. Y. Kim, Atomically thin two-dimensional materials as hole extraction layers in organolead halide perovskite photovoltaic cells, J. Power Sources 319 (2016) 1-8.

[153]   A. L. Palma, L. Cinà, S. Pescetelli, A. Agresti, M. Raggio, R. Paolesse, F. Bonaccorso, A. D. Carlo, Reduced graphene oxide as efficient and stable hole transporting material in mesoscopic perovskite solar cells, Nano Energy 22 (2016) 349-360.

[154]   H. Chen, Y. Hou, C. E. Halbig, S. Chen, H. Zhang, N. Li, F. Guo, X. Tang, N. Gasparini, I. Levchuk, S. Kahmann, C. O. R. Quiroz, A. Osvet, S. Eigler, C. J. Brabec, Extending the environmental lifetime of unpackaged perovskite solar cells through interfacial design, J. Mater. Chem. A 4 (2016) 11604-11610.

[155]   H. Li, L. Tao, F. Huang, Q. Sun, X. Zhao, J. Han, Y. Shen, M. Wang, Enhancing efficiency of perovskite solar cells via surface passivation with graphene oxide Interlayer, ACS Appl. Mater. Interfaces 9 (2017) 38967-38976.

[156]   S. Feng, Y. Yang, M. Li, J. Wang, Z. Cheng, J. Li, G. Ji, G. Yin, F. Song, Z. Wang, J. Li, X. Gao, High-performance perovskite solar cells engineered by an ammonia modified graphene oxide interfacial layer, ACS Appl. Mater. Interfaces 8 (2016) 14503-14512.

[157]   C.-C. Chung, S. Narra, E. Jokar, H.-P. Wu, E. W.-G. Diau, Inverted planar solar cells based on perovskite/graphene oxide hybrid composites, J. Mater. Chem. A 5 (2017) 13957.

[158]   A. Agresti, S. Pescetelli, L. Cinà, D. Konios, G. Kakavelakis, E. Kymakis, A. D. Carlo, Efficiency and stability enhancement in perovskite solar cells by inserting lithium-neutralized graphene oxide as electron transporting layer, Adv. Funct. Mater. 26 (2016) 2686-2694.

[159]   K. T. Cho, G. Grancini, Y. Lee, D. Konios, S. Paek, E. Kymakis, M. K. Nazeeruddin, Beneficial role of reduced graphene oxide for electron extraction in highly efficient perovskite solar cells, ChemSusChem 9 (2016) 3040-3044.

[160]   G.-H. Kim, H. Jang, Y. J. Yoon, J. Jeong, S. Y. Park, B. Walker, I.-Y. Jeon, Y. Jo, H. Yoon, M. Kim, J.-B. Baek, D. S. Kim, J. Y. Kim, Fluorine functionalized graphene nano platelets for highly stable inverted perovskite solar cells, Nano Lett. 17 (2017) 6385-6390.

[161]   E. Castro, T. J. Sisto, E. L. Romero, F. Liu, S. R. Peurifoy, J. Wang, X. Zhu, C. Nuckolls, L. Echegoyen, Cove-edge nanoribbon materials for efficient inverted halide perovskite solar cells, Angew. Chem. Int. Ed. 56 (2017) 14648-14652.

[162]   M. Zhu, W. Liu, W. Ke, L. Xie, P. Dong and F. Hao, Graphene-modified tin dioxide for efficient planar perovskite solar cells with enhanced electron extraction and reduced hysteresis, ACS Appl. Mater. Interfaces 11 (2018) 666-673.

[163]   A. Capasso, F. Matteocci, L. Najafi, M. Prato, J. Buha, L. Cinà, V. Pellegrini, A. D. Carlo, F. Bonaccorso, Few-layer MoS_2 flakes as active buffer layer for stable perovskite solar cells, Adv. Energy Mater. 6 (2016) 1600920.

[164]   U. Dasgupta, S. Chatterjee, A. J. Pal, Thin-film formation of 2D MoS_2 and its application as a hole-transport layer in planar perovskite solar cells, Sol. Energy Mater Sol. Cells 172 (2017) 353-360.

[165]   R. Dai, Y. Wang, J. Wang, X. Deng, Metal-organic compound modified MoS_2 with enhanced solubility for high-performance perovskite solar cells, ChemSusChem 10 (2017) 2869.

[166]   P. Huang, Z. Wang, Y. Liu, K. Zhang, L. Yuan, Y. Zhou, B. Song, Y. Li, Water-soluble 2D transition metal dichalcogenides as the hole-transport layer for highly efficient and stable p-i-n perovskite solar cells, ACS Appl. Mater. & Interfaces 9 (2017) 25323-25331.

[167]   S. K. Muduli, E. Varrla, S. A. Kulkarni, G. Han, K. Thirumal, O. Lev, S. Mhaisalkar, N. Mathews, 2D black phosphorous nanosheets as a hole transporting material in perovskite solar cells, J. Power Sources 371 (2017) 156-161.

[168]   G. Kakavelakis, I. Paradisanos, B. Paci, A. Generosi, M. Papachatzakis, T. Maksudov, L. Najafi, A. E. D. R. Castillo, G. Kioseoglou, E. Stratakis, F. Bonaccorso, E. Kymakis, Extending the continuous operating lifetime of perovskite solar cells with a molybdenum disulfide hole extraction interlayer, Adv. Energy Mater. 8 (2018) 1702287.

[169]   F. Zhang, J. He, Y. Xiang, K. Zheng, B. Xue, S. Ye, X. Peng, Y. Hao, J. Lian, P. Zeng, J. Qu, J. Song, Semimetal–semiconductor transitions for monolayer antimonene nanosheets and their application in perovskite solar cells, Adv. Mater. 30 (2018) 1803244.

[170]   S. Kohnehpoushi, P. Nazari, B. A. Nejand, M. Eskandar, MoS_2: a two-dimensional hole transporting material for high-efficiency, low-cost perovskite solar cells, Nanotechnology 29 (2018) 205201.

[171]   N. H. Hemasiri, S. Kazim, S. Ahmad, Reduced trap density and mitigating the interfacial losses by placing 2D dichalcogenide material at perovskite/HTM interface in a dopant free perovskite solar cells, Nano Energy 77 (2020) 105292.

[172]   N. H. Hemasiri, S. Kazim, S. Ahmad, 1T-Rich 2D-WS_2 as an interfacial agent to escalate photo-induced charge transfer dynamics in dopant-free perovskite solar cells, J. Mater. Chem. C 9 (2021) 9865-9873.

[173]   J. Cao, G. Tang, P. You, T. Wang, F. Zheng, J. Zhao and F. Yan, Enhanced performance of planar perovskite solar cells induced by van der Waals epitaxial growth of mixed perovskite films on WS_2 Flakes, Adv. Funct. Mater. 30 (2020) 2002358.

[174]   Q. Fu, Z. Xu, X. Tang, T. Liu, X. Dong, X. Zhang, N. Zheng, Z. Xie, Y. Liu, Multifunctional two-dimensional conjugated materials for dopant-free perovskite solar cells with efficiency exceeding 22 %, ACS Energy Lett. 6 (2021) 1521-1532.

[175]   G. Yin, H. Zhao, J. Feng, J. Sun, J. Yan, Z. Liu, S. Lin, S. Liu, Low-temperature and facile solution-processed two-dimensional TiS_2 as an effective electron transport layer for UV-stable planar perovskite solar cells, J. Mater. Chem. A 6 (2018) 9132-9138.

[176]   Y. Wang, S. Wang, X. Chen, Z. Li, J. Wang, T. Li, X. Deng, Largely enhanced V_{OC} and stability in perovskite solar cells with modified energy match by coupled 2D interlayers, J. Mater. Chem. 6 (11) (2018) 4860-4867.

[177]   P. Huang, L. Yuan, K. Zhang, Q. Chen, Y. Zhou, B. Song, Y. Li, Room-temperature and aqueous solution-processed two-dimensional TiS_2 as an electron transport layer for highly efficient and stable planar n-i-p perovskite solar cells, ACS Appl. Mater. Interfaces 10 (2018) 14796-14802.

[178]   L. Yang, Y. Dall'Agnese, K. Hantanasirisakul, C. E. Shuck, K. Maleski, M. Alhabeb, G. Chen, Y. Gao, Y. Sanehira, A. K. Jena, L. Shen, C. Dall'Agnese, X.-F. Wang, Y. Gogotsi, T. Miyasaka, SnO_2–Ti_3C_2 MXene electron transport layers for perovskite solar cells, J. Mater. Chem. A 7 (2019) 5635-5642.

[179]   L. Yang, C. Dall'Agnese, Y. Dall'Agnese, G. Chen, Y. Gao, Y. Sanehira, A. K. Jena, X.-F. Wang, Y. Gogotsi, and T. Miyasaka, Surface-modified metallic $Ti_3C_2T_x$ MXene as electron transport layer for planar heterojunction perovskite solar cells, Adv. Funct. Mater. 29 (2019) 1905694.

[180]   X. Zhao, S. Liu, H. Zhang, S. Y. Chang, W. Huang, B. Zhu, Y. Shen, C. Shen, D. Wang, Y. Yang, M. Wang, 20 % efficient perovskite solar cells with 2D electron transporting layer, Adv. Funct. Mater. 29 (2019) 1805168.

[181]   J. Chen, J. Zhang, C. Huang, Z. Bi, X. Xu, H. Yu, SnO_2/2D-Bi_2O_2Se new hybrid electron transporting layer for efficient and stable perovskite solar cells, Chem. Eng. J. 410 (2021) 128436.

[182]   Y. Wang, H. Zhang, T. Zhang, W. Shi, M. Kan, J. Chen, Y. Zhao, Photostability of $MAPbI_3$ perovskite solar cells by incorporating black phosphorus, Sol. RRL 3 (2019) 1900197.

[183]   Z. Guo, L. Gao, Z. Xu, S. Teo, C. Zhang, Y. Kamata, S. Hayase, T. Ma, High electrical conductivity 2D MXene serves as additive of perovskite for efficient solar cells, Small 1802738 (2018) 1-8.

[184]   D. Saranin, S. Pescetelli, A. Pazniak, D. Rossi, A. Liedl, A. Yakusheva, L. Luchnikov, D. Podgorny, P. Gostischev, S. Didenko, A. Tameev, D. Lizzit, M. Angelucci, R. Cimino, R. Larciprete, A. Agresti, A. D. Carlo, Transition metal carbides (MXene) for efficient NiO-based inverted perovskite solar cells, Nano Energy 82 (2021) 105771.

Um Kanta Aryal is currently postdoctoral researcher at University of Southern Denmark, MCI, Sønderborg, Denmark. He obtained his Ph. D. degree in Chemical Materials and Device Physics from Pusan National University, South Korea. His main research interests include interface engineering, device physics, device fabrication and characterization of solar cells and optoelectronic devices.

Mehrad Ahmadpour received his Ph.D. under the supervision of Prof. wsr. Morten Madsen, at the Mads Clausen Institute (MCI), University of Southern Denmark (SDU) in 2017. His research topics are focused on the usage of metal oxides in improving the efficiency and stability of thin-film solar cells. He has been awarded several national and international project funded postdoc positions at MCI, SDU since 2017, in order to proceed with his research. His research is reflected in many peer-reviewed publications and conference presentations.

Vida Engmann obtained her Dr. in 2014 from Ilmenau University of Technology, Germany. In 2014 she joined Mads Clausen Institute at the University of Southern Denmark, where in 2020 she was appointed associate professor. Her research focuses on bioinspired approaches to stabilization of organic semiconductor thin films and energy devices. For her work on additive-assisted stabilization she received the L'Oréal-UNESCO, Women in Science national award in 2019, and International Rising Talent award in 2020. In 2020 she was awarded the Carlsberg Young Researcher Fellowship. She is a member of SDU Committee on diversity and equality and SDU Expert group on climate.

Horst-Günter Rubahn is professor of physics and director of the Mads Clausen Institute at the University of Southern Denmark. He leads the nanotechnology center NanoSYD. Besides a doctoral title and a habilitation from University of Göttingen he owns an honorary doctoral title from Kaunas University of Technology. He was appointed Danish national expert nanotechnology in the Horizon 2020 Programme Committee NMBP and is chair of the international PhD school PCAM. Horst-Günter Rubahn's recent research focuses on the development of generic routes towards novel thin film smart materials. This includes the complete range from fundamental via applied research to device integration.

Aldo Di Carlo is a Professor at the University of Rome Tor Vergata and Director of the Institute of Structure of Matter of the National Research Council. His research activity mainly involves the design, fabrication, and characterization of solution-processed solar cells and other optoelectronic devices. He was the founder of the Centre for Hybrid and Organic Solar Energy (CHOSE), which involved more than 40 researchers. He was the CTO of Dyepower, a consortium for the industrialization of dye solar cells for façade applications. He has authored/co-authored more than 500 publications, review articles, and book chapters, and he owns 13 patents.

Morten Madsen, Professor wsr at the University of Southern Denmark (SDU), Mads Clausen Institute. Finalized in 2009 his PhD within Functional Materials and Nanotechnology, SDU NanoSYD. Conducted a postdoc fellowship (2010-2011) at Prof. Ali Javey lab, UC Berkeley, and started in 2011 the organic photovoltaics (OPV) group at SDU. He is heading the SDU Roll-to-Roll (R2R) facility that focuses on up-scaling of OPV and energy devices. Holds more than 75 peer-reviewed publications on these topics, including two books as Editor. Coordinator of the Marie Curie ITN network THINFACE and EU Interreg project RollFlex, and PI on several national and international research projects.